Andreev Reflections and transport phenomena in superconductors at the interface with ferromagnets and normal metals

Samanta Piano

A Dissertation submitted for the Degree of Philosophiae Doctor in Physics in the

Dipartimento di Fisica "E.R. Caianiello"
Facoltà di Scienze Matematiche Fisiche e Naturali
Università degli Studi di Salerno

Supervisors

Dr. Fabrizio Bobba
Prof. Anna Maria Cucolo
Prof. Mark G. Blamire

Coordinator

Prof. Gaetano Vilasi

V Ciclo Nuova Serie (2003-2006)

...to my husband and
my little child who grows inside me

Abstract

This dissertation contains the experimental investigation of the symmetry of the superconducting order parameter in novel superconductors and of the interaction between superconductivity and magnetism in atomic-size and artificial heterostructures. The main scope has been to study the superconducting order parameter and the modification of the density of states due to the presence of a magnetic order. This work has been devoted not only to the fundamental physics but also to the possible development of useful systems for the realization of quantum electronic devices. The tool of investigation of these systems has been the Andreev reflection spectroscopy. The symmetry of the order parameter has been explored in novel superconductors, such as MgB_2 and $RuSr_2GdCu_2O_8$ with the point contact technique. For the first one we have used a tip of Niobium, so realizing a S/N/S' Josephson junctions. The conductance characteristics have shown the Josephson current and the presence of subharmonic gap structures, that have been explained in terms of multiple Andreev reflections [S2,S8]. The point contact Andreev reflection spectroscopy carried out on $RuSr_2GdCu_2O_8$ has evidenced the *d-wave* symmetry of the superconducting order parameter and, due to the presence of a magnetic order in this compound, a reduced amplitude of the superconducting energy gap has been measured [S1,S3,S4]. Furthermore, the presence of these two competitive orders has shown a peculiar temperature dependence of the superconducting energy gap. Artificial F/S ($YBa_2Cu_3O_{7-x}/La_{0.7}Ca_{0.3}MnO_3$) heterostructures have been analyzed in order to investigate the interplay between superconductivity and ferromagnetism [S5,S7]. Also in this case from the conductance curves a reduced amplitude of the superconducting energy gap has been extrapolated, then an estimation of the polarization of the $La_{0.7}Ca_{0.3}MnO_3$ has been drawn. Moreover the study of the coexistence between ferromagnetism and superconductivity has been performed in nanostructured S/F/S Josephson junctions [S6,S9,S10]. S/F/S heterostructures, constituted by a low-T_C superconductor, Niobium, and strong ferromagnetic materials, Nickel, $Ni_{80}Fe_{20}$, Cobalt and Iron, have been fabricated and analyzed. The oscillations of critical current have been analyzed as a function of the ferromagnetic barrier thickness. From the theoretical models we have estimated the exchange energy of the ferromagnetic layer. This analysis has given, for the magnetic and electrical properties of these heterostructures, a good input towards the realization of coherent two-state quantum systems.

Acknowledgments

Before reading this dissertation I would like that the reader paid attention to these few lines. In this page I feel to thank all the people who have shared with me my PhD experience.

First of all I am very grateful to my supervisors, Dr. Fabrizio Bobba and Prof. Anna Maria Cucolo. Two persons that have followed my scientific growth, they have been my support and my encouragement, giving me the possibility to learn and "experiment". In particular I thank Dr. Fabrizio Bobba, he has followed my scientific formation in laboratory, handing me the possibility to make mistakes and hence to learn the way of the experimental physicist; his helpfulness and friendship were never missing. On the other hand, I thank Prof. Anna Maria Cucolo for her guidance, suggestions and clever advices. She has taught me to write papers and she has helped me to always believe in my capabilities.

Many thanks go to Prof. Mark Blamire, my "external" supervisor, he has allowed me to live the great experience to work in his group in Cambridge for one year. The British experience has been important not only for the results included in this thesis but also for my personal and scientific growth. And in the group of Prof. Mark Blamire I thank in particular Jason Robinson, who has instructed me to the usage of the numerous instruments in Cambridge, and with whom I established a fruitful and friendly collaboration: thanks Jason for understanding my horrible English pronunciation, and letting it improve.

I thank my friend, colleague and husband, Gerardo Adesso, he has believed in me, always..... and he is my first supporter and my first referee. I feel to thank him for all that I am and I have done in these three years.

At the end I thank my colleagues and friends in Salerno, in particular Dr. Filippo Giubileo and Alessandro Scarfato, and in Cambridge, Dr. Gavin Burnell and Nadia Stelmashenko, who has prevented me to destroy the sputtering...thanks Nadia for your support. And thanks to my two families, they have always accepted my decisions and, why not, sometimes my madnesses.

A big thank you to all!!!!

CONTENTS

INTRODUCTION

Immanuel Kant (1724-1804)

....Mathematics and physics are the two theoretical sciences of reason, which have to determine their objects a priori; the former quite purely, the latter partially so, and partially from other sources of knowledge besides reason...Reason, holding in one hand its principles, according to which concordant phenomena alone can be admitted as laws of nature, and in the other hand the experiment, which it has devised according to those principles, must approach nature, in order to be taught by it: but not in the character of a pupil, who agrees to everything the master likes, but as an appointed judge, who compels the witnesses to answer the questions which he himself proposes.....

The history of superconductivity has begun in 1911 thanks to the experiments performed by Kamerlingh Onnes. In 1956 John Bardeen, Leon Cooper, and Robert Schrieffer explained the disappearance of electrical resistivity in terms of electron pairing in the crystal lattice: the BCS microscopic theory of the superconductivity was born. Among the experimental techniques which allowed testing this theory, quasiparticle tunneling introduced by Giaever (1960) played a central role. Giaever showed that a planar junction composed of a superconducting film and a normal metal separated by a nanometer thin insulator, has striking current voltage characteristics. He showed that the derivative, the tunneling conductance, has a functional dependence on the voltage which reflects the BCS quasiparticle density of states. This was the beginning of tunneling spectroscopy, which was later used by Mc-Millan and Rowell (1965) to establish a quantitative confirmation of the BCS theory.

A new era in the study of superconductivity began in 1986 with the discovery of high-critical-temperature superconducting cuprates, new materials that showed a critical temperature up to 40 K, where the superconductivity seemed to come from the CuO_2 planes. Despite 20 years of intensive research, the mechanism of superconductivity in high-T_C superconductors is still not clarified. A necessary first step in identifying the effective interactions responsible for the superconductivity is to fully identify the symmetry of the pairing state and to explain the various relevant experimental properties below T_C. In recent years, the results of many experiments have made it generally acceptable to assume that high-T_C cuprates exhibit d-wave symmetry of the superconducting energy gap; however, the idea that the order parameter is of s-wave type still remains tenaciously. We remark that the nature of the symmetry of the order parameter for the high-T_C cuprates occupies a center stage in high-T_C research and an understanding of this would shed considerable light on the microscopic interactions that lead to superconductivity in these unusual systems.

Among a variety of techniques, the point contact spectroscopy has proved to be a comparatively simple, available and highly informative method to investigate the symmetry of the order parameter in high temperature superconductors. It is indeed often difficult to have these compounds in form of thin films or single crystal, so it is not possible to realize planar junctions and the point contact spectroscopy presents itself as the only tool of investigation.

It has generally been believed that, within the context of the BCS theory of superconductivity, the conduction electrons in a metal cannot be both

ferromagnetically ordered and superconducting. In fact superconductors expel magnetic field passing through them but strong magnetic fields kill the superconductivity (Meissner effect). Even small amounts of magnetic impurities are usually enough to eliminate the superconducting phase. In spite of this effect in 1977 the discovery of ternary rare-earth (RE) compounds (RE)Rh_4B_4 and (RE)Mo_6X_8, with X=S, Se, where magnetism and superconductivity coexist, has opened a new field of research. For this reason "intrinsic" and artificial F/S bilayers have been realized and investigated. It has been verified that colossal magnetoresistance manganites have good structural compatibility with high-T_C superconductors, and are a rich reservoir of spin-polarized charges, which can be used for spin injection studies. Injection of spin-polarized electrons into a superconductor with energy greater than the energy gap induces a non-equilibrium state in the superconductor by creating non-equilibrium population of spins in the material, both by scattering and pair breaking phenomenon. These heterostructures are interesting for their properties and the possible applications.

But what about the F/S structures where S is a BCS superconductor and F is a ferromagnetic material? The attention naturally turns towards these systems. It has been verified that, due to the presence of these competitive orders, peculiar effects appear: the superconductivity is reduced by the spin polarization of the F layer, then due to the proximity effect the Cooper pairs can enter in the superconductor resulting in a oscillatory behavior of the density of states. The last effect opens the doors towards new and exciting developments for the realization of quantum electronic devices. In fact in S/F/S systems, due to the oscillations of the order parameter, some oscillations manifest in the Josephson critical current as a function of the ferromagnetic barrier thickness evidencing the presence of two different states, 0 and π, corresponding to the sign change of the Josephson critical current.

Our research, presented in this dissertation, fits in this rapidly developing and exciting area of condensed matter physics.

In the first place we have investigated, by means of the point contact Andreev reflection spectroscopy, the symmetry of the order parameter of a novel superconductor, MgB_2 and a high-T_C cuprate superconductor, $RuSr_2GdCu_2O_8$. The MgB_2 compound presents *s-wave* symmetry of the order parameter. In this case S/N/S' junctions have been realized using a tip of Niobium. So, due to the multiple Andreev reflection, subharmonic gap structures have been evidenced at integer multiples of the superconducting energy gap of the two superconductors. On the compound $RuSr_2GdCu_2O_8$, the first detailed study of the symmetry of superconducting energy gap has been carried out. N/S junctions have shown a *d-wave* symmetry of the order parameter with an amplitude of the superconducting energy gap lower than the conventional cuprate

superconductors. We have explained this effect in terms of the proximity effect due to the ferromagnetic order. In fact many experiments have shown in this compound a coexistence between superconductivity and ferromagnetism. Another effect of this interplay is the peculiar, sublinear temperature dependence of the superconducting energy gap. We have evidenced these features also in the artificial F/S heterostructures constituted by a cuprate, $YBa_2Cu_3O_8$, and a colossal magneto-resistance oxide, $La_{0.7}Ca_{0.3}MnO_3$.

Within the context of the interplay between superconductivity and ferromagnetism, we have fabricated and investigated the magnetic and electrical properties of S/F/S nano-structured Josephson junctions constituted by a low temperature superconductor, Niobium, and strong ferromagnetic metal, Ni, $Ni_{80}Fe_{20}$, Co and Fe. These structures have evidenced a small magnetic dead layer and oscillations of the critical current as a function of the ferromagnetic barrier. The results on S/F/S junctions with Ni and $Ni_{80}Fe_{20}$ have reported values of the exchange energy in agreement with other works. For the first time we have reported critical current oscillations of Josephson junctions with Co and Fe. For the high value of the exchange energies and small magnetic dead layer these two materials can be considered as good candidates for the realization of quantum devices.

This dissertation is organized as follows. In Chapter 1 the physics of the superconducting and ferromagnetic materials is discussed with a hint to the BCS theory and the theoretical models to describe these systems. A discussion on the possible coexistence of these two antagonist orders concludes this Chapter. The Chapter 2 reviews the theory of the tunnel junctions and the weak links regarding different transport regimes from the tunneling to the Andreev reflection process. Then the Josephson junction model and its modification with a ferromagnetic barrier is also presented. The experimental techniques and apparatuses needed for our study are described in Chapter 3. The last two Chapters contain the original results of this work, which have appeared in Refs. [S1–S10]. In particular in Chapter 4 we present the point contact spectroscopy measurements carried out on a novel superconductor, MgB_2, on a cuprate High-T_C superconductor, $RuSr_2GdCu_2O_8$, and on an artificial F/S system constituted by a cuprate, $YBa_2Cu_3O_8$, and a colossal magneto-resistance oxide, $La_{0.7}Ca_{0.3}MnO_3$. In Chapter 5 we describe the fabrication and the transport measurements of sub-micron Josephson junctions constituted by a low temperature superconductor, Niobium, and strong ferromagnetic barriers, Nickel, Permalloy ($Ni_{80}Fe_{20}$), Cobalt and Iron. In Chapter 6 we draw our conclusions and outline possible future research developments.

PART I

THEORY

CHAPTER 1

SUPERCONDUCTIVITY AND FERROMAGNETISM

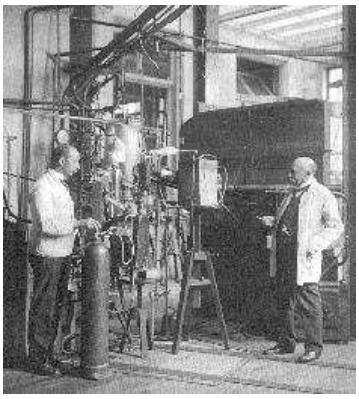

Heike Kamerlingh Onnes (1853-1926)
....Mercury has passed into a new state, which on account of its extraordinary electrical properties may be called the superconductive state..

In this part we explain the main properties of superconducting and ferromagnetic materials, in order to give a basic background to understand the experimental data that we will show in Part II.

1.1. Fundamental properties of the superconducting materials

Superconductivity was discovered in 1911 by Heike Kamerlingh Onnes[125]. He was investigating the electrical properties of various substances at liquid helium temperature (4.2 K) when he noticed that the resistivity of mercury dropped abruptly at 4.2 K to a value below the resolution of his instruments. After many researches the physicists arrived at the first characteristic property of the superconductors: their electrical resistance is zero below a well-defined

temperature T_C, called the critical temperature. Then it has been observed that at any temperature below the critical temperature, the application of a minimum magnetic field $H_C(T)$ destroys the superconductivity restoring the normal resistance appropriate for that field. So the relation between the critical field H_C and the transition temperature T_C is:

$$H_C(T) = H_C(0)(1 - T/T_C). \tag{1.1}$$

Anyway the critical field H_C for the destruction of the superconductivity can be experimentally determined only for the so-called type I superconductors. The great majority of superconductors are of type II, and their transition between the normal and the superconducting states is spread out over a finite range of magnetic fields [128]. The observation of the temperature dependence of the critical field, combined with the zero resistance in the superconducting phase, led Meissner and Ochsenfeld [115] to the following result. If a superconductor, posed in a magnetic field, is cooled down the transition temperature, the lines of the induction field B are pushed out, in other words B vanishes inside the superconductor (Meissner effect).

London [108] showed that the pure superconducting state in a magnetic field has a persistent shielding current associated with it. Since Meissner effect is very well established for samples of macroscopic dimensions, this current must be confined to a region very close to the surface. Expressed in terms of the field, we can conclude that B drops to a vanishing value over a characteristic penetration depth $\lambda \sim 10^{-5}$ cm.

1.2. Microscopic theory of the superconductivity

To understand the physics of the systems that we study in this work we recall the basic aspects of the microscopic theory of the superconductivity of Bardeen-Cooper-Schrieffer (BCS theory) [12, 13]. The BCS theory uses the Fröhlich Hamiltonian [10] of the interaction between electrons and phonons to show that, as a consequence of this interaction, there is a deformation of the crystal lattice that under certain conditions determines an attraction between the two electrons with the formation of a coupled state(Cooper Pair) [11]. At T=0 in the superconducting ground state all electrons are paired and the superconducting ground state has the following expression:

$$|\psi\rangle = \prod_{\vec{k}} [u_{\vec{k}} + v_{\vec{k}} c^*_{\vec{k}\uparrow} c^*_{-\vec{k}\downarrow}]|0\rangle, \tag{1.2}$$

where $|0\rangle$ is the vacuum state, $c^*_{\vec{k}\uparrow}(c^*_{-\vec{k}\downarrow})$ is the single-electron operator that creates an electron with momentum $\vec{k}$ $(-\vec{k})$ and spin $\uparrow$ $(\downarrow)$. While, $v^2_{\vec{k}}$ is the probability of pair occupancy and $u^2_{\vec{k}} = 1 - v^2_{\vec{k}}$ is the probability of pair vacancy.

At T=0 a certain minimum amount of energy is required to break the Cooper pair, this energy is called the *energy gap*. In terms of the momentum k, the expression of the energy gap is:

$$\Delta_{\vec{k}} = -\sum_{\vec{k'}} V_{\vec{k}\vec{k'}} v_{\vec{k'}} u_{\vec{k'}} \tag{1.3}$$

where $V_{\vec{k}\vec{k'}}$ is the electron-electron interaction energy [168]. Assuming that the electron-electron interaction is constant in a shell around the Fermi level of width $\hbar\omega_D$, with ω_D the Debye frequency:

$$V_{\vec{k}\vec{k'}} = \begin{cases} -V, & |E_{k'}|, |E_k| \leq \hbar\omega_D; \\ 0, & \text{otherwise}, \end{cases} \tag{1.4}$$

the energy gap Δ will be independent on k. We refer to an *s-wave* symmetry of the order parameter in the case of a gap uniform in the k-space. The probabilities of vacancy and occupancy in terms of the excitation energy of the quasiparticle $\tilde{E_k} = \sqrt{E_k^2 + \Delta^2}$ and the energy gap Δ are given by:

$$u_k^2 = \frac{1}{2}\left[1 + \frac{\sqrt{\tilde{E}_k^2 - \Delta^2}}{\tilde{E}_k}\right]; v_k^2 = \frac{1}{2}\left[1 - \frac{\sqrt{\tilde{E}_k^2 - \Delta^2}}{\tilde{E}_k}\right] \tag{1.5}$$

We can rewrite Eq. 1.3 in the following expression:

$$\Delta = \frac{V}{2}\sum_{k'} \frac{\Delta}{\sqrt{E_{k'}^2 + \Delta^2}}. \tag{1.6}$$

For T=0 we can simply verify that the expression for the energy gap becomes:

$$\Delta = \frac{\hbar\omega_D}{\sinh(1/VN(0))} \tag{1.7}$$

with $N(0)$ being the density of electrons at the Fermi energy in the normal state.

For T$\neq$ 0 the probability that the state with vector k' is occupied is given by the Fermi-Dirac distribution:

$$f(E_k) = \frac{1}{1 + \exp[\tilde{E_k}/K_B T]}, \tag{1.8}$$

so Eq. 1.3 is modified by introducing the Fermi-Dirac distribution:

$$\Delta_k = \sum_{k'} V_{k,k'} \frac{\Delta_{k'}}{2\tilde{E_{k'}}} \tanh\left(\frac{\tilde{E_{k'}}}{2K_B T}\right) \tag{1.9}$$

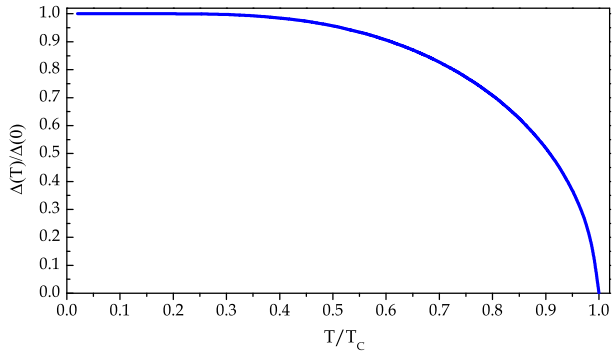

FIGURE 1.1. Temperature dependence of the superconducting energy gap obtained by the numerical solution of Eq. 1.10, where $\Delta(0)$ is the value of the energy gap at T=0.

Assuming the approximate form for the electron-electron energy, Eq. 1.4, and going to the continuum, the self- consistent equation for the gap becomes:

$$\frac{1}{VN(0)} = \int_0^{k\omega_D} dE \frac{1}{\sqrt{E^2+\Delta^2}} \tanh\left(\frac{(E^2+\Delta^2)^{1/2}}{2K_BT}\right) \tag{1.10}$$

The numerical solution of Eq. 1.10 determines the temperature dependence of the gap. In Fig. 1.1 we show the temperature dependence of the energy gap in agreement with Eq. 1.10

We notice that Eq. 1.10 has not solution for each T, this means that there is a critical temperature T_C so that for $T > T_C$ the superconducting energy gap cannot be determined. This temperature can be calculated in the limit $\Delta(T) \to 0$, giving:

$$\frac{2\Delta(0)}{K_BT_C} = 3.52. \tag{1.11}$$

From experimental measurements on conventional superconductors it has been found that this numerical factor falls between 3.0 and 4.5. Furthermore from the BCS theory we can directly obtain the expression of the superconducting density of states:

$$\frac{N_S(E)}{N_N(0)} \begin{cases} \frac{E}{\sqrt{(E^2-\Delta^2)}} & E > \Delta; \\ 0 & E < \Delta, \end{cases} \tag{1.12}$$

so we can conclude that a measurement of the density of states is a direct estimation of the superconducting energy gap.

1.3. High-T_C Superconductivity

The history of the high temperature superconductors (HTSC) has begun in 1986, when J. George Bednorz and Karl Müller of the IBM research laboratory in Zurich, Switzerland, reported [17] the observation of superconductivity in the compound LaCuO doped with Ba or Sr atoms at temperatures up to 38 K. This caused tremendous excitement because 38 K was above the limit of 30 K for superconductivity that had been theoretically predicted almost 20 years earlier. Since then many investigations [78, 109] have been carried out on high-T_C superconductors with the dream to find the room-temperature superconductors.

At that point, the compound $YBa_2Cu_3O_7$ took a central place [178], because of its high value of the $T_C = 92$ K. Subsequently, attention was focused on the compound $Bi_2Sr_2CaCu_2O_8$ with $T_C = 105$ K. That was followed by the discovery in 1988 of $Tl_2Ca_2Ba_2CuO_{10}$ [154], with $T_C = 125$ K and currently a mercury-based material has been found to have the highest critical temperature of about 133 K [147]. After more than 20 years, the field of high-T_C superconductivity still remains very active and in development. From the experimental viewpoint much work has been carried out to improve the quality of the samples with reproducible properties, for example single crystals and thin films are available. Nevertheless it is difficult to develop a complete theory that can describe the physics of these materials due to the complexity of their properties. In particular, there is no doubt that the superconductivity is based on Cooper pairs of electrons with zero net momentum because the usual ac Josephson effect frequency is presented at integer multiplies of $2eV/\hbar$ and the flux quantum is observed of the usual size $hc/2e$, like the conventional superconductors [168]. Moreover, the BCS theory appears inadequate to explain the vast and different characteristics of the new superconductors. For example one and three-band Hubbard models have been proposed to give an explanation of the electrical behavior of these compounds, but these theories cannot take into account all the properties of the high-T_C superconductors.

The high-T_C superconducting oxides are layered cuprate perovskites. One of the important characteristics of all cuprates is the presence of CuO_2 planes separated by layers of other atoms (Ba, O, La,...) that have the function of charge reservoirs and it is believed that the superconductivity occurs in these planes, for this reason these compounds are generally called "cuprates". The critical temperature of the cuprate superconductors depends on the number of CuO_2 planes, in fact it has been shown that T_C increases with increasing number of CuO_2 layers. Due to the complex layered crystal structure, these compounds present a strong anisotropy of the electrical and transport properties. Measurements of the resistivity as a function of the temperature in the CuO_2 planes have shown a linear temperature behavior. For different

materials the slopes of the curves are very similar suggesting a common scattering mechanism for the carrier transport in the CuO_2 planes. These new superconductors, moreover, present a short coherence length, $\xi \sim 12\mathring{A}$ to $15\mathring{A}$, smaller than that the conventional superconductors ($\xi \sim 500\mathring{A}$ to $10000\mathring{A}$). The coherence length is associated with the average size of the Cooper pair, this means that a standard mean-field theory cannot describe the physics of these compounds. Another common property of these materials is the presence of antiferromagnetic order at low temperature in the undoped regime, i.e. when there are not free carriers in the planes. When the planes are doped the antiferromagnetic order disappears and the superconducting phase occurs. Anyway this doesn't mean that there is not a correlation between these two orders, in fact in literature some theories relating superconductivity and ferromagnetism are proposed, as we briefly show in Sec. 1.5

1.3.1. Symmetry of the order parameter

We ask ourselves another question: is the superconducting pairing in these materials of the familiar *s-wave* type on which conventional BCS theory is based, or some other form of pairing appears? Many experiments and theoretical predictions seem to show for these materials a deviation from the *s-wave* symmetry of the BCS superconductors supporting the evidence of an unconventional symmetry of the order parameter [80]. With the term "unconventional" we mean a state with a symmetry in the momentum k-space different from the isotropic *s-wave* symmetry of the conventional superconductors. Experimental observations that are sensitive to the phase [177, 171] and nodes of the gap [79], reported a sign reversal of the order parameter supporting *d-wave* pairing. On the other hand, a group of experiments indicate existence of a significant *s-wave* component [44, 164, 96]. There are also indications, both from theories and experiments, that the high T_C materials may have a mixed pairing symmetry ($d + s$, $d + is$, $d + e^{i\theta}\alpha$, with $\alpha = s, d_{xy}$ [93], etc) in the presence of external magnetic field, magnetic impurities [101], interface effects [63] etc. In Fig. 1.2 we show some of the possible symmetries for the cuprates. We notice that a *s-wave* symmetry of the order parameter presents a magnitude and a phase constant in the k-space, while for the *s-anisotropic* and *d-wave* symmetry nodal lines appear in the magnitude of the order parameter. But the behavior of the phase is different: for a *s-wave* symmetry the phase is uniform, while for a *d-wave* state the phase presents discontinuity along the nodal lines (110). Therefore, to identify the pairing state, an experiment should be sensible not only to the magnitude but also to the phase of the order parameter. As we will show in the next Chapter, experiments based on the Andreev reflections are an useful tool to investigate the symmetry of the order parameter, in fact in this case due to the sign change

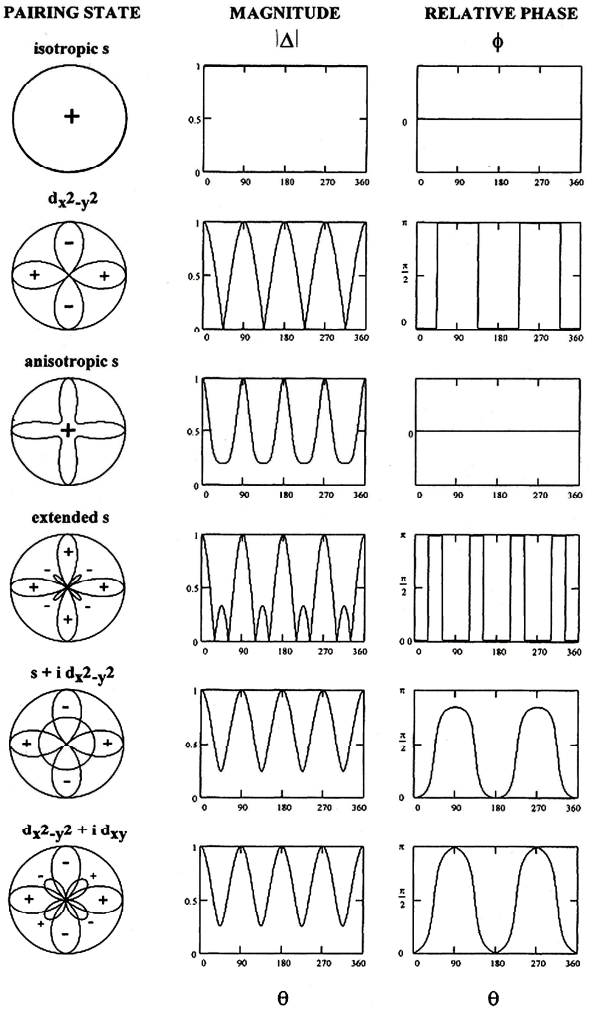

FIGURE 1.2. Magnitude and phase of the superconducting energy gap for different symmetry of the pairing state. Figure adapted from Ref. [80]

of the phase of the order parameter bound states appear at the Fermi level of the superconductor.

1.4. Magnetism

In this section we introduce some properties of magnetic materials, with a particular accent to the ferromagnetic and colossal magneto-resistance compounds, accompanied by brief hints to the recent theories that explain the characteristics of these systems.

1.4.1. Magnetic order

In a solid the band electrons and sometimes also the ions in the crystalline lattice, carry a microscopic magnetic moment [33]. In the case of electrons, this is due to the spin angular momentum; atomic moments result from the orbital motion of the shell electrons, or incompletely filled inner shells. There is a significant difference in character between these moment-carriers. The atoms, and therefore also their moments, are localized at the crystal lattice points. The band electrons, however, propagate through the crystal as Bloch waves, and are regarded as delocalized. Consequently, it is necessary to consider a density of their spins, which is a continuously varying function of position. In a non-magnetic material there is no long-range ordering of the microscopic magnetic moments over sufficiently large distances, the orientation of the localized moments on the atoms varies randomly, and the departures from the band-electron's average spin density of zero are uncorrelated. Thus, in both cases, the magnetization M (the average moment per unit volume) is zero. The application of an external magnetic field H has two effects: (a) to align the microscopic magnetic moments in direction of the field, and (b) to induce anti-aligned moments due to the orbital response of the electrons. When the former process is dominant, the material is paramagnetic; dominance by the latter leads to diamagnetism. In both cases, the external field induces a magnetization, $M = \chi H$; where χ is the magnetic susceptibility of the material and is positive for paramagnets, negative for diamagnets. For both materials, the magnetization vanishes when the external field is removed, the system returns to its original disordered state.

In a magnetic material a spontaneous long-range ordering of the microscopic moments exists. This is due to so-called exchange interactions between the moment carriers. There are two major classes of magnetic materials exhibiting spontaneous order, ferromagnets and antiferromagnets. In ferromagnetic materials, the exchange interactions tend to align the moments in one direction, giving the material a non-zero magnetization. The preferred direction of alignment (the so-called easy axis) is determined by secondary coupling to the crystal field (e.g. spin-orbit effects). In contrast to ferromagnets, the exchange interactions in antiferromagnetic materials tend to periodically order the moments in such a way that there is no overall magnetization of the system. In

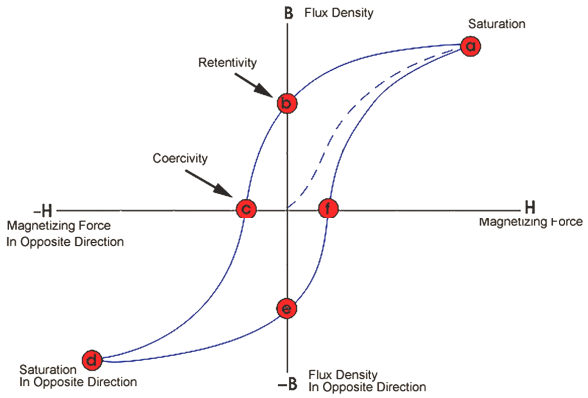

FIGURE 1.3. Hysteresis loop for a ferromagnet.

both ferromagnets and antiferromagnets the tendency of the exchange interactions to order the moments is counteracted by thermal fluctuations; in the limit of zero temperature, the thermal agitations which destroy the ordering vanish, and the degree of order is limited only by quantum effects.

1.4.2. Ferromagnetism

The characteristic property of a ferromagnet is the spontaneous magnetization produced by the exchange interactions. This magnetization is not necessarily uniform across the sample. A ferromagnet may be divided into macroscopic volumes called domains, each possessing one oriented magnetic moment. The application of an external magnetic field results in an expansion of the domains with moments aligned with the field at the expense of those with anti-aligned moments. This process is irreversible and leads to a permanent increase in the magnetization of the sample (hysteresis effect). The magnitude of the spontaneous magnetization of a domain obtains a maximum in the limit of zero temperature. This maximum magnetization is referred to as the saturation magnetization (Ms) of the material. In Fig. 1.3 we plot the magnetization M versus H. The magnetic material starts at the origin in an unmagnetized state, and the magnetic induction follows the curve from 0 to M_S, the saturation induction, as the field is increased in the positive direction. When H is reduced to zero after the saturation, the induction decreases from M_S to M_R, the residual induction. The reserved field required to reduce the induction to zero is called the coercivity, H_C. Depending on the value of the coercivity, the ferromagnetic materials are classified as hard or soft. When the reversed H is increased further, saturation is achieved in the reverse direction. The loop that is traced out is called the major hysteresis loop.

Due to the dominance of thermal fluctuations, the spontaneous magnetization of a ferromagnet disappears above a certain critical temperature, the Curie temperature (T_{Curie}). Generally, a ferromagnetic material becomes paramagnetic above T_{Curie}, but certain rare-earth elements exhibit anti ferromagnetic ordering at temperatures higher than T_{Curie} [113]. The phase transition from the ferromagnetic to the paramagnetic phase (the normal phase) is the classic example of a second order phase transition. Theoretical attempts of a microscopic theory of ferromagnetism generally regard either the magnetic ordering of the lattice atoms or the band electrons as of primary importance. Such models are classified as "localized" and "itinerant", respectively. Although in any real system, both localized and itinerant effects are likely to be present to differing degrees, it is usually possible to expect one to dominate the other. For example, the rare-earth ferromagnets and their ionic compounds (such as EuO and GdC_{12}) are regarded as good examples of localized systems, whereas the ferromagnetism of the 3d transition metals (iron, nickel, and cobalt) and a number of alloys of non-magnetic elements (e.g. $ZrZn_2$ and Sc_3In) are best explained by the itinerant scheme [138]. Theoretical studies of itinerant electron models began in 1929 with the pioneering efforts of Bloch. His work indicated that ferromagnetism was only likely to appear in the homogeneous electron gas at very low densities; more detailed studies have proved that the homogeneous electron gas is not ferromagnetic at typical metallic densities. This has been confirmed by computational studies which predict the onset of ferromagnetic ordering only at extremely low densities. There is, however, much disagreement about the precise density range, and the physics of these low density regimes should be regarded with caution [127]. More detailed models of itinerant electron systems have met with considerably better success than the homogeneous electron gas approximation. These models have demonstrated the main important role played by the band structure in determining whether or not itinerant electron ferromagnetism will appear in a material. Of particular note is the so-called Slater and Stoner models [157, 159], which gives a criterion for the appearance of ferromagnetism in terms of the density of states at the Fermi energy. The Stoner model gives a very basic phenomenological description of an itinerant system, and considerable improvement has been made upon it [102]. Nevertheless, it has provided a useful starting point for the study of itinerant electron ferromagnetism.

1.4.3. Colossal magnetoresistance

In 1950 Jonker and Van Santen reported the first study on polycrystalline samples of (La,Ca)MnO_3, (La,Sr)MnO_3 and (La,Ba)MnO_3 evidencing in these compounds the presence of a ferromagnetic order [89]. These compounds are usually called manganites. The first studies attributed this order to a positive *indirect-exchange* interaction, but this viewpoint was soon replaced

by the excepted *double-exchange* model. In this model the ferromagnetism is interpreted as rising from an indirect coupling between incomplete *d-shells*, via conducting electrons. Studies of the lattice parameters as a function of the hole doping, in these samples, reported distortions of the crystalline structure; these effects are explained in terms of the Jahn-Teller effect [77]. Furthermore Wollan and Koehler [176], using neutron diffraction techniques, found that in addition to the ferromagnetic order, an antiferromagnetic phase is presented in manganites. In some cases, they also reported evidence of charge ordering coexisting with the antiferromagnetic phase. One of the most remarkable properties of the manganites is the influence of a magnetic transition on the electronic conduction. Already in 1950, Jonker and Van Santen [89] discovered that the resistance below the magnetic ordering, $T<T_{Curie}$, exhibits a positive thermal coefficient, indicating metallic-like behavior and a negative gradient above T_{Curie}. This brings about a maximum in the resistivity curve near T_{Curie}. Despite much progress, the implications of this behavior were only explored in 1993, when a reduction of the resistance was observed in thin films under application of an external magnetic field by Chahara et al. [43] and Von Helmolt et al. [82]. This reduction was only 50% of the zero field resistance. A year later it was proven possible to reduce the resistivity by several orders of magnitude [87]. The term Colossal Magnetoresistance (CMR) was coined. The CMR is a bulk property which originates from magnetic ordering and is usually connected to the vicinity of T_{Curie}. The electronic transport properties of the transition metal oxides strongly interact with the magnetic properties and with the crystal lattice. Because many properties and transitions cannot be described by simple one-electron models, these compounds are generally regarded as strongly correlated electron systems. Tokura [170] proposed that the charge-ordering states observed by Wollan and Koehler [176], and Jirák et al.[88] are very important for the explanation of the CMR effect. They presented results indicating an abrupt collapse of the charge-ordered state into a ferromagnetic state under the influence of a magnetic field. The competition between charge-ordering state and ferromagnetism is indeed a key component of the current theories of manganites aiming to explain the CMR phenomenon.

1.5. Interplay between superconductivity and ferromagnetism

In the previous section we have presented the basic principles of the superconductivity and the ferromagnetism, in this section we raise the question whether these two different orders can coexist. Many theoretical and experimental works have investigated this interplay to search the possibility of coexistence between these two competing phases. In 1956 Ginzburg [68] proposed

the problem of the coexistence of magnetism and superconductivity considering an orbital mechanism by which he concluded that the superconductivity is suppressed from the ferromagnetic order. With the microscopic theory of the superconductivity in 1957, Bardeen, Cooper, and Schrieffer showed that the superconductivity in the singlet state is destroyed by an exchange mechanism [12]. The exchange field, in fact, in a magnetically ordered state, tends to align spins of Cooper pairs in the same direction, thus preventing a pairing effect. Abrikosov [2] studied superconductivity with magnetic impurities using the Ruderman-Kittel-Kasuya-Yosida interaction in which magnetic impurities interact with conduction electrons with the magnetization considered as an external parameter independent of the superconducting gap, and showed that the normal ferromagnetic state has lower energy than the superconducting-ferromagnetic state and hence coexistence is energetically unfavorable. Afterwards Fulde and Ferrell [64] studied superconductivity with a strong exchange field produced by ferromagnetically aligned impurities and found that if the exchange field is sufficiently strong compared to the energy gap, a new type of depaired superconducting ground state will occur. On the other hand, Fay and Appel [60] predicted the possibility of a *p-wave* superconducting state in itinerant ferromagnets where the pairing is mediated by the exchange of longitudinal spin fluctuations. Even if superconductivity is interpreted as arising from magnetic mediation, it was thought that the superconducting state will occur in the paramagnetic phase. But magnetically mediated superconductivity had not been observed [47]. Some theories predicted the possibility of *s-wave* superconductivity and ferromagnetic order that coexist in the paramagnetic phase but the ferromagnetic fluctuations destroy it near the Curie temperature. Consideration of *s-wave* superconductivity and ferromagnetism was carried out by Suhl [161] and Abrikosov [3] in which the ferromagnetism is due to localized spins. The first experimental observations of coexistence was found in the ferromagnetic metal UGe_2 [145]. The coexistence has also been shown to exist in $ZrZn_2$ [132] and URhGe [6]. Experiments on these three materials show that the same electrons are responsible for both ordered states. But still the exact symmetry of the paired state and the dominant mechanism responsible for the pairing is in question. Although most authors believe there is triplet superconductivity in these materials, the possibility of *s*-wave superconductivity cannot be denied.

Despite the problem of the interplay between superconductivity and ferromagnetism is an open question in the field of the condensed matter, atomic-scale multilayer F/S systems, where the superconducting and ferromagnetic layers coexist, have been realized. For example, $Sm_{1.85}Ce_{0.15}CuO_4$ [163] reveals superconductivity at T_C=23.5 K. In this compound the superconducting layers are separated by two ferromagnetic layers with magnetic moments oriented oppositely. Several years ago, a new class of magnetic superconductors

based on the layered perovskite ruthenocuprate compound $RuSr_2GdCu_2O_8$, comprising CuO_2 bilayers and RuO_2 monolayers, were synthesized [16]. In this compound, the magnetic transition occurs at about $130 - 140$ K and superconductivity appears at T_C=$30 - 50$ K. Recent measurements of the interlayer current in small-sized $RuSr_2GdCu_2O_8$ [119] single crystals showed the intrinsic Josephson effect. Apparently, it is a weak ferromagnetic order which occurs in this compound. Although magnetization measurements provide evidence of a small ferromagnetic component, the neutron-diffraction data on this compound revealed the dominant antiferromagnetic ordering in all three directions [112].

Due to the progress of multilayer preparation methods, the fabrication of artificial atomic-scale F/S superlattices has become possible. An important example is the $YBa_2Cu_3O_7/La_{0.7}Ca_{0.3}MnO_3$ superlattice. The manganite half metallic compound $La_{0.7}Ca_{0.3}MnO_3$ (LCMO) [150] exhibits colossal magnetoresistance and its Curie temperature is about 240 K. The cuprate high-T_C superconductor $YBa_2Cu_3O_7$ (YBCO) with T_C=92 K has a similar lattice constant as LCMO, allowing for the preparation of high quality YBCO/LCMO superlattices with different F and S layer thickness ratios. The proximity effect in these superlattices happens to be long-ranged. For a fixed superconducting layer thickness, the critical temperature is dependent on the LCMO layer thickness. We will present the results of point contact Andreev reflection spectroscopy on compounds like $RuSr_2GdCu_2O_8$ and YBCO/LCMO bilayers in Chapter 4.

In addition in F/S multilayers it has been reported that due to the proximity effect the Cooper pair wave function extends from the superconductor to the ferromagnet with damped oscillatory behavior [35]. This results in many new effects: spatial oscillations of the electron density of states, a non-monotonic dependence of the critical temperature of F/S multilayers and bilayers on the ferromagnet layer thickness, and the realization of "π" Josephson junctions in S/F/S systems. Spin-valve behavior in complex S/F structures gives another example of the interesting interplay between magnetism and superconductivity, an effect that is promising for potential applications. The realization and experimental characterization of S/F/S Josephson junctions with strong ferromagnetic barriers is the subject of Chapter 5.

CHAPTER 2

ELECTRICAL TRANSPORT IN HETEROSTRUCTURES

Ivar Giaever (1961)
....on the naive picture that tunneling is proportional to density of states..

"If a small potential difference is applied between two metals separated by a thin insulating film, a current will flow due to the quantum mechanical tunnel effect. For both metals in the normal state the current voltage characteristic is linear, for one of the metals in the superconducting state the current voltage characteristics becomes non linear... From these changes in the current voltage characteristics, the change in the electron density of the states when a metal goes from its normal to its superconductive state can be inferred" With this observation in 1961 Giaever [66, 67] revolutionized the solid state physics introducing a new tool of investigation to study the superconducting materials. Then his experimental data confirmed the Bardeen-Cooper-Schrieffer theory on the conventional superconductors.

In this Chapter we want to examine different junctions, from the tunneling junctions with a thick barrier to the junctions without barrier, and analyze

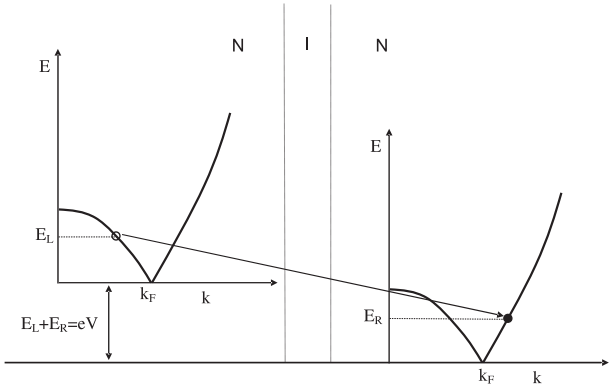

FIGURE 2.1. Excitation tunneling diagram for a Normal metal-Insulator-Normal metal junction. The black circle represents the electron, the other the hole.

their main characteristics necessary to understand the physical properties of the systems that we will study.

2.1. Tunnel junctions

The term *tunneling* is applicable when an electron passes through a region in which the potential is such that a classical particle with the same kinetic energy could not pass. In quantum mechanics, one finds that an electron incident on such a barrier has a certain probability of passing through, depending on the height, the width and the shape of the barrier.

2.1.1. N/I/N junctions

In this section we analyze the tunneling process through a barrier between two normal metals (N/I/N tunneling junction). We suppose to apply a bias V between the metals, this is represented in the excitation-energy diagram by a displacement of the zero-excitation level (Fermi level) (see Fig. 2.1). As illustrated in Fig. 2.1, the metal on the left side is positively biased with respect to that on the right and, as a result, there is a net transfer of electrons from left to right. This transfer is represented by an excitation of a hole in the k space on the left side from which the electron is removed, and an excitation of an electron in the k space on the right side into which the electron is injected. The sum of the excitation energies $E_L + E_R$ for the hole and the electron must be equal to the energy eV provided by the applied bias. A tunneling current consists of a succession of many such pairs of excitations as the electrons cross the barrier. The transition probability per unit time is given by Fermi golden rule:

$$w_{LR} = \frac{2\pi}{\hbar}|T_{LR}|\rho(E_R)\delta(E_R - E_L), \tag{2.1}$$

where $\rho(E_R)$ is the density of states of the metal on the right side and $|T_{RL}|$ is the tunneling matrix element that depends on the properties of the barrier (geometry, size, shape, etc). Now we want to calculate the tunnel current that passes through the junction. We notice that the number of incident electrons on the barrier in the energy range dE is proportional to the occupied states on the left side: $N_L(E - eV)f(E - eV)dE$, where $N_L(E - eV)$ is the density of states of the metal on the left side and $f(E)$ is the Fermi function. The electrons can tunnel in the metal on the right if there are empty states on the right side, so the current will be proportional to $N_R(E)(1 - f(E))$. The total current of the electrons that tunnel from the left side to the right side of the barrier, therefore, will be given summing on the possible full states on the left and the empty states on the right:

$$I_{LR} \propto \int_{-\infty}^{+\infty} |T_{LR}|^2 N_L(E - eV)N_R(E)f(E - eV)[1 - f(E)]dE \tag{2.2}$$

A similar expression is given for the tunneling current from right to left:

$$I_{RL} \propto \int_{-\infty}^{+\infty} |T_{RL}|^2 N_L(E - eV)N_R(E)f(E)[1 - f(E - eV)]dE \tag{2.3}$$

Thus, the net tunneling current will be the difference of the rightward and leftward currents, and, exploiting the symmetry of the tunneling matrix element so $|T_{RL}|^2 = |T_{LR}|^2 = |T|^2$ and considering the area A of the junction, we obtain for the tunneling current the following expression:

$$I = I_{LR} - I_{RL} = \frac{2\pi eA}{\hbar} \int_{-\infty}^{+\infty} |T|^2 N_L(E - eV)N_R(E)[f(E) - f(E - eV)]dE. \tag{2.4}$$

Over a small range of bias voltage, the tunneling matrix element and the densities of states can be considered as constants and removed from the integral. For low temperature, the remaining integral can be shown to be approximately equal to eV, where V is the applied bias. Therefore:

$$I = G_{NN}V, \tag{2.5}$$

where $G_{NN} = (\frac{2\pi eA}{\hbar})|T|^2 N_L(0)N_R(0)$. We have obtained Ohm's law.

2.1.2. N/I/S junctions

We calculate the tunneling current in the case of the tunneling between a Normal metal and a conventional Superconductor (N/I/S junction), in Fig. 2.2 we show the excitation energy diagrams for this junction. An electron in the metal with excitation energy E_L can tunnel into any unoccupied state of the superconductor with energy E_R such that the total energy is conserved:

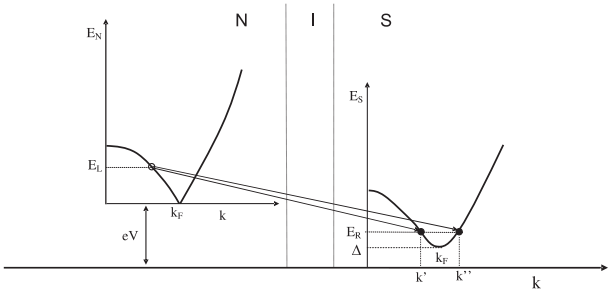

FIGURE 2.2. Excitation tunneling diagram for a Normal metal-Insulator-Superconductor tunneling junction. An electron tunnels into either of the two states, conserving energy.

$E_L + E_R = eV$. We notice that there are two states k' and k'' with the same energy, so the probability that the state k' is empty is the probability that it is not pairwise occupied, $u^2_{k'}$. At the same time the probability that the state k'' is empty is given by $u^2_{k''}$. Assuming the energy gap isotropic ($\Delta'_k = \Delta''_k = \Delta$), $u^2_{k''} = v^2_{k'}$, so the probability of a vacant state is $u^2_{k'} + v^2_{k'} = 1$. Therefore, though the excitations in the superconductor are really in states both above and below k_F, we can calculate tunneling current by considering only states above k_F and taking the vacancy there to be unity.

We can assume that from the normal state to the superconducting state only the density of states changes, so, using the appropriates densities of the states and noting that there are no states in the gap, Eq. 2.4 becomes:

$$I = \frac{2\pi eA}{\hbar} \int_{-\infty}^{+\infty} |T|^2 N_{LN}(E - eV) N_{RS}(E)[f(E) - f(E - eV)]dE. \tag{2.6}$$

where N_{LN} is the density of states of the normal metal, independent from E, and $N_{RS}(E)$ is the density of states of the superconductor. From the BCS theory, for a conventional superconductor, $N_{RS}(E)$ is given by:

$$N_{RS}(E) = \begin{cases} N_{RN} \frac{E}{(E^2 - \Delta^2)^{1/2}} & |E| \geq \Delta \\ 0 & |E| < \Delta, \end{cases} \tag{2.7}$$

in this equation N_{RN} is the density of states of the superconductor in the normal state and the range of energy $E < |\Delta|$ is excluded from the integration.

It is interesting to note that for $T \longrightarrow 0$ the differential conductance yields the measurement of the density of states in the superconductor:

$$G_S(eV) = \frac{dI}{dV}_{T \longrightarrow 0} = \begin{cases} G_{NN} \frac{eV}{((eV)^2 - \Delta^2)^{1/2}} & |eV| \geq \Delta \\ 0 & |eV| < \Delta. \end{cases} \tag{2.8}$$

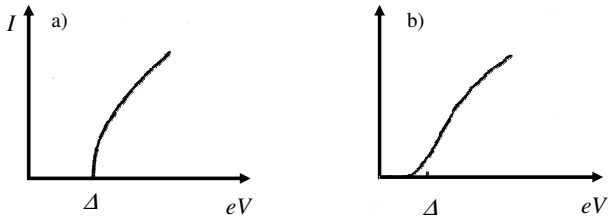

FIGURE 2.3. Current-voltage characteristics at $T = 0$ a) and at $T \neq 0$ b) for a N/I/S tunnel junction.

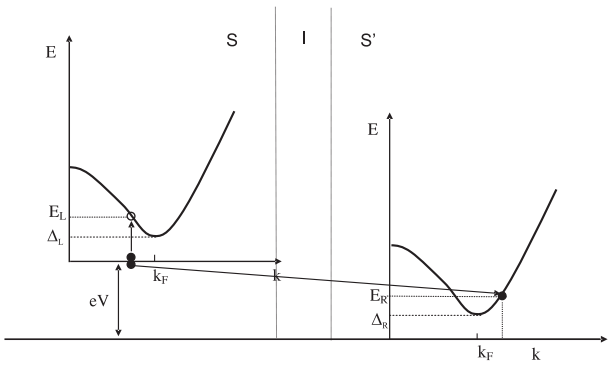

FIGURE 2.4. Tunneling between two superconductors. A hole excitation is created in one superconductor and an electron excitation is created in the other superconductor.

As temperature is increased, caused by thermal fluctuation, the conductance peak decreases in height and becomes broader, giving rise to a finite conductance in the gap region. In addition the conductance maximum moves to higher values of $eV/\Delta(T)$ so the evaluation of the energy gap from the tunneling characteristics is more complicated.

2.1.3. S/I/S' junctions

Now we explain what happens when both electrodes forming the tunneling junction are superconductors, considering the general case with two different superconductors. We have seen that, in the case of tunnel between a normal metal and a superconductor, an electron can tunnel into the states both below and above k_F, but the calculation of the tunneling current can be done by considering only states above k_F and taking the others having a zero probability of occupancy. The same treatment can be done for a Superconductor-Insulator-Superconductor tunneling junction (S/I/S'). In a S/I/S' junction we should consider two processes. A pair can be broken, creating a hole excitation on

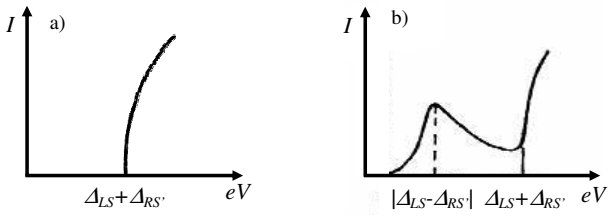

FIGURE 2.5. V-I characteristic of a junction with different superconducting electrodes at $T = 0$ and $T \neq 0$, S and S'.

the side where the pair was and injecting the electron into the other side. The second type is the transfer of an excited electron from one side to the other. The minimum energy required for this process is the sum of the energy gap in the two superconductors, $\Delta_{LS} + \Delta_{RS'}$. Since this energy must be supplied by the external bias no current can flow for $eV < \Delta_{LS} + \Delta_{RS'}$. At larger biases the tunneling current is given by:

(2.9)

$$I_{SS'} = \frac{G_{NN}}{e} \int_{-\infty}^{+\infty} \frac{|E - eV|}{[(eV - E)^2 - \Delta_{LS}^2]^{1/2}} \frac{|E|}{[E^2 - \Delta_{RS'}^2]^{1/2}} [f(E-eV) - f(E)] dE.$$

At higher temperatures the current must be calculated by numerical integration of Eq. 2.9. This result gives a non-zero current for biases $eV < \Delta_{LS} + \Delta_{RS'}$ with a region of negative differential resistance between $eV = |\Delta_{LS} - \Delta_{RS'}|$ and $eV = \Delta_{LS} + \Delta_{RS'}$. In Fig. 2.5 the current vs voltage for $T = 0$ and $T \neq 0$ is shown.

2.1.4. Josephson effect

In the previous section we have analyzed the quasi-particle tunnel in a S/I/S' tunnel junctions, now we explain another interesting effect that can occur: due to the weak coupling existing between the two superconductors, transitions between the two states S and S' are observed. This coupling is essentially related to the finite overlap of the pair wave functions of the two superconductors. This situation was noticed for the first time by Josephson [90] reporting the existence of a current at $V = 0$ (supercurrent). The existence of a supercurrent can be regarded as an extension of the superconducting properties over the whole structure including the barrier. In the framework of energy-momentum diagrams, d.c Josephson tunneling can be described in terms of the tunnel of the Cooper pair, at the Fermi level, from S to S' [15]. The Josephson effect is described by two equations, one for the pair current

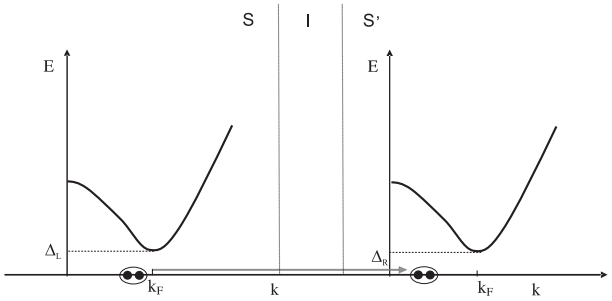

FIGURE 2.6. Tunneling between two superconductors. A hole excitation is created in one superconductor and an electron excitation is created in the other superconductor.

density J_C:

$$J_C = J_0 \sin(\phi_L - \phi_R) = J_0 \sin\phi, \tag{2.10}$$

and the other for the time evolution of the difference of the phase of the two superconductors:

$$\frac{\partial\phi}{\partial t} = \frac{2e}{\hbar}V, \tag{2.11}$$

where J_0 is the critical current density, and ϕ_L and ϕ_R are the macroscopic phases of the two superconductors. Assuming $V = 0$, the phase difference ϕ results, from Eq. 2.11, to be constant, so that a finite current density with a maximum value J_0 can flow through the barrier with zero voltage drop across the junction. A typical current–voltage $(I - V)$ characteristic of a Josephson junction is reported in Fig. 2.1.4. When the current flowing through the junction exceeds its maximum value I_0 (corresponding to the current density J_0 times the dimension of the junctions) a finite voltage suddenly appears across the junction. Indeed a switch occurs from the zero voltage state to the quasi-particle branch of the $I - V$ characteristic.

If we apply a constant voltage $V \neq 0$, it follows by integration of 2.11 that the phase ϕ varies in time as $\phi = \phi_0 + (2e/\hbar)Vt$ and an alternating current appears:

$$J = J_C sin(\phi_0 + \frac{2e}{\hbar}Vt), \tag{2.12}$$

with a frequency $\varpi = 2eV/\hbar$. This is called a.c. Josephson effect. One possibility to observe this phenomenon is to apply a microwave irradiation on the d.c. $I - V$ characteristics of the junction. In fact the microwave signal

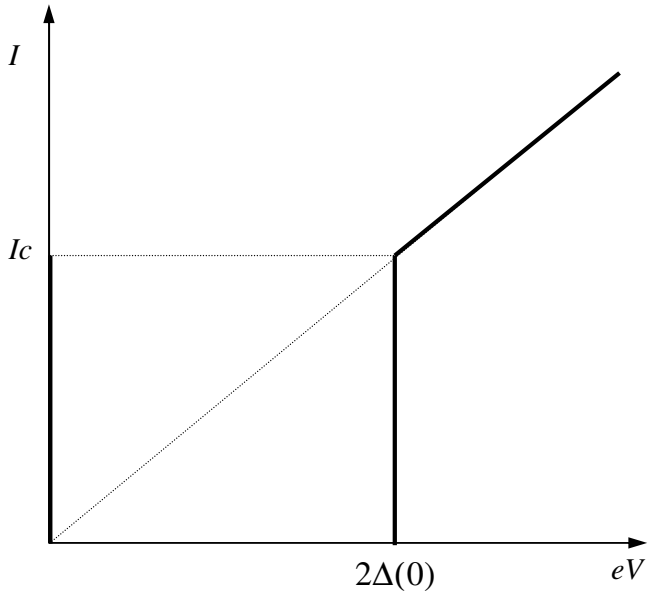

FIGURE 2.7. $I-V$ characteristic for a Josephson junction at T=0.

leads to the appearance of current steps at constants voltages, given by:

$$V_n = \frac{nh}{2e}\nu_0 (n = \pm 1, \pm 2, ...) \tag{2.13}$$

where ν_0 is the frequency of the applied radiation. The first observation of this phenomenon was reported by Shapiro. [152]

If a magnetic field B is applied, it causes a modulation in the junction given by:

$$\nabla_{xy} = \frac{2ed}{\hbar} B \times n_z, \tag{2.14}$$

where n_z is a unit vector perpendicular to the barrier, d is the magnetic thickness given by $d = 2\lambda_J + t$, with λ_J the London penetration distance and t the barrier thickness. In the case of small symmetric junctions, the critical current is found from:

$$I_C(B) = 2J_C \int_{l/2}^{-l/2} f(x) cos \frac{2\pi B_y d}{\Phi_0} x dx \tag{2.15}$$

where $f(x)$ is a positive and even function that describes the junction shape in the region $\pm l/2$ and $\Phi_0 = hc/2e$ is the elementary flux quantum. In general this equation gives an oscillatory function, in particular for rectangular junctions the $I_C(B)$ follows the well known Fraunhofer pattern.

	$A(E)$	$B(E)$
$E < \Delta$	$\frac{\Delta^2}{E^2+(\Delta^2-E^2)(1+2Z^2)^2}$	1-A(E)
$E > \Delta$	$\frac{u_0^2 v_0^2}{\gamma^2}$	$\frac{(u_0^2-v_0^2)Z^2(1+Z^2)}{\gamma^2}$

TABLE 2.1. Andreev reflection [A(E)] and normal reflection [B(E)] probabilities. $\gamma^2 = u_0^2 + Z^2(u_0^2 - v_0^2)$; $u_0^2 = 1 - v_0^2 = \frac{1}{2}[1 + [\frac{E^2-\Delta^2}{E^2}]^{1/2}]$

2.2. Weak links: N/S junctions

Now we want to study what happens when the barrier between the superconductor and the normal metal becomes zero. To understand this geometry, in this section, we review the main results of the original Blonder-Tinkham-Klapwijk (BTK) theoretical model [25], as developed for electronic transport between a normal metal and a conventional BCS superconductor for an arbitrary barrier. We also summarize the Kashiwaya-Tanaka [91] extension for asymmetric *s-wave* and *d-wave* superconductors. Indeed, a close comparison of the calculated conductance spectra is useful for a better understanding of the peculiar transport processes that occur at an N/S interface depending on the symmetry of the superconducting order parameter.

2.2.1. Andreev reflections in *s*-wave and *d*-wave superconductors

Following the original paper, we write the expression of the differential conductance characteristics for a N/S contact that, according to the BTK model[25], is given by:

$$G_{NS}(eV) = \frac{dI(eV)}{dV} = G_{NN} \int_{-\infty}^{+\infty} dE[1 + A(E) - B(E)] \left[-\frac{df(E+eV)}{d(eV)} \right] \tag{2.16}$$

where eV is the applied potential, $G_{NN} = 4/(4 + Z^2)$ is the normal conductance expressed in term of Z, a dimensionless parameter modeling the barrier strength, *f(E)* is the Fermi function and *A(E)* and *B(E)* are, respectively, the Andreev reflection and normal reflection probabilities for an electron approaching the N/S interface (see table 2.1).

Let us briefly explain the phenomenon of Andreev reflections, which plays a crucial role in all our work. In this case, an incoming electron from the normal metal with energy E $< \Delta$ cannot enter into the superconducting electrode and is reflected as a hole in the normal metal, simultaneously adding a Cooper pair to the condensate in the superconductor (Fig. 2.8). This process

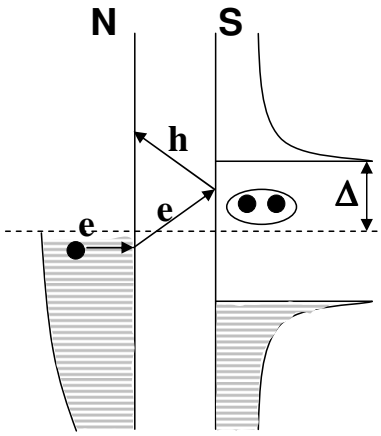

FIGURE 2.8. An electron coming from the normal electrode with energy smaller than the energy gap cannot enter the superconductor. It is reflected as a hole, leaving an extra charge 2e in the superconducting condensate (Andreev reflection).

causes an increase of the conductance around zero bias with a maximum ratio G(V=0)/G$_N$(V$\gg\Delta$)=2 (see Fig. 2.9 (a)). Eq. 2.16 shows indeed that, while ordinary reflections reduce the transport current through the junction, Andreev reflections increase it by transferring two electrons (Cooper pair) in the superconducting electrode on the other side of the barrier. The case $Z = 0$ corresponds to a completely transparent barrier so that the transport current is predominantly due to Andreev reflections. By increasing Z, the Andreev reflections are partially suppressed and the conductance spectra tend to the case of a N/I/S tunnel junction showing peaks at $eV = \pm\Delta$ (Figs. 2.9 (b),(c)).

Recently, Kashiwaya and Tanaka [91] extended the BTK model by considering different symmetries of the order parameter. Indeed, for a *d-wave* superconductor, the electron-like and hole-like quasiparticles, incident at the N/S interface, experience different signs of the order parameter, with formation of Andreev Bound States at the Fermi level along the nodal directions. The presence of Andreev Bound States modifies the transport current and the expression of the differential conductance is given by:

$$G_{NS}(V) = \frac{\int_{-\infty}^{+\infty} dE \int_{-\frac{\pi}{2}}^{+\frac{\pi}{2}} d\varphi\ \sigma(E,\varphi)\cos\varphi \left[-\frac{df(E+eV)}{d(eV)}\right]}{\int_{-\infty}^{+\infty} dE \left[-\frac{df(E+eV)}{d(eV)}\right] \int_{-\frac{\pi}{2}}^{+\frac{\pi}{2}} d\varphi\ \sigma_N(\varphi)\cos(\varphi)}, \tag{2.17}$$

where

$$\sigma(E,\varphi) = \sigma_N(\varphi)\frac{(1+\sigma_N(\varphi))\Gamma_+^2 + (\sigma_N(\varphi)-1)(\Gamma_+\Gamma_-)^2}{(1+(\sigma_N(\varphi)-1)\Gamma_+\Gamma_-)^2}, \tag{2.18}$$

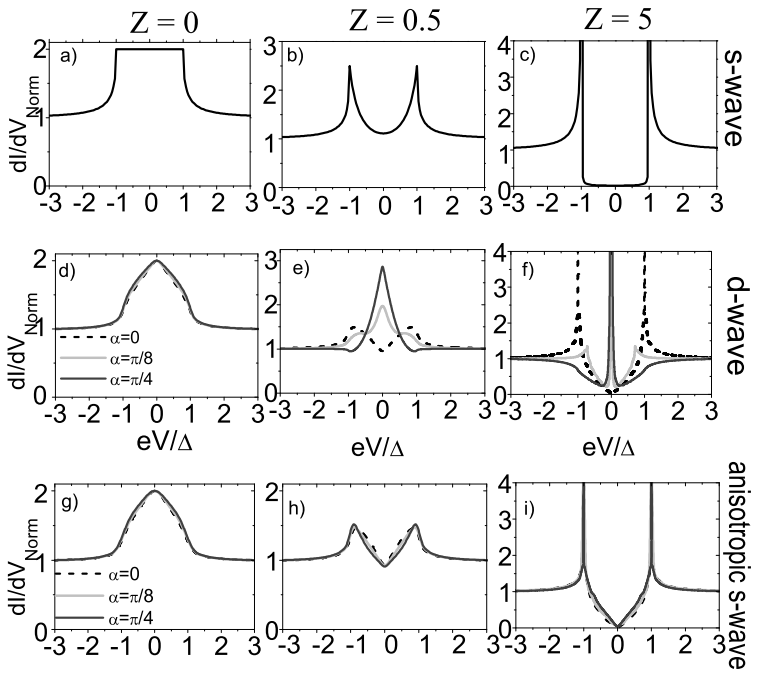

FIGURE 2.9. Conductance characteristics, at low temperatures, for different barriers Z as obtained by the BTK model for a point contact junction between a normal metal and a *s-wave* (a,b,c), a *d-wave*(d,e,f) and an anisotropic *s-wave* superconductor (g,h,i).

is the differential conductance and

$$\sigma_N(\varphi) = \frac{1}{1+\tilde{Z}(\varphi)^2}, \quad \tilde{Z}(\varphi) = Z\cos(\varphi), \tag{2.19}$$

$$\Gamma_\pm = \frac{E-\sqrt{E^2-\Delta_\pm^2}}{\Delta_\pm}, \tag{2.20}$$

$$\Delta_\pm = \Delta\cos[2(\alpha \mp \varphi)]. \tag{2.21}$$

So, at a given energy E, the transport current depends both on the incident angle φ of the electrons at the N/S interface as well as on the orientation angle α, that is the angle between the *a-axis* of the superconducting order parameter and the *x-axis*.[(1)]

[(1)] When applying Eqs. 2.17–2.21 to point contact Andreev reflection (PCAR) experiments, there is no preferential direction of the quasiparticle injection angle φ into the superconductor, so the transport current results by integration over all directions inside a hemisphere weighted by the scattering probability term in the current expression. Moreover, because our experiments deal with polycrystalline samples (as we can see in detail in the Chapter

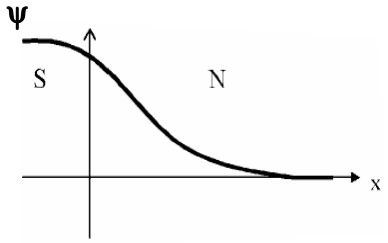

FIGURE 2.10. Behavior of the superconducting order parameter at the N/S interface.

In the case of *d-wave* symmetry, for $Z \to 0$, the conductance curves at low temperatures show a triangular structure centered at $eV = 0$, quite insensitive to variations of α with maximum amplitude $G_{NS}(V = 0)/G_{NN}(V >> \Delta) = 2$ (Fig. 2.9 (d)). However, for higher barriers, the conductance characteristics show dramatic changes as function of α. In particular as soon as $\alpha \neq 0$, the presence of Andreev Bound States at the Fermi level produces strong effects more evident along the nodal direction ($\alpha = \pi/4$) for which $G_{NS}(V = 0)/G_{NN}(V >> \Delta) > 2$ is found (Figs. 2.9 (e),(f)).

For comparison, we report the conductance behavior for anisotropic *s-wave* superconductor, in which only the amplitude of the order parameter varies in the k-space, while the phase remains constant and Eq. 2.21 reduces to:

$$\Delta_+ = \Delta_- = \Delta \cos[2(\alpha - \varphi)]. \tag{2.22}$$

Again, in the limit $Z \to 0$, an increase of the conductance for $E < \Delta$ with a triangular profile is found with maximum amplitude $G_{NS}(V = 0)/G_{NN}(V >> \Delta) = 2$ at zero bias (Fig. 2.9 (g). On the other hand, for higher Z, we obtain tunneling conductance spectra that show the characteristic "V"-shaped profile in comparison to the classical "U"-shaped structure found for an isotropic *s-wave* order parameter (Figs. 2.9 (h),(i)). We notice that in this case all the curves are quite insensitive to variation of the α parameter and a zero bias peak is obtained only for low barriers.

At the N/S interface the superconducting properties can be inducted in the normal metal, due to the penetration of Cooper pairs: this phenomenon is commonly called the *proximity effect*. If the electrons' motion is diffusive, the penetration of the Cooper pairs in the metal is proportional to the thermal diffusion length scale $L \sim \sqrt{D/T}$, where D is the diffusive constant. In the case of a pure metal the characteristic distance is $\xi \sim v_F/T$, where v_F is Fermi velocity. So the order parameter disappears exponentially (see Fig. 2.10).

4), the angle α is a pure average fitting parameter, which depends on the experimental configuration.

Simultaneously the leakage of the Cooper pairs weakens the superconductivity near the interface with the normal metal. This effect is called the *inverse proximity effect*, and results in a decrease of the superconducting transition temperature in a thin layer in contact with a normal metal, with the depression of the superconducting energy gap Δ. If the thickness of a superconducting layer is smaller than the critical one, the proximity effect totally suppresses the superconducting transition. [56]

2.2.2. S/N/S: Subharmonic gap structures

In this subsection we analyze what happens when two superconductors are connected by a "weak link" of any physical nature (normal metal, semiconductor, geometrical constriction, etc.). The main features in the current voltage characteristics of such junctions are the presence of Josephson current and Subharmonic Gap Structures (SGS). The physical origin of the Josephson effect with weak link can be understood by resorting to the Andreev reflection [5] processes of quasiparticles with energy smaller than the superconducting

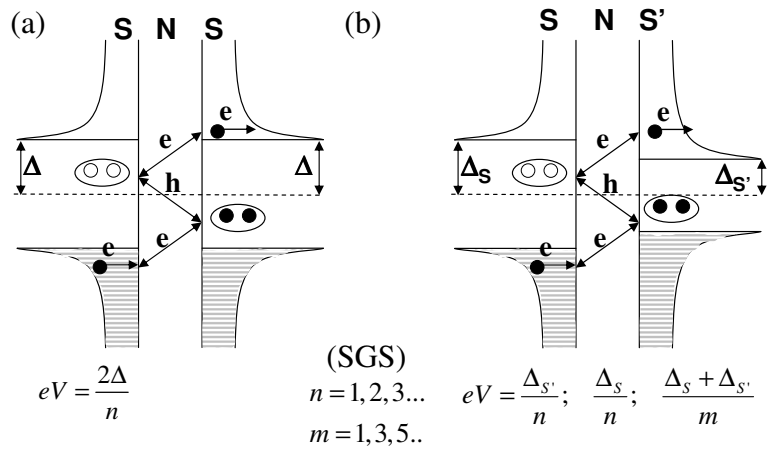

FIGURE 2.11. In the case of superconducting electrodes (a), an electron is reflected back or transmitted. For voltages $eV \leq \Delta$ the Andreev reflected hole can not find an empty state in the left electrode but is Andreev reflected in turn as an electron. For energies $2\Delta/3 \leq eV < \Delta/2$ the electron finds an empty state in the right electrode, three charges are transferred in this process (Multiple Andreev Reflections). For smaller voltages, MAR processes that transfer four or more electron charges carry the current. (b) In asymmetric tunnel junctions the conductance enhancements appear at energies $(\Delta_S + \Delta_{S'})/m$, with m=1,3,5,..., Δ_S/n and $\Delta_{S'}/n$, with n=1,2,3,...

energy gap. In the weak link region, an electron impinging on one of the interfaces is Andreev reflected and converted into a hole moving in the opposite direction, thus generating a Cooper pair at the interface, and is converted back to an electron, leading to the destruction of the Cooper pair in the other S. As a result of this cycle, a pair of correlated electrons is transferred from one S to another, creating a supercurrent flow across the junction. The SGS have been observed in junctions between identical superconductors as conductance peaks appearing at bias voltages V=2Δ/ne with n = 1,2,3,... [14, 131, 146] and different mechanisms have been suggested to describe this phenomenon: initially, correctly the multiparticle tunneling model [149] was able to predict the voltage positions of the SGS. Successively, a satisfactory explanation of the subgap structures has been proposed in the BTK theory[25] and then extended in the OBTK model by Octavio et al. [124]: SGS are originating from multiple Andreev reflections at the superconductor–normal-metal interfaces, see Fig. 4.15(c). This model has been then generalized by Arnold [7] to any kind of junctions between two superconductors and in particular to the superconducting point contacts by using a modified tunneling Hamiltonian approach. It is now understood that the multiparticle tunneling model represents the low transparency perturbation theory limit of the more general process of multiple Andreev reflections [30].

Unlike symmetric junctions, very few reports in the literature address the behavior of asymmetric S–c–S' constrictions, see Fig. 4.15(d), both theoretically [124, 84] and experimentally [143, 184]. In particular, calculation of the current-voltage relations for ballistic S/N/S' junctions by means of transmission formalism [84] showed that, for finite temperatures, SGS appear in the differential conductance at energies $eV_n = (\Delta_S + \Delta_{S'})/m$,with m=1,3,5,..., $eV_n = \Delta_S/n$, and $eV_n = \Delta_{S'}/n$, with n=1,2,3,...

2.3. F/S junctions

The aim of this section is to give an outline of the physics of the Ferromagnetic-Superconducting (F/S) interfaces. Andreev reflection plays an important role to understand the transport process in F/S junctions. The Andreev reflection near the Fermi level preserves energy and momentum but does not preserve spin, in other words the incoming electron and the reflected hole have opposite spin. This is irrelevant for the transport in N/S junctions due to the spin-rotation symmetry. On the other hand at F/S interfaces, since the spin-up and spin-down bands in F are different, the spin flipping changes the conductance profile. In particular in fully spin-polarized metals all carriers have the same spin and the Andreev reflection is totaly suppressed; therefore, at zero bias voltage the normalized conductance becomes zero (see Fig. 2.12). In general,

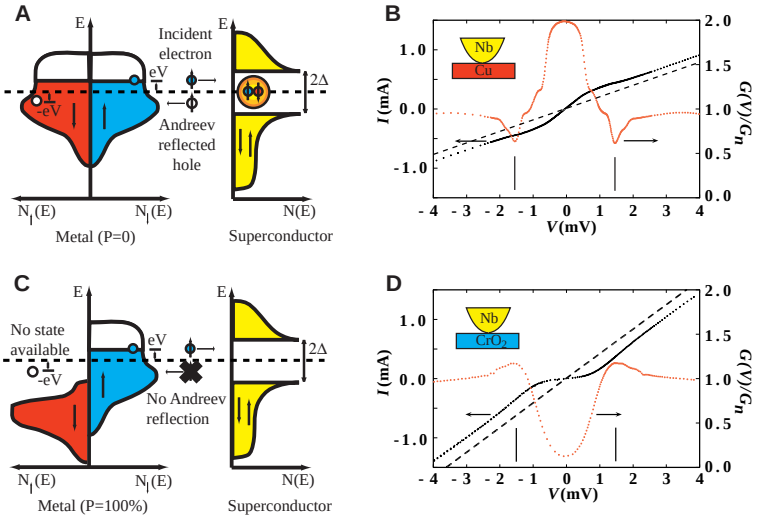

FIGURE 2.12. Andreev reflection process for a metal with $P = 0$ (A) and $P = 100\%$ (C); experimental measurements of a N/S interface (B) and F/S junction (D). Figure adapted from Ref.[158].

for arbitrary polarization P, it can easily be shown that

$$\frac{G_{FS}(0)}{G_{FN}} = 2(1 - P) \tag{2.23}$$

where, in terms of the spin-up $N_\uparrow$ and spin-down $N_\downarrow$ electrons, the spin polarization is defined as

$$P = \frac{(N_\uparrow - N_\downarrow)}{(N_\uparrow + N \downarrow)}, \tag{2.24}$$

From this analysis it has been shown that the point contact measurements based on the Andreev reflection process give a quantitative estimation of the polarization of the ferromagnetic material [158, 160]. In fact from the reduction of the zero bias conductance peak it is possible with a modified BTK model to estimate the polarization P.

In a ferromagnet in proximity to a superconductor, the coherence length ξ_F, due to the presence of the exchange field E_{ex}, is given by:

$$\xi_F = \sqrt{\frac{D\hbar}{2(\pi K_B T + iE_{ex})}}, \tag{2.25}$$

where D is the diffusive coefficient. If the exchange energy is large compared to the temperature $Eex > k_B T$ the coherence length is much shorter than in the case of the N/S proximity effect. In addition to the reduced coherence length compared to typical N/S structures, a second characteristic property

arises from the complex nature of the coherence length: the induced pair amplitude oscillates spatially in the ferromagnetic metal as a consequence of the exchange field acting upon the spins of the two electrons forming a Cooper-pair [37, 39, 139, 140] (see Fig. 2.13). This oscillation includes a change of sign and by using appropriate values for the exchange energy and F-layer thickness, negative coupling can be realized. This effect can be exploited in order to fabricate ferromagnetic π-junctions. We refer to the state corresponding to a positive sign of the real part of the order parameter as "0-state" and that corresponding to a negative sign of the order parameter as "π-state".

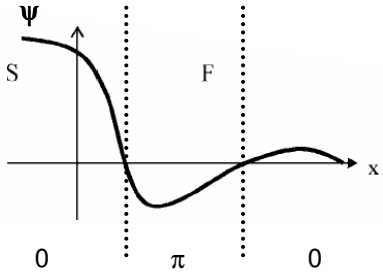

FIGURE 2.13. Oscillatory behavior of the exponentially decay of the superconducting order parameter at the F-S interface.

Demler et al. [54] gave a qualitative picture of this oscillatory character. They considered a Cooper pair transported adiabatically across an F/S interface, with its electron momenta aligned with the interface normal direction. The pair entering in the F region decays exponentially on the length scale of the normal metal coherence length. Then the up-spin electron, oriented along the exchange field, decreases its energy by $h = E_{ex}/\hbar$, where E_{ex} is the exchange energy of the F layer. On the other hand, the down-spin electron increases its energy by E_{ex}. To compensate this energy variation, the up-spin electron increases its kinetic energy, while the down-spin electron decreases its kinetic energy. As a result the Cooper pair acquires a center-of-mass momentum $Q = 2E_{ex}/v_F$, which implies the modulation of the order parameter with period $\pi v_F/E_{ex}$, where v_F is the Fermi velocity.

As a consequence of the oscillations of the order parameter, a similar oscillatory behavior is observed for the density of states. This behavior can be explained by considering the spin effect on the mechanism of Andreev reflections[35].

The process is illustrated in Fig. 2.14 using the energy-momentum dispersion law of the normal metal: in the previous section we have explained the Andreev Reflections at a N/S interface, and we have seen that an incoming electron in a normal metal N with energy lower than Δ_S from the Fermi level is reflected into a hole at the N/S interface. If the normal layer is very thin

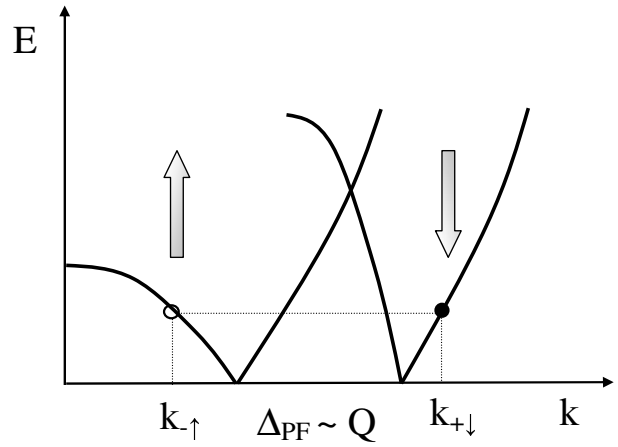

FIGURE 2.14. Schematic of the Andreev reflection process in a F/S junction, the momentum shift, Δ_{pF}, is dominated by the spin splitting of the up and down bands.

the density of states in N is close to that of the Cooper pair reservoir. The situation is strongly modified if the normal metal is ferromagnetic. As Andreev reflections invert spin-up into spin-down quasiparticles and vice versa, the total momentum difference includes the spin splitting of the conduction band: $\triangle P_F \simeq Q$. The density of states is modified in a thin layer on the order of ξ_F. In particular, the interference between the electron and hole wave functions produces an oscillating term in the superconducting density of states with period $E_{ex}/\hbar v_F$. This effect has been observed experimentally by Kontos et al. [97]

2.3.1. π-junctions

Due to the spatially oscillating induced pair amplitude in F/S proximity structures it is possible to realize negative coupling of two superconductors across a ferromagnetic weak link (S/F/S Josephson junctions). In this case of negative coupling, the critical current across the junction is reversed when compared to the normal case giving rise to an inverted current-phase relation. Because they are characterized by an intrinsic phase shift of π, these junctions are called π-junctions.

One of the manifestations of the π phase is a non-monotonic variation of the critical temperature and the critical current, with the variation of the ferromagnetic layer thickness (t_F) [35]. Referring to the current-phase relation $I_C = I_0 sin\phi$ (Eq. 2.11), for a S/I/S Josephson junction the constant $I_0 > 0$ and the minimum energy is obtained for $\phi = 0$. In the case of a S/F/S Josephson junctions the constant I_0 can change its sign from positive

to negative indicating the transition from the 0-state to π-state. Physically the changing in sign of I_0 is a consequence of a phase change in the electron pair wave function induced in the F layer by the proximity effect. Experimentally, measurements of I_C are insensitive to the sign of I_0 hence the absolute I_0 is measured, so we can reveal a non-monotonic behavior of the critical current as a function of the F layer thickness. The vanishing of critical current marks the transition from 0 to π state. The dependence of the critical current on the thickness of the ferromagnetic layer in S/I/F/S junctions has been experimentally investigated by Kontos et al. [97]. The quantitative analysis of the S/F/S junctions is rather complicated, because the ferromagnetic layer can modify the superconductivity at the F/S interface. Then other parameters, such as the boundary transparency, the electron mean free path, the magnetic scattering, etc can affect the critical current. It is outside the purpose of this dissertation to derive explicitly the expression of the critical current as a function of the F layer, for the interested reader we refer to this review [35].

The majority of experimental studies to date have concentrated on weak ferromagnets where $E_{ex} \sim K_B T_c$ resulting in multiple oscillations in I_C with temperature and t_F. In the case of strong ferromagnets, where $T_{Curie} >> T_C$, only oscillations of I_C with t_F, and not with temperature, are observed. In this work (Chapter 5) we will present the study of the oscillations of the critical current as a function of t_F for S/F/S Josephson junctions with strong ferromagnetic barriers.

The generic expression of the critical current as a function of F layer is given by:

$$I_c R_N(t_F) = I_c R_N(t_0) \left| \frac{\sin \frac{t_F - d_1}{\xi_2}}{\sin \frac{t_F - t_0}{\xi_1}} \right| \exp\left\{ \frac{t_0 - t_F}{\xi_1} \right\}, \tag{2.26}$$

where t_1 is the thickness of the ferromagnet corresponding to the first minimum and $I_C R_N(t_0)$ is the first experimental value of $I_C R_N$ (R_N is the normal state resistance), and ξ_1 and ξ_2 are the two fitting parameters. Eq. 2.26 ranges in the clean and in the dirty limit. In particular, in clean limit, $t_F < L$ where L is the mean free path of the F layer, $\xi_2 = v_F \hbar / 2E_{ex}$. In this way, known ξ_2 and estimating the Fermi velocity from reported values in literature, one can calculate the exchange energy of the ferromagnetic barrier.

Then, in the case of clean limit the oscillations of $I_C R_N$ *vs* t_F can be modeled by a simpler theoretical model [36] given by:

$$I_c R_N \propto \frac{|\sin(2E_{ex} t_F / \hbar v_f)|}{2E_{ex} d_F / \hbar v_f}, \tag{2.27}$$

where in this case the two fitting parameters are v_F and E_{ex}.

On the other hand, in dirty limit $t_F > L$ we can model the oscillations [22] by the following formula:

$$I_C R_N \propto | \, Re \sum_{\omega_m > 0} \frac{\Delta^2}{\Delta^2 + \omega_m^2} \int_{-1}^{1} \frac{\mu}{\sinh(k_\omega t_F / \mu L)} d\mu \, |, \tag{2.28}$$

where Δ is the superconducting order parameter, ω_m is the Matsubara frequency and is given by $\omega_m = \pi T k_B (2m + 1)$ where T is the transmission coefficient and m is an integer number. $k_\omega = (1 + 2 \mid \omega_m \mid \tau/\hbar) - 2iE_{ex}\tau/\hbar$ and $\mu = \cos\theta$ where θ is the angle the momentum vector makes relative to the distance normal to the F-S interface. L is given by $v_F \tau$ and τ is the momentum relaxation time. In this case the fitting parameters are v_F, E_{ex} and the mean free path L of the ferromagnetic layer.

PART II

EXPERIMENTS

CHAPTER 3

EXPERIMENTAL METHODS AND INSTRUMENTAL APPARATUSES

Galileo Galilei (1564-1642)
...All truths are easy to understand once they are discovered;
the point is to discover them.....

In this Chapter a brief overview of the instruments that we have used in this work is presented. We begin with the description of the experimental methods for the fabrication and realization of the Josephson devices, starting from the choice of the substrates and including the sputtering system, the photolithography, the ion milling and the focused ion beam. Then we describe the measurement system to investigate the magnetic and the transport properties of the devices. At the end, in the last section we introduce the point contact Andreev reflection (PCAR) spectroscopy set up.

3.1. Fabrication of Josephson junctions

3.1.1. Choice of the substrates

To produce good junctions we need to consider all the aspects of the preparation, starting from the choice of the substrates. The substrates should be good insulators to avoid shorting-out high resistance devices. They should be extremely flat, have a high thermal conductivity, good stability and have good adhesion properties in order not to alter the surface condition and properties of the junctions. For its favorable properties in our junction we have used silicon wafers (100) with 250 nm SiO_2 on the surface. The importance of clean substrate surfaces has a critical impact on the performance of the device, so before the preparation of the junction a careful cleaning of the silicon substrates is necessary. The silicon wafer is put on a glass plate using hot wax. Using a diamond edged circular saw, the silicon wafer is cut to form $10 \times 5 \text{mm}^2$ chips and 5×5 mm^2 chips for the magnetic measurements. The saw is set to high rotation speed and advanced slowly in order to prevent the wrong crash of the substrate. The chips, so realized, are heated to separate them from the glass plate and bathed in Chloroform and ultrasonically cleaned for at least 15 minutes to remove the wax. After this bath, the chips are bathed in Acetone and ultrasonically cleaned for additional 15 minutes. Before loading them on the sputtering system the chips are cleaned with acetone.

3.1.2. Sputtering system: MarkIII

The heterostructures presented in Chapter 5 of this work have been deposited by d.c. magnetron sputtering in an Ar atmosphere at 1.5 Pa. The sputtering system that we have used is MarkIII system (from the Device Materials group, University of Cambridge (UK)). In Fig. 3.1 we show a scheme of the system. The main chamber is a cylinder with an opening top, in which the flange with the magnetrons and sample holder is set. The chamber is surrounded by a cavity that is the line for the liquid nitrogen[(1)] and by an outer chamber. The outer chamber is connected to the roughing line through a roughing valve and to the diffusion pump through a gate valve. The diffusion pump is connected to the rotary pump through the backing line. The roughing line and the backing line use the same rotary pump. An Ar tank is connected to the rotary pump for roughing and to the outer chamber for diffusion pumping. During the deposition Ar, with a purity better than 99.9% is fed into the inner chamber through a needle valve. The deposition pressure and the Ar flow rate are adjusted by both the needle valve and the gate valve

[(1)] The purpose of this arrangement is to cool the chambers with liquid nitrogen during the final stage of evacuation. This cooling encourages absorption of molecules into the walls, thereby lowering the pressure.

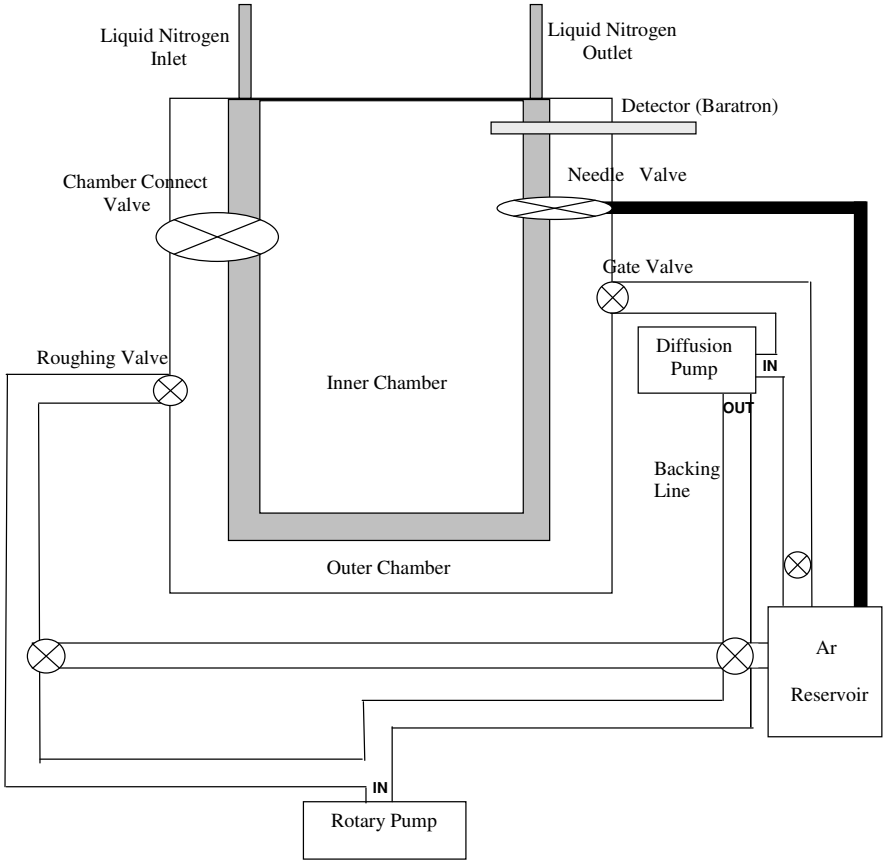

FIGURE 3.1. A scheme of the deposition system (MARK III magnetron dc sputtering).

of the diffusion pump. The system is furnished with a detector to measure and control the pressure in the chamber. The flange was bolted down onto the inner chamber, sealed with a copper gasket. The chamber was evacuated overnight with the diffusion pump. The chamber and gas reservoir were heated for 6 hours, to permit the out-gassing from the walls of the system and flange. In the morning the bolts holding the flange were tightened and the pressure checked with a mass spectrometer. The pressure was generally found to be approximately 5×10^{-8} mBar. The magnetron cooling water was then connected and the liquid nitrogen jacket filled. The system was pumped for a further 1.5-2 hours; the ultrahigh vacuum base pressure achieved was generally 2×10^{-9} mBar.

3.1.2.1. Photolithography

Photolithography is the process of transferring geometric shapes on a mask to the surface of our junctions: Si/SiO_2/Film. The steps involved in the photolithographic process are wafer cleaning; photo-resist application; mask alignment; exposure and development.

In the first step, the heterostructures are chemically cleaned using acetone and nitrogen airgun to remove particulate matter on the surface as well as any traces of organic, ionic, and metallic impurities. After cleaning, positive Hoechst AZ-1529 photo-resist is applied to the surface of the structure. A standard method for applying photo-resist is High-speed centrifugal whirling of the wafers, in our case we use a spin of 6000rpm for 45 seconds. This technique, known as "Spin Coating", produces a thin uniform layer of photo-resist of about 2μm on the junction surface. After the "Spin Coating" the sample are then baked for 1 minute at 100°C in an oven placed on a hotplate. One of the most important steps in the photolithography process is mask alignment. A mask or "photomask" is a square glass plate with a patterned emulsion of metal film on one side. The mask is aligned with the wafer, so that the pattern can be transferred onto the wafer surface. Each mask after the first one must be aligned to the previous pattern. Once the mask has been accurately aligned with the pattern on the wafer's surface, the photo-resist is exposed through the pattern on the mask with a high intensity ultraviolet light. The last step in the photolithographic process is the development, the time of the development depends on the geometry that we want to use. All the chips, so realized, are examined under a light microscope.

3.1.3. Ion Milling

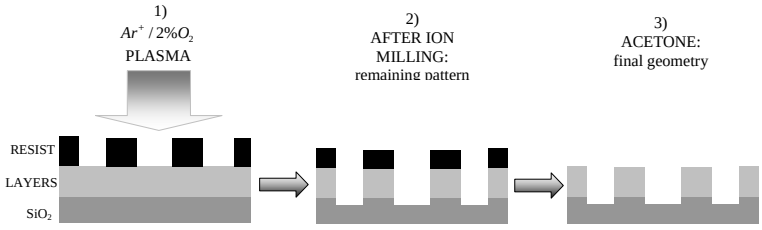

FIGURE 3.2. A schematic illustration of the ion milling process.

To ion mill away the unwanted metal from the chip surface, we used a turbo-pumped system fitted with a load-lock on the chip with the resist pattern. Argon ions ($Ar^+/2\%O_2$) from a plasma are accelerated at the sample which mills the metallization away with a partial pressure of $\sim 4 \times 10^{-2}$ Pa. The

patterned resist acts as a thick layer of protection against the bombarding ions. Regions not covered in resist are therefore milled away, and when the resist is dissolved, the desired pattern remains in the film. The calibration of the milling conditions is necessary to ensure the resist is not totally milled away during this process. During this process the sample stage was water cooled, and rotated continuously to ensure uniform milling. At the end of the process the remaining resist is dissolved in acetone. In Fig. 3.2 there is a schematic illustration of the ion milling process.

3.1.4. FIB

The focused ion beam (FIB) technique is widely used in the semiconductor research and new applications include ion lithography and applications related to micromachining (for a review see [126]). The FIB systems have several functions, for example Ion milling to define micrometric junctions, end point detection (EPD) technique used to identify different materials measuring the current signal to the ground while ion milling and the imaging. In this work we have used a FEI 200 series type FIB for milling and imaging of our junctions.

3.1.4.1. Fib system. — The most important components of the FIB system are: the ion column, the work chamber, the vacuum system, the gas system and the workstation to control the FIB's operations.

A schematic diagram of a FIB ion column is shown in Fig. 3.3 [142]. The structure of the column is similar to that of a scanning electron microscope, the major difference being the use of a gallium ion (Ga^+) beam instead of an electron beam. A vacuum of about 1×10^{-7} mBar is maintained inside the column. The ion beam is generated from a liquid-metal ion source (LMIS) by the application of a strong electric field. This electric field causes the emission of positively charged ions from a liquid gallium cone, which is formed on the tip of a tungsten needle. A typical extraction voltage is 7000 Volt. The extraction current under normal operating conditions is 2μA. After a first refinement through the spray aperture, the ion beam is condensed in the first electrostatic lens. The upper octopole then adjusts the beam stigmatism. The ion beam energy is typically between 10 and 50 keV, with beam currents varying between 1 pA and 10 nA. Using the variable aperture mechanism, the beam current can be varied over four decades, allowing both a fine beam for high-resolution imaging on sensitive samples and a heavy beam for fast and rough milling. Blanking of the beam is accomplished by the blanking deflector and aperture, while the lower octopole is used for raster scanning the beam over the sample in a user-defined pattern. In the second electrostatic lens, the beam is focused to a fine spot, enabling a best resolution in the sub 10 nm range. The multichannel plate (MCP) is used to collect secondary particles for imaging. The samples that are treated by a FIB are mounted on a motorized

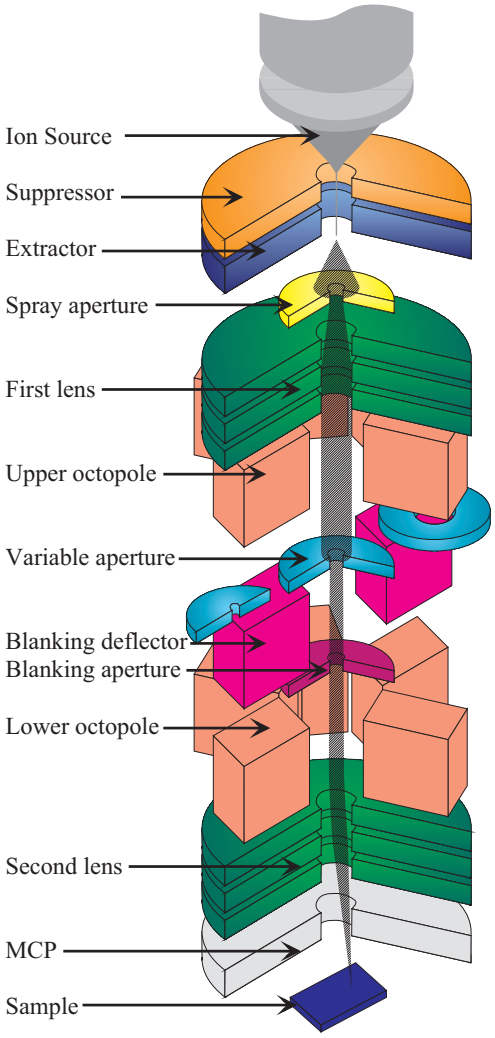

FIGURE 3.3. Schematic diagram of the FIB ion column. Details are in the text. Figure adapted from [142]

five-axis stage, inside the work chamber. Under normal operating conditions, inside this stainless-steel chamber a vacuum in the low 10^{-7} mBar range is maintained. Loading and unloading of the samples is usually done through a loadlock, in order to preserve the vacuum inside the work chamber as much as possible. It typically takes a few minutes to load or unload a sample. A system of vacuum pumps is needed to maintain the vacuum inside the column and the work chamber. A fore pump is used in combination with a turbo pump

for pumping the work chamber. The ion column is additionally provided with one or two ion pumps. A gas cabinet containing all applicable gases is present outside the vacuum chamber. The gas containers are connected to a so called nozzle assembly inside the vacuum chamber through an appropriate piping system. The gases are used for faster and more selective etching, as well as for the deposition of materials. Then, all operations such as loading and unloading of samples (partly), manipulating the stage, controlling valves for gas delivery, turning on and off pumps and manipulating the ion beam are carried out via software. Indeed, the complete user interface is realized by means of a computer workstation.

3.1.4.2. Imaging. — During the FIB imaging the primary beam is scanned across the sample as a raster, which consists of a series of lines in the horizontal (X) axis, shifted slightly from one another in the vertical (Y) axis. As the beam scans over the sample, secondary electrons and secondary ions that are generated by the sample are detected and the information is stored in the computer; the image is generated from this stored information (see Fig. 3.4 (a)). The monitor displays the image at TV rate but the information update in the computer occurs only at the beam scan rate. There are three different types of image quality: high (1024 x 1024 pixel), medium (512 x 512 pixel) and low (256 x 256 pixel) (Source: FIB Manual for FEI 200 (1996)). The best resolution of FIB images equals the minimum ion beam spot size, i.e. below 10 nm.

3.1.4.3. Milling. — Promising work concerning FIB milling for micromachining applications has been published, such as tunneling gap milling, channel and cantilever.

The removal of sample material is achieved using a high ion current beam. The result is a physical sputtering of sample material, as illustrated schematically in Fig. 3.4 (b). By scanning the beam over the substrate, an arbitrary shape can be etched. It is difficult to calculate directly the etching rate, because, it depends on the scanning style and re-deposition, which drastically reduces the effective etching rate. Furthermore the sputtering yield is dependent on the angle of incidence: it roughly increases with $1/cos(\vartheta)$, with ϑ the angle between the surface normal and the ion beam direction. The milling process is monitored through the "end-point detection"; this is a realtime graph of the average brightness in the milling area. An insulator will appear darker than a conductor since the secondary electron yield of the latter is much higher. So the metal is the high-intensity part. The resolution of the milling process is a few tens of nanometers.

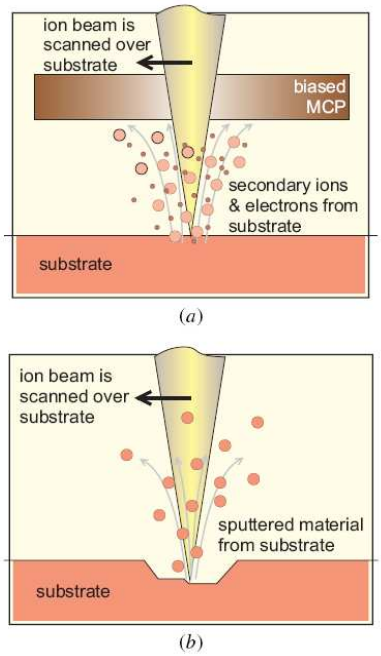

FIGURE 3.4. Schematic representation of imaging (a) and the milling (b) using a FIB system. Figure adapted from [142]

3.2. Electrical and magnetic measurement set ups

3.2.1. Vibrating Sample Magnetometer. — Magnetic properties of our samples are investigated using a Vibrating Sample Magnetometer (VSM) [61]. It is basically a comparator, which measures the difference in induction between a region of space with and without the sample (for more details see Ref.[62]).

In Fig. 3.5 we show a scheme of the mechanism of a VSM. The sample, positioned at the centering of the coils, is oscillated vertically in a region of uniform field. The AC signal induced in the pick-up coils (according to the Faraday law of electromagnetic induction) by the magnetic field of the sample is compared with the signal from a reference sample, and is converted to a number proportional to the magnetic moment, so it gives a direct measure of the magnetization M. Then a comparative analysis of other magnetic properties including coercivity and the magnetization reversal process is also possible. The advantages of this technique are that it is non-destructive, has a high sensitivity at about 10^{-6} emu, and is easy to operate.

3.2.2. Point contact probe and conductance measurements. — The PCAR probe used in this work to investigate the conductance curves of N/S

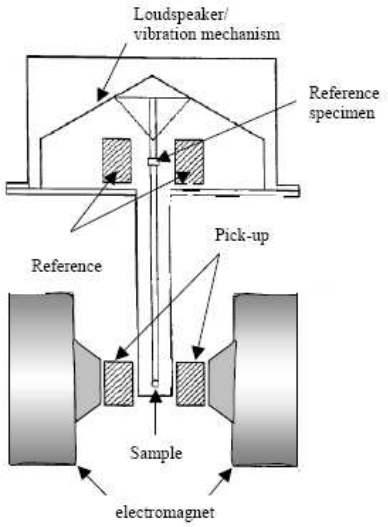

FIGURE 3.5. Simplified scheme of the Vibrating Sample Magnetometer (VSM)

and F/S junctions, is a home-built set up, constituted by three micrometric screws, each driven by its own crank. Two screws allow to vary the distance between tip and sample, with a precision of $1\mu m$ and $0.1\mu m$, respectively. The third screw is devoted to change the inclination of the sample holder varying the contact area on the sample surface. The vertical movement of the tip allowed the tuning of the contact resistance from tunneling regime to metallic contact. Our experimental setup resulted to be extremely stable, showing no relevant effects of thermal contraction, so that in many cases it was possible to vary the junction temperature without affecting the contact geometry. A scheme of our PCAR probe is shown in Fig. 3.6.

To limit surface degradation, after the mounting, the PC inset was placed in liquid He^4, immediately. The contacts were established by driving the tip into the sample surface at low temperatures. Current and dI/dV *vs* V characteristics were measured by using a standard four-probe method and a lock-in technique by superimposing a small ac-modulation to a slowly varying bias voltage. Each measurement comprised two successive cycles in order to check for the absence of heating hysteresis effects [122, 70]. The "Tunneling-Current" (written in LabVIEW^{TM} by F. Bobba and F. Giubileo) software was used to display and control the measurements. All measurements were performed in the temperature range between 4.2 K and up to the critical current of the sample. An in-plane solenoid is mounted on the probe to enable magnetic measurements.

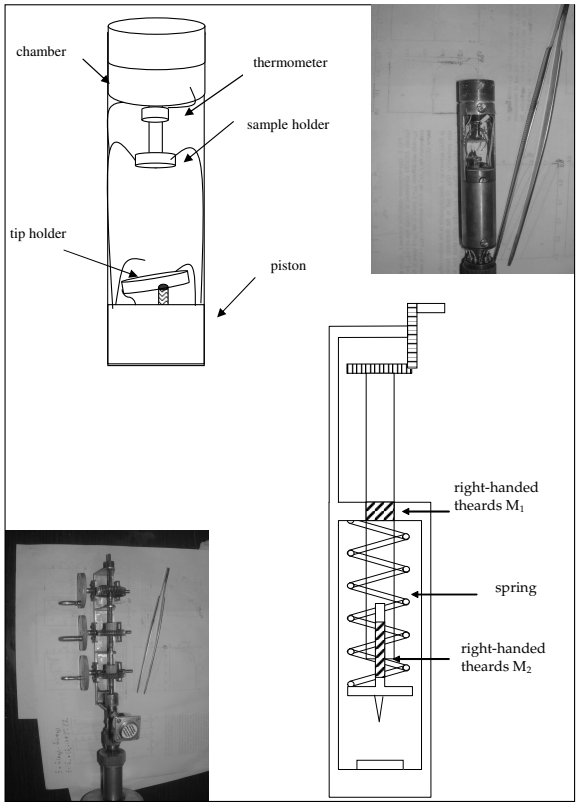

FIGURE 3.6. Illustrative scheme of our PCAR probe. Close-ups show the sample holder and the micrometric screws that allow to vary the distance between tip and sample.

3.2.3. Josephson transport measurements. — The electrical measurements on the Josephson devices have been done with a four-terminal technique. Chips were set to a copper chip holder with silver conducting paint. The contact pads of the chip were wirebonded to the copper pads of the chip holder using an ultrasonic wirebonder with 25 μm diameter Al wire. The probe consists of a diode thermometer, heating element, in-plane solenoid and out-of plane Helmholtz pair for applying magnetic fields, ($0 - 80$ mT at 4.2 K), and a microwave antenna ($12 - 18$ GHz). A low noise current and voltage source, (giving a typical noise level of $0.5 - 1$ μV in a 10 kHz bandwidth), applied a quasi-d.c. (~ 15 Hz) sinusoidal current output. A metal shield was placed over the end of the probe to reduce stray magnetic field. The "Dualscope" (written in LabVIEW$^{\text{TM}}$ by G. Burnell) software was used to display and control the measurements.

A lock-in amplifier allowed the measurement of voltage signals as low as 1 nV. A simple op-amp adder box was used to combine the lock-in reference oscillation (in the range $5 - 30$ mV at 1 kHz), to a d.c. voltage output of the analogue-to-digital card, which was used to control the current source. The d.c. offset was then ramped by the software to obtain the differential resistance as a function of bias current.

CHAPTER 4

POINT CONTACT ANDREEV REFLECTION SPECTROSCOPY ON NOVEL SUPERCONDUCTORS AND HYBRID F/S SYSTEMS

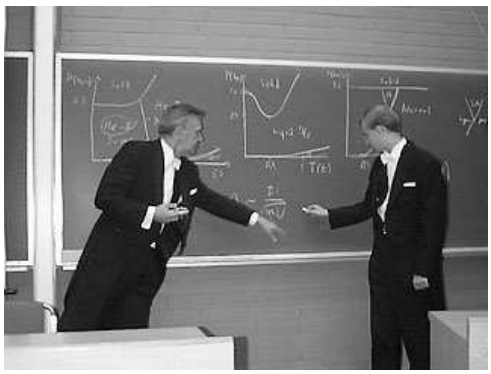

Alexander Andreev (1964)
...in the opposite limit, in which there is no barrier at the interface, the key to understanding the current transfer process is a novel reflection...

PCAR spectroscopy [58] is a versatile technique widely used to study the basic properties of superconductors, such as the density of states at the Fermi level and the superconducting energy gap. The technique consists in establishing a contact between a tip of a normal metal (N) and a superconducting sample (S), thus forming a small contact area that is a "Point Contact" junction. By varying the distance and/or the pressure between tip and sample it is possible to obtain different tunnel barriers, that is different conductance regimes. Indeed, quasiparticle tunnel spectroscopy is obtained for high barriers, while PCAR spectroscopy is achieved in case of low barriers. Often in the experiments, intermediate regimes are realized, in which through the N/S contact both quasi-particle tunneling and Andreev reflection processes occur.

In this Chapter we present the PCAR conductance spectra obtained on novel high-T_C superconductors such as MgB_2 [S2,S8] and $RuSr_2GdCu_2O_8$ (Ru-1212) [S1,S3,S4], in order to investigate the symmetry of the order parameter. The investigation of the symmetry of the order parameter is a crucial point to identify the pairing state and thus represents an important step towards the possible development of the microscopic theory of high temperature superconductors. The MgB_2 compound presents a *s-wave* symmetry of the order parameter and two superconducting energy gaps, while the our analysis evidences for Ru-1212 a *d-wave* symmetry of the superconducting energy gap, in addition the coexistence of the superconducting phase and the magnetic order induces peculiar feature in the conductance spectra of this latter material. This interplay between superconductivity and magnetism has been further investigated by analyzing the conductance spectra obtained on artificial heterostructures constituted by a high-T_C superconductor ($YBa_2Cu_3O_{7-x}$) and a colossal-magnetoresistance material ($La_{0.7}Ca_{0.3}MnO_3$) [S5,S7], in which case the inhibition of the superconducting properties has been related to a partial polarization of the magnetic layer.

4.1. Subharmonic gap structures and Josephson effect in MgB_2/Nb micro-constrictions

The discovery of superconductivity in the binary intermetallic MgB_2 compound [120] has given rise to a considerable effort in the condensed matter community in the last years. Besides the great interest in understanding the new physics originating from the multiband nature of this material, attention has been paid to the attractive potential applications in superconducting electronics, because of the remarkably high critical temperature ($T_C \simeq 39\ K$) simple crystal structure, relatively long coherence lengths [179] ($\xi^c \simeq 25$Å, $\xi^{ab} \simeq 65$Å) and low surface resistance [105] ($R_S \simeq 0.8 m\Omega$ at T=24 K). From the structural point of view, the intermetallic MgB_2 superconductor is very similar to graphite with crystal lattice formed by honeycomb layers of B atoms intercalated by layers of Mg atoms, sitting at the center of each underlying hexagon (see Fig. 4.1 for a picture of the cristalline structure of the MgB_2). From the theoretical point of view, this compound presents a rare example of two disconnected parts of the Fermi surface: a two-dimensional (2D) hole-type σ bands, and a three-dimensional (3D) electron-type π bands [99, 156]. The unusual consequence of this band structure makes that in the clean limit [107] two different energy gaps are formed at the Fermi level, both closing at the same temperature T_C. Indeed, two superconducting energy gaps have been experimentally observed by different techniques, including tunneling spectroscopy [69, 85, 114, 165, 32, 71, 148, 42, 9] specific heat measurements

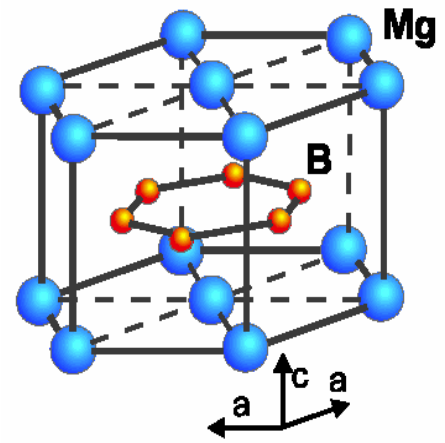

FIGURE 4.1. Structure of the MgB_2 compound.

[174, 29], Raman spectroscopy [45, 137], and high-resolution photoemission [166]. The majority of these studies agree with the presence of a larger gap around Δ_σ=7.0÷7.5 meV attributed to the 2D σ-band and a smaller gap Δ_π=2.0÷2.8 meV due to the 3D π-band. In the dirty limit a large amount of impurity scattering causes the two gaps to merge to an intermediate value $\Delta_D \simeq 4.1$ meV, that closes at a reduced T_C [31, 27].

The physics of multiband superconductors has been intensively studied since the appearance of the original theoretical works [162, 107, 31] and different phenomena are expected due to the presence of different condensates in the same material. The predictions have been tested in few cases, as e.g. in Niobium doped $SrTiO_3$ [65] or in Nickel borocarbides [40]. Due to these considerations, MgB_2 appeared, from the beginning, as a natural candidate to investigate peculiarities of a two band superconductor. Recently, a multiband model for quasiparticle and Josephson tunneling in MgB_2 based junctions has been developed [31]. Depending on the different bands exposed at the sides of the insulating barrier, different temperature behaviors of the Josephson current have been predicted with values of the $I_C R_N$ product at low temperatures as high as 9.9 mV and 5.9 mV for tunneling along the a-b planes and c direction, respectively. In the experiments, however, effective Josephson coupling of the 2D band σ with a 3D band, both of a MgB_2 or of a conventional superconducting counterelectrode, has been not observed. In addition to this, the measured $I_C R_N$ values are often severely depressed and regardless to the junction orientation, different temperature dependencies of the Josephson current are often reported [71, 42, 144, 167, 155, 172]. Similar behavior is expected in proximity coupled S/I/N/S structures [15], and in MgB_2 junctions it has been

attributed to degradation of T_C at the interface and/or to the barrier nature and quality.

In this section, based on Refs. [S2,S8], we address the problem of the behavior of both SGS and Josephson current in the multiband superconductor MgB_2. Since both phenomena depend on the multiplicity of the order parameter in the two electrodes, the simultaneous presence of SGS and Josephson effect allows a consistent cross check to verify the effective coupling of different condensates at the sides of the tunnel barrier. To investigate this aspect more deeply, we have realized point contact junctions between MgB_2 pellets and Nb tips. The aim of our study was to check for the Josephson coupling of the Nb order parameter with both the 2D and/or 3D MgB_2 bands, this aspect reinforced by the appearance of the related subharmonic gap resonances. In the following we report the first detailed study of the temperature dependence of both subharmonic gap structures and Josephson current observed in asymmetric Nb-MgB_2 micro-constrictions. Current-Voltage characteristic ($IvsV$) and conductance spectra ($dI/dVvsV$) were measured by using a home built point-contact apparatus, in which a Nb tip was pressed into high quality MgB_2 pellets, to favor the possible interaction with both bands of this compound.

4.1.1. Conductance characteristics for $T > T_C^{Nb}$

The polycrystalline MgB_2 pellets used in the present work, showed resistive superconducting transitions at $T_C(\rho = 0) = 38.8$ K, with $\Delta T_C \simeq 0.5$ K. The sample surface was chemically etched in a 1% HCl solution in pure ethanol. The Nb tips were prepared by cutting a thin (0.2 mm) Nb wire then treated by electrochemical etching.

In Fig. 4.2(b),(c) we show the conductance spectra measured for high and low junction resistances above the niobium critical temperature, T_C^{Nb}. These are representative of several measurements carried out on different contacts. High contact resistances were obtained by pushing the Nb tip into the MgB_2 and then slightly releasing the pressure. In this case, the conductance curves show the typical tunneling behavior, Fig. 4.2(b). The temperature dependence of the zero bias tunneling conductance, reported in the inset, suggests that rather than a S/I/N junction, the contact is formed between two MgB_2 grains. Indeed, a zero bias conductance peak is found as for S/I/S junctions, due to thermally activated quasiparticles with spectral weight increasing for rising temperatures. The S/I/S behavior has been observed in other experiments of PCAR spectroscopy in polycrystalline high-T_C superconductors [114, 116] and it has been attributed to a small piece of the base electrode captured by the tip apex. Due to the granularity of the samples, also in our case when releasing the pressure, one MgB_2 grain remains on the Nb tip, see Fig. 4.2(a). Two junctions in series are so formed and in the analysis of the data

attention has to be payed to the relative weight of the related junction resistances. In the tunneling regime, the contribution of the point contact junction is not critical, since $R_{PC} << R_J$. On the other hand, this has to be taken into account, in the point contact regime, with both resistances of the same order of magnitude. The tunneling conductance characteristic, measured at T=12 K (scattered graph in Fig. 4.2(b)), were so compared to the theoretical fitting for a S/I/S tunnel junction between two identical superconductors (solid line). Since $R_N = 3.1\ k\Omega$, we did not consider the contribution of the point contact in series. $\Delta_\pi = 2.7\, meV$ was used in the fitting in which a broadening parameter, representative of the quasiparticle finite lifetime, $\Gamma = 0.7$ meV was also included [59].

The conductance spectrum of a low resistance contact is shown in Fig. 4.2(c), where the expected Andreev Reflection behavior with conductance enhancement for $eV < \Delta$ is observed. The conductance characteristic also shows dip structures at energies higher than the Andreev Reflection feature (arrows in the figure), that are not reproduced by the usual BTK theory (for details see Sec. 2.2). The origin of these dips has been related to proximity effect [160] and/or to the formation of a junction in series [151]. In our case, for a satisfactory fitting of the experimental data, it was necessary to consider a more complex configuration, consistent with the assumption shown in Fig. 4.2(a). Indeed, when the resistance of the point contact junction (R_{PC}) is comparable with the resistance of the Josephson junction (R_J), we have to consider the formation of two junctions in series: the S/N point contact between the Nb-tip and MgB_2 and the inter-grain, low resistance MgB_2/MgB_2 junction. As shown in Fig. 4.2 (a), as the point contact tip/grain junction is approached to the base MgB_2 electrode, the latter junction reduces its resistance and the two MgB_2 grains can be coupled by Josephson effect. The measured voltage is now given by the sum of two contributions, i.e., the voltage drop V_{PC} at the point contact and V_J at the Josephson junction. In the limit of small capacitance C, the average contribution V_J can be simulated by the modified resistively shunted junction model given by Lee[104], where:

$$\langle V_J \rangle = \frac{2}{\gamma} R_J I_J \frac{exp(\pi\gamma\alpha) - 1}{exp(\pi\gamma\alpha)} T_2^{-1} \tag{4.1}$$

with $\alpha = I/I_J$ the normalized current, I_J the Josephson current of the junction in series, $\gamma = hI_J/eK_BT_n$ (T_n being the effective noise temperature) and

$$T_2 = \int_0^{2\pi} d\varphi \sin\frac{\varphi}{2} I_1\left(\gamma \sin\frac{\varphi}{2}\right) exp\left[-\left(\frac{\gamma}{2}\alpha\right)\varphi\right]$$

where $I_1(x)$ is the modified Bessel function. The conductance $\sigma(V)$ is then calculated by the formula:

$$\sigma(V) = dI/dV = (dV_{PC}/dI + dV_J/dI)^{-1}, \tag{4.2}$$

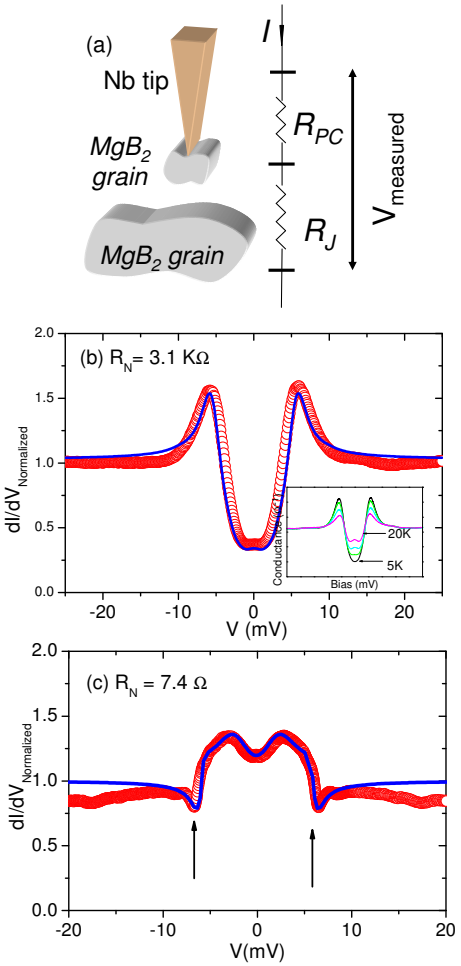

FIGURE 4.2. (a) A small MgB_2 grain remains on the Nb tip realizing two junctions in series: the point contact between the Nb tip and the small grain with resistance R_{PC}, and the Josephson junction between the two MgB_2 grains with resistance R_J. The measured voltage, V_{meas}, is the sum of the voltage drops at both junctions. (b) Tunneling conductance for a high resistance contact measured at T =12K. Experimental data (scattered graph) are compared to the theoretical simulation (solid line) for a S/I/S tunnel junction between two MgB_2 with Δ_π= 2.7 meV and Γ = 0.7 meV . (c) Conductance spectrum at T =12 K for a low resistance contact. The theoretical simulation (solid line) has been obtained with Δ_π= 2.4 meV, Z=0.66 and Γ = 0 meV considering the formation of an intergrain MgB_2/MgB_2 junction in series with $R_J = 1.5\Omega$ and $I_J = 1.2$ mA.

where the point contact contribution is simulated by the usual BTK model (Eq. 2.16). The best theoretical fitting (solid line in Fig. 4.2(c)) reproducing also the side deeps, was obtained for $\Delta_\pi = 2.4$ meV and Z =0.66, and no smearing factor Γ was needed for this junction.

We notice that the presence of the Josephson junction in series introduces in the model two more fitting parameters, the resistance $R_J = 1.5\Omega$ and the critical current I_J= 1.2 mA of the Josephson junction; these, however, are not independent one from the other and from the measured resistance. We remark here that, since the measured voltage $V_{\rm meas} = V_{\rm PC} + V_J > V_{\rm PC}$, a theoretical fitting that did not take into account the presence of the additional V_J, would give an over-estimation of the MgB_2 superconducting energy gap. From our discussion, it appears that PC spectroscopy reveals two type of junctions depending on the contact resistance: MgB_2/MgB_2 at high resistances when the tip/grain is left far from the surface and MgB_2/Nb at low resistances when the tip/grain is pushed into the surface. From the whole set of data at $T > T_C^{Nb}$, obtained in several locations, we have found as average value of the 3D gap, $\Delta_\pi = 2.5 \pm 0.2$ meV.

4.1.2. Conductance characteristics for $T < T_C^{Nb}$

As we already mentioned, the analysis of the Josephson coupling between a two band superconductor and a conventional one has been relatively less studied in the literature with contradictory results about both the values of the $I_C R_N$ product and its temperature dependence. In comparison with the theoretical predictions [31], the majority of the reports indicate depressed values of such product and different temperature behaviors irrespectively to the weak link or tunnel nature of the junctions [71, 42, 144, 155, 172]. To the best of our knowledge, in the majority of the cases coupling of the conventional superconductor with only the 3D band of the multi-gap material is inferred.

In this section we analyze the conductance data of low resistance junctions for $T < T_C^{Nb}$ in which both Josephson effect and subharmonic gap structures appear. Indeed, the simultaneous presence of these features makes unambiguous any conclusion about the coupling between the Nb order parameter and the 2D or 3D band of MgB_2. In addition to this, the study of the behavior of the subgap features in asymmetric junctions is itself of interest, since few reports can be found in the literature.

In Fig. 4.3 (a), (b) we show the conductance spectra measured at T=7K for two different contacts. The spectra are characterized by the huge conductance peak at zero bias, signature of the Josephson current flowing through the electrodes, as confirmed by the corresponding $I-V$ characteristics shown in the insets. In addition to this, subharmonic gap structures at low energies appear in both cases. Similar structures have been seldom observed in MgB_2

junctions, however a detailed analysis of their origin and/or temperature dependence was not carried out [114, 134].

In Fig. 4.3 we identify three principal features for junction (a), localized at energies $E_1 \simeq \pm 1.2$ meV, $E_2 \simeq \pm 2.4$ meV, and $E_3 \simeq \pm 3.5$ meV, while only E_1 and E_3 are visible in junction (b), at the same energies. As discussed in Subsec.2.2.2, these structures can be explained in terms of multiple Andreev Reflections that enhance conductance at voltages Δ_1/n, Δ_2/n, and $(\Delta_1+\Delta_2)$. The most useful way to identify the origin of various SGS can be obtained

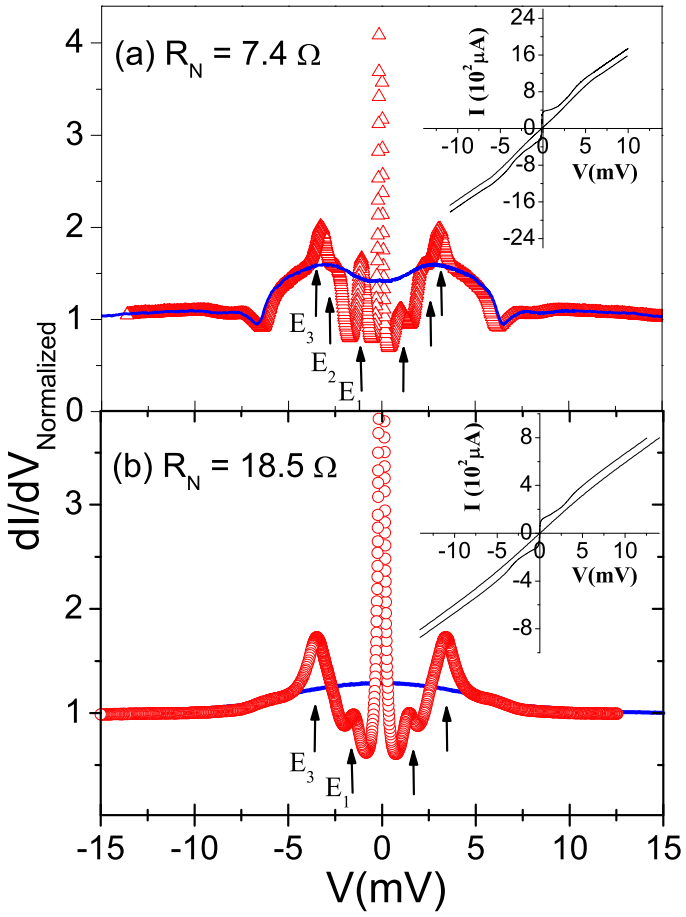

FIGURE 4.3. Conductance spectra for two different contacts measured at T = 7 K (scattered graphs). The conductance measured at T = 12 K, i.e., above T_C^{Nb}, are also reported (solid lines). The arrows indicate the energies of the SGS. Insets: Current-Voltage characteristics of the same junctions.

by studying their temperature dependence. Due to the high stability of our system, the dynamical conductance of both the contacts were measured in the temperature range between 4.2K and 12K. Since the two superconductors have quite different critical temperatures ($T_C^{MgB_2} \simeq$ 39K; $T_C^{Nb} \simeq$ 9.2 K) for these temperatures, only changes in the Nb energy gap are expected to affect the evolution of the SGS.

In Fig. 4.4 (a) we show the temperature dependence of the conductance spectra for the junction of Fig. 4.3(a). We clearly see that the feature at the highest energy (E_3) changes in temperature while $E_2 \simeq \pm 2.4$ mV and $E_1 \simeq \pm 1.2$ mV remain quite stable, suggesting that these are related to MgB_2. In Fig. 4.4 (b), we report the temperature dependence of the energy positions of the SGS for both junctions of Fig. 4.3, with solid and empty symbols referring to junction (a) and (b), respectively. Due to the fact that all the

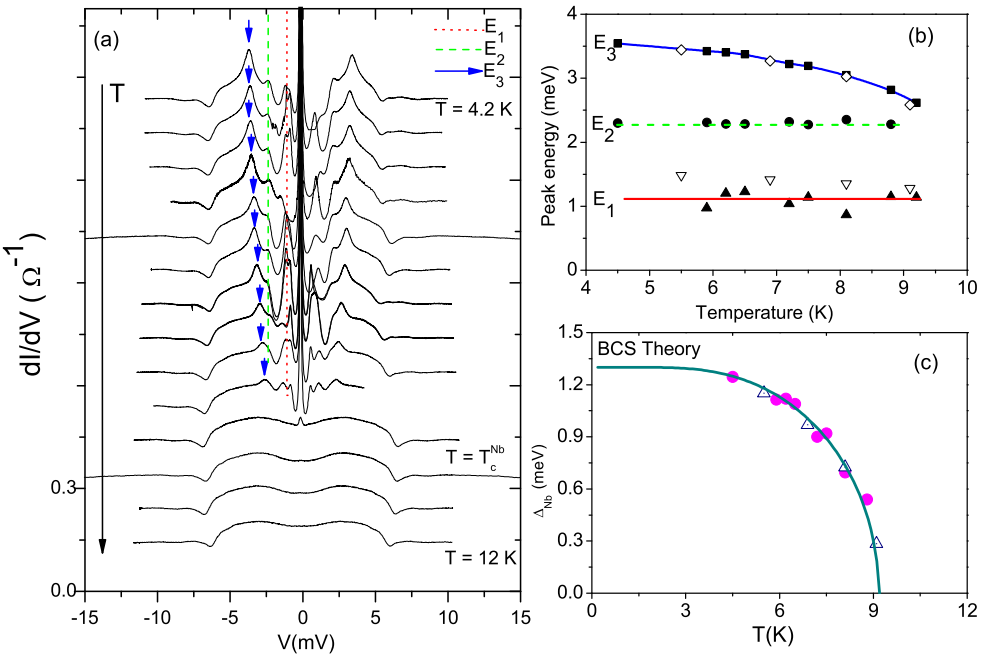

FIGURE 4.4. (a) Temperature dependence of the conductance spectra of the junction in Fig. 4.3 (a) in the range between 4.2K and 12K. All the spectra have been shifted and the scale is valid only for the highest temperature data. The arrows indicate the energy positions of the E_3 feature. (b) Temperature dependence of E_1, E_2, E_3. Dotted and solid lines are guidelines for the eye. Open symbols correspond to sample in Fig. 4.3 (b). (c) Temperature dependence of $\Delta^{Nb}(T) = E_3(T) - E_2(T)$, symbols, and theoretical curve, full line.

structures appear for voltages lower than 3.0 mV, we exclude the influence of the 2D σ band in the formation of the resonances. We then make the following identification: $E_3 \rightarrow \Delta_\pi^{MgB_2} + \Delta^{Nb}$, $E_2 \rightarrow \Delta_\pi^{MgB_2}$, and $E_1 \rightarrow \Delta_\pi^{MgB_2}/2$, consistently with the MgB_2 value of $\Delta_\pi = 2.4$ meV inferred from the theoretical fitting of the data at $T > T_C^{Nb}$ (Fig. 4.3 (c)). To confirm our hypothesis, we have extracted the temperature dependence of the Nb gap from the data $E_3(T)$ and $E_2(T)$, being $\Delta^{Nb}(T) = E_3(T) - E_2(T)$. The result is plotted in Fig. 4.4 (c) where the experimental data correctly follow the theoretical behavior (full line) expected for the Nb energy gap. In particular, the theoretical fitting gives $\Delta^{Nb}(T = 0) = 1.4$meV and a local critical temperature $T_C^{Nb} = 9.2$K. We notice that the E_2 structure only appears in the lower resistance junction (Fig. 4.3(a)), and its amplitude is relatively depressed in comparison with E_1 and E_3. Indeed, for this contact, we measured a higher value of the Josephson current which, in comparison with junction (b), implies a stronger coupling between the two electrodes.

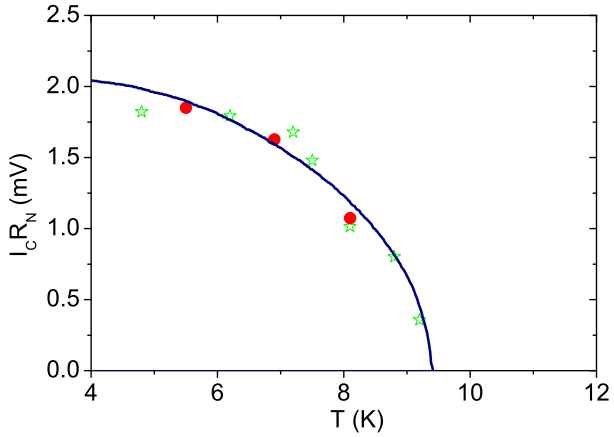

FIGURE 4.5. Temperature dependence of the $I_C R_N$ product. The experimental data (scattered graph) are compared to the Ambegaokar-Baratoff behavior (full line).

In Fig. 4.5, we finally report the $I_C R_N$ product versus temperature for both contacts in Fig. 4.3 (a) and (b). $I_C = 290\,\mu A$ and $I_C = 110\mu A$ were measured in these junctions with $R_N = 7.4\Omega$ and $R_N = 18.5\Omega$, respectively. This implies $I_C R_N = (2.1 \pm 0.1)$ mV at T=4.5K, among the highest values reported in the literature [42, 71, 167]. Our values are very close to those predicted when the superconducting Nb couples with the MgB_2 π-band [31] and follow the expected Ambegaokar-Baratoff temperature behavior [31, 15]. From our discussion it unambiguously appears that coupling of the Nb energy gap only occurs with the MgB_2 3D Δ_π band, while in more than 50 measured

contacts we never found evidence for coupling with the 2D Δ_σ band. We have also demonstrated that it is in principle possible to avoid the MgB_2 degraded surface layer, responsible for both depressed values of the $I_C R_N$ product and non conventional temperature behavior.

4.1.3. Summary of the results

We have realized superconducting micro-constrictions between high quality MgB_2 pellets and electrochemically etched Nb tips. The conductance as a function of bias measured above the Nb critical temperature reveals that an inter-grain MgB_2/MgB_2 junction is often formed in series with the MgB_2/Nb contact. This results from a small piece of MgB_2 remaining on the tip apex when relieved from the pellet. Depending on the tip pressure the MgB_2/MgB_2 contact resistance can be either larger (tip far from the pellet) or comparable (tip into the pellet) with the MgB_2/Nb point contact resistance. In the last case, an accurate theoretical analysis has to be carried out to extract the correct value of the MgB_2 superconducting energy gap. For $T < T_C^{Nb}$, we have observed Josephson effect as well as subgap resonances. We explain these features in terms of Subharmonic Gap Structures due to Multiple Andreev Reflections. From the analysis of the SGS, consistently with the values measured for $T > T_C^{Nb}$, we have extracted the correct temperature dependence of the Nb energy gap and the value $\Delta_\pi \simeq 2.4$meV for the 3D energy gap at the MgB_2 Fermi surface. In our junctions, at T=4.5K, we have measured $I_C R_N$ values up to 2.2meV, among the highest reported in literature. The temperature dependence of the $I_C R_N$ product follows the classical Ambegaokar-Baratoff behavior. Both observations completely confirm the results predicted by a recent theoretical model [31]. In addition to this, the simultaneous observation of both Josephson current and SGS, unambiguously indicate the coupling of the Nb energy gap with the MgB_2 3D band.

4.2. Andreev reflections in an intrinsic F/S system: $RuSr_2GdCu_2O_8$

In this section we report PCAR studies carried out in the hybrid ruthenocuprate $RuSr_2GdCu_2O_8$ (Ru-1212) system (results reported in Refs. [S1,S3,S4]). This compound [16] has recently drawn great attention among theorists and experimentalists in the field of solid state physics due to the coexistence at low temperatures of superconducting and magnetic ordering [118]. The Ru-1212 structure is similar to that of $YBa_2Cu_3O_7$ with magnetic (*2D*) RuO_2 planes substituting the (*1D*) Cu-O chains (see Fig. 4.6 (a)). The superconducting critical temperature in this compound strongly depends on the preparation conditions with some reports showing transition onset as high as 50K [23].

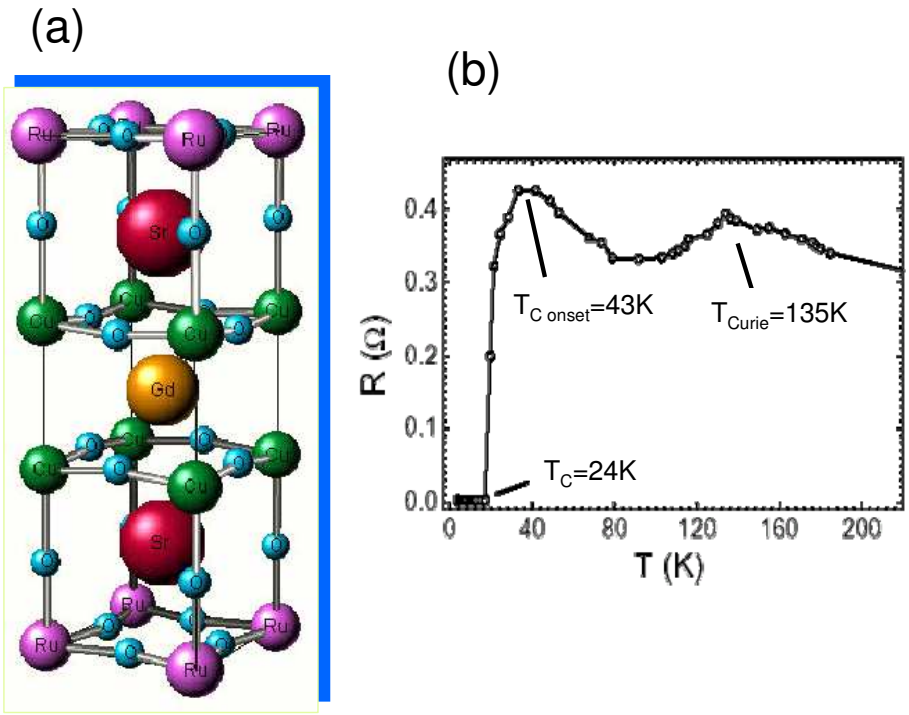

FIGURE 4.6. (a) Cristalline structure of the Ru-1212; (b) Resistance *vs* temperature of the sample reported in this work, showing the critical and the Curie temperatures.

The Ru-1212 also shows a magnetic phase below 135K. It has been reported that the magnetic order of the Ru moments is predominantly antiferromagnetic along the *c* axis [112], while a ferromagnetic component has been observed in the RuO_2 planes, that act as charge reservoir [24]. At the moment, due to complexity of this compound, an exhaustive description of the interaction between the magnetic and superconducting layers is still missing as well as an unambiguous evaluation of the symmetry of the energy gap.

4.2.1. Experimental conductance curves and theoretical fittings

The Ru-1212 samples used for this study were directionally solidified pellets, grown by means of the Top-Seeded Melt-Textured method starting from Ru-1212 and Ru-1210 ($RuSr_2GdO_6$) powder mixtures with a ratio Ru-1212/Ru-1210 = 0.2. The details of the preparation procedure are reported elsewhere [8]. In the X-Ray diffraction patterns, a single Ru-1212 phase was found. In the resistivity measurements versus temperature, the onset of the superconducting transition was observed at $T_C^{on} \simeq 43K$ with $T_C \simeq 24K$ and

ΔT_C = 12K (ΔT_C is defined as the difference between the temperatures measured at 90% and 10% of the normal state resistance). We notice that a broadening of the superconducting transition is often observed in polycrystalline samples and it is usually related to the formation of intergrain weak Josephson junctions[136, 118, 46]. We address this point in the next section.

To realize our experiments we used a Pt-Ir tip, chemically etched in a 40% solution of HCl, while Ru-1212 samples were cleaned in an ultrasound bath in ethyl alcohol. Sample and tip were introduced in the PCAR probe. The point contact junctions were formed by pushing the Pt-Ir tip on the Ru-1212 pellet surface with the probe thermalized in the liquid He^4 bath.

In Fig. 4.7, we show a variety of normalized conductance spectra obtained at T= 4.2K by establishing different contacts on different areas of the same Ru-1212 pellet. The junction resistances varied between 10Ω and 100Ω. By using the Sharvin relation, [153] it has been possible to achive an estimation of the size of the contact area. Indeed $R = \rho l/4a^2$, where $\rho = 0.4 m\Omega\ cm$ is the low temperatures resistivity and l≈ 1000 Å, as estimated in Ref.[8]. In our case, we have found that the typical contact size varied between 300Å and 1000Å.

We observe that all the reported spectra are characterized by a Zero Bias Conductance Peak (ZBCP) with a triangular structure, the main features appearing for each contact with different shapes, amplitudes and energy widths. Quite often, oscillations are observed on the conductance background, as shown in Figs. 4.7 c–f. We observe that the ZBCP appears as a simple structure in Fig. 4.7b, while in the remaining spectra it results to be structured with variations of slope or secondary maxima, as in Fig. 4.7e. The maximum conductance ratio $G_{NS}(V = 0)/G_{NN}(V >> \Delta)$ is less than 2 for all the curves, however $G_{NS}(V = 0)/G_{NN}(V >> \Delta) \simeq 2.2$ for the data in Fig. 4.7f. In addition to this, the energy width of the main zero bias triangular structure is lower than 10mV in Figs. 4.7a–d while it results wider, around 40mV, in Figs. 4.7e,f. At a first qualitative analysis, these data appear quite puzzling and could be interpreted in term of local, large variations of the superconducting energy gap. In the following, we will show that the theoretical fittings of all the spectra give clear indication of a *d-wave* symmetry of the superconducting order parameter, with consistent values of the inferred amplitude of the energy gap.

First of all, let us quantitatively analyze the curves of Figs. 4.7a–d. We were not able to reproduce the conductance spectra reported in Fig. 4.7 a,b by using either the conventional *s-wave* model or the anisotropic one, even by considering small Z values, indicative of low barriers. On the other hand, as can be observed in Fig. 2.9 a–c, the *s-wave* fittings cannot model the structured conductances reported in Figs. 4.7 c,d. The solid lines in the figures

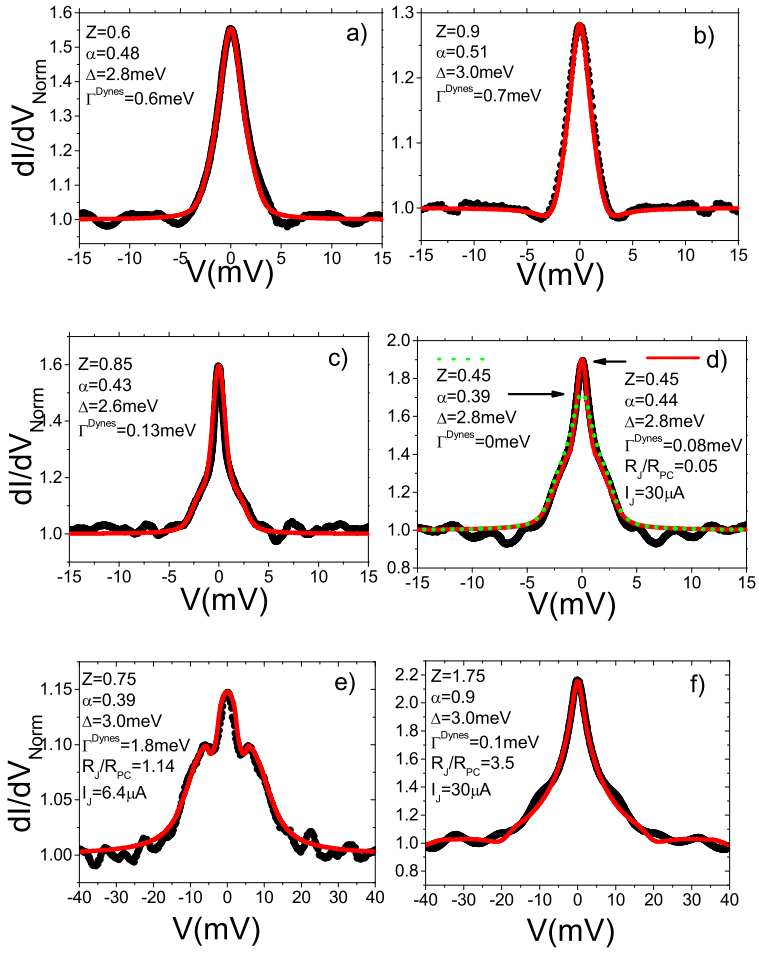

FIGURE 4.7. The dI/dV vs V characteristics measured in different Ru-1212/Pt-Ir PC junctions at 4.2K. The experimental data (dots) are shown together with the best theoretical fittings (solid lines) obtained by a modified BTK model for a *d-wave* symmetry of the superconducting order parameter.

are the theoretical fittings obtained by considering a *d-wave* symmetry of the order parameter in the modified BTK model, Eqs. 2.17-2.21. A satisfactory agreement is obtained by using as fitting parameters the superconducting energy gap Δ, the barrier strength Z, the angle α and a phenomenological factor Γ^{Dynes} [59] to take into account pair breaking effects and finite quasiparticle lifetime [73]. We notice that in the considered spectra, both quasiparticle tunneling and Andreev reflection processes take place, since intermediate Z values

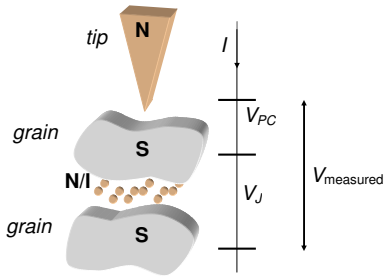

FIGURE 4.8. Intergrain coupling effect in polycrystalline samples. The measured voltage $V_{measured}$ is the sum of two terms: V_{PC}, the voltage drops between tip and sample, the N/S PC junction, and V_J, the voltage drops between two superconducting grains, forming the S/I/S Josephson junction.

have to be used to simulate the barrier strength ($0.45 \leq Z \leq 0.9$). Moreover, the angle α varies between 0.39 and 0.51, indicating that the average transport current mainly flows along an intermediate direction between the nodal one ($\alpha = \pi/4$) and that of the maximum amplitude of the energy gap ($\alpha = 0$). The modified *d-wave* BTK model allows to satisfactorily reproduce the variations of slope around $\pm 1mV$ of the structured ZBCP in Figs. 4.7a,c,d with a light discrepancy in modeling the full height of the peak in Fig. 4.7d. We show in the next section that a more satisfactory fitting for this contact can be obtained by taking into account an additional in series intergrain junction.

We remark that the values of the superconducting energy gap, inferred from the theoretical fittings, are all consistent and enable us to estimate an average value of the amplitude of the order parameter $\Delta = (2.8 \pm 0.2)$meV. This value is surprisingly low in comparison with the amplitude of the energy gap in other cuprate superconductors, however the possibility that the presence of the RuO_2 magnetic planes can play an important role in the complex Ru-1212 system has to be taken into account. We notice that the ratio between the smearing factor Γ^{Dynes} and the superconducting energy gap results always less than 20% and it vanishes for the fitting shown in Fig. 4.7d. We consider this fact as an indication of the good quality of our point-contact junctions.

4.2.2. Role of the intergrain coupling

To complete our discussion about the spectra measured at low temperatures, we now address the analysis of the conductance curves reported in Figs. 4.7e,f, with a wider ZBCP. In this respect, we observe that, due to the granularity of the compound, in same cases, an intergrain Josephson junction can be formed in series with the point contact one, as schematically drawn in Fig. 4.8. This

topic has been already addressed in the previous section about PCAR studies on MgB_2.

To provide a quantitative evaluation of the conductance spectra, we consider a real configuration in which the Pt-Ir tip realizes a PC junction on a single Ru-1212 grain, which, in turn, is weakly coupled to another grain, so forming a Josephson junction. In this case the measured voltage corresponds to the sum of two terms:

$$V_{\mathrm{measured}}(I) = V_{PC}(I) + V_J(I)\ , \tag{4.3}$$

where V_{PC} and V_J are the voltage drops at the N/S point contact junction and at the S/I/S intergrain Josephson junction, respectively. This last contribution can be calculated by the Lee formula [105] which, in the limit of small capacitance and at low temperatures, reduces to the simplified expression [173]:

$$V_J = \begin{cases} 0 & \text{for } I < I_J\ ; \\ R_J I_J \sqrt{[(I/I_J)^2 - 1]} & \text{for } I \geq I_J\ . \end{cases} \tag{4.4}$$

At the same time, for the point contact contribution, we use again the extended BTK model for a *d-wave* superconductor. The $I(V)$ characteristic is then calculated by inverting Eq. 4.3 and the conductance spectrum is given by:

$$\sigma(V) = \frac{dI}{dV} = \left(\frac{dV_{PC}}{dI} + \frac{dV_J}{dI} \right)^{-1}\ . \tag{4.5}$$

By applying this simple model we have satisfactory fitted the experimental data reported in Figs. 4.7e,f. Remarkably, for both spectra, the best fittings have been obtained by using $\Delta = 3.0$ meV, consistently with the average value extracted from the other curves in Figs. 4.7a–d. We observe that, in this model, two more parameters are needed, namely the resistance R_J and the critical current I_J of the Josephson junction. However, the choice of these two parameters is not completely arbitrary, since the condition $R_J + R_{PC} = R_{NN}$ has to be fulfilled, where R_{NN} is the measured normal resistance and the product $R_J I_J$ necessarily results lower than Δ [15].

In some cases, it has been pointed out that dips in the conductance spectra can be related to the presence of intergrain junctions, and for sake of completeness, we have applied our model also to the spectra of Figs. 4.7 a–d. We notice that for different junctions, the effect of the intergrain coupling results more or less evident, depending on ratio R_J/R_{PC}. For the conductances shown in Figs. 4.7a–c this effect turns out to be negligible, however, some improvement of the theoretical fitting is obtained in the case of Fig. 4.7d (see dashed line). Remarkably, by this last fitting we have found the same value of the superconducting energy gap previously inferred, $\Delta = 2.8$meV, with a $\Gamma^{\mathrm{Dynes}}/\Delta$ ratio less than 3% and $R_J/R_{PC} = 0.05$.

4.2.3. Temperature dependence of the conductance spectra

To achieve information on the temperature dependence of the superconducting energy gap in the Ru-1212 system, in this section we analyze the temperature behavior of the conductance spectrum shown in Fig. 4.7d. Indeed, this PCAR junction resulted to be very stable for temperature variations.

In Fig. 4.9 we show the conductance characteristics measured in the temperature range 4.2K$\leq$T$<$ 35K. We firstly notice that the ZBCP decreases for increasing temperature and disappears at about T$\simeq$ 30K, that we estimate as the local critical temperature T_C^l of the superconducting Ru-1212 grain in contact with the Pt-Ir tip, consistently with the resistivity measurements[8]. This fact provides further evidence that the ZBCP is a consequence of the superconducting nature of Ru-1212 and is not due to spurious effects like inelastic tunneling via localized magnetic moments in the barrier region [49]. The experimental data for each temperature are then compared to the theoretical fittings calculated by using the *d-wave* modified BTK model with a small contribution of Josephson junction in series. For all the curves, we fixed the strength of the barrier and the angle α to the values obtained at the lowest temperature.

The resulting temperature dependence of the superconducting energy gap $\Delta(T)$ is reported in Fig. 1.3, where vertical bars indicate the errors in the gap amplitude evaluation, that increase when approaching the critical temperature. Contrarily to what expected for BCS superconductors, we observe that the energy gap, at low temperatures, decreases rapidly for increasing temperatures and goes to zero at T_C^l in a sublinear way. We notice that the same temperature evolution for the superconducting energy gap is found trough the *d-wave* BTK model with or without considering any intergrain junction in series; remarkably, in this last case, the superconducting energy gap Δ remains the only varying parameter. A similar temperature dependence has been reported by G. A. Ummarino et al. [71], however these authors give a larger estimation of the maximum gap amplitude.

From the average value of the superconducting energy gap Δ = 2.8meV and from the measured local critical temperature $T_C^l \simeq$ 30K, we obtain a ratio $2\Delta/K_BT_C^l \simeq 2$ much smaller than the predicted BCS value and also smaller than the values found for high-T_C cuprate superconductors[50]. Again we speculate that the simultaneous presence of superconducting and magnetic order is an important key for understanding the behavior of the Ru-1212 system. Coexistence of superconductivity and antiferromagnetism is found among cuprates, however it is common believe that ferromagnetism and superconductivity are mutually excluding orders. Recently, it has been found that in conventional Ferromagnetic/Superconducting (F/S) structures, proximity effect give rise to an oscillatory behavior of the superconducting T_c as

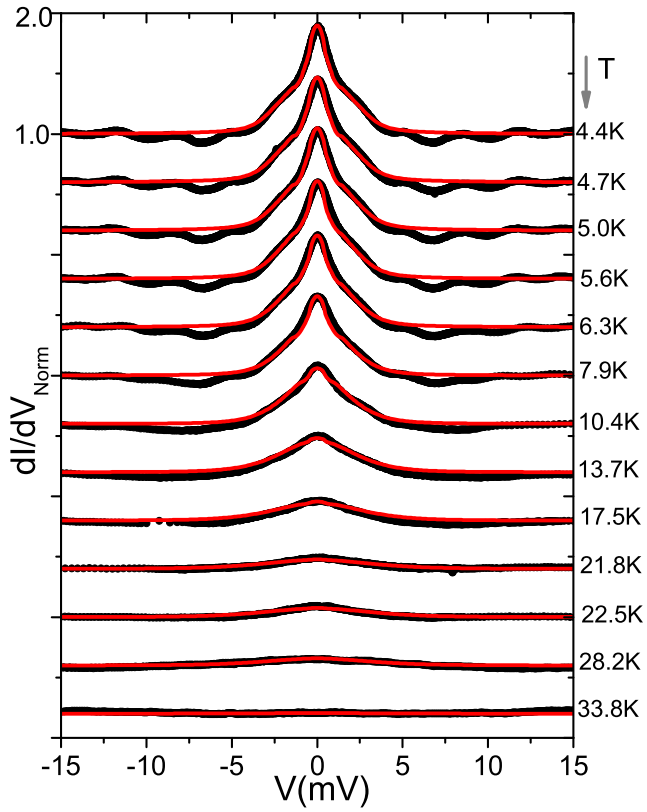

FIGURE 4.9. Temperature evolution of the conductance spectrum of Fig. 4.7 (c) from T = 4.2K to up the critical temperature (dots). The solid lines are the theoretical fittings obtained by a modified *d-wave* BTK model with the energy gap as only free parameter.

a function of the thickness of the F layer [38, 86]. There are conditions for which a change of sign of the order parameter occurs, producing the π-junction phenomenon[74]. In addition to this, a dramatic suppression of the amplitude of the order parameter is expected for high T_C superconductors in close contact with a ferromagnetic material [110] and various examples of anomalous temperature behavior are found in the literature. Gapless superconductivity can be achieved, that can induce a sublinear temperature dependence of the superconducting energy gap. In the Ru-1212 system, it has been proved that the RuO_2 planes are conducting, however these do not develop superconductivity at any temperature[135]. By means of different experimental techniques, it has been inferred that a large fraction of the charge carriers is not condensed

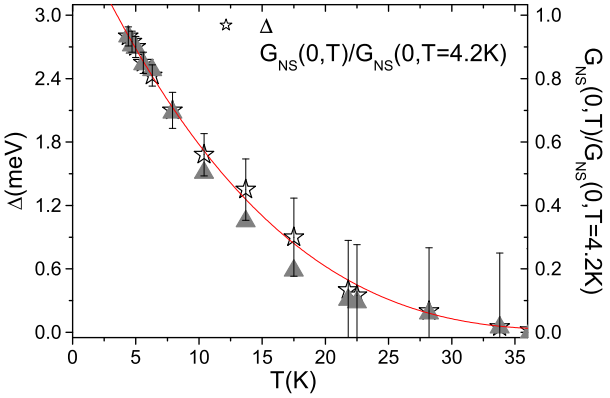

FIGURE 4.10. Temperature dependence of the superconducting energy gap as inferred from the theoretical fittings shown in Fig. 4.9. The solid line is a guide for the eyes. The right hand scale refers to the temperature evolution of the measured height of the ZBCP normalized to the 4.2K value.

in the superconducting state even at low temperatures [135]. Both findings are consistent with a reduced value of the $2\Delta/(K_B T_C)$ ratio in this compound.

In Fig. 1.3 we also report (righthand scale) the temperature evolution of the height of the ZBCP normalized to its value at T=4.2K. It is worth to notice that $G_{NS}(V = 0, T)$, as directly measured from the experiments, and $\Delta(T)$, as inferred from the theoretical fittings, show a similar scaling with temperature. This correspondence is easily verified for Z=0 in case of a *s-wave* superconductor, however it is a quite new result since it has been found for intermediate barriers and unconventional symmetry of the superconducting order parameter.

4.2.4. Magnetic field dependence of the conductance spectra

As we already observed, one of the most interesting features of the Ru-1212 is the coexistence of the superconducting phase and magnetic order. Indeed, from Nuclear Magnetic Resonance (NMR) [103, 169] and magnetization [34] measurements, it has been found that in this compound ruthenium occurs in a mixed valence state Ru^{4+}, Ru^{5+} with some higher Ru^{5+} concentration. The RuO_2 planes, from one side, act as charge reservoir for the superconducting CuO_2 planes, on the other hand, as observed in Muon Spin Rotation (μSR) experiments [24], they show quite homogeneous ferromagnetic order below T_C. A weak interaction between the two order parameters, ferromagnetism in the RuO_2 planes and superconductivity in the CuO_2 planes, has been suggested and recently several experiments appear to confirm this hypothesis [135]. Despite of the huge experimental and theoretical efforts focused on the study of

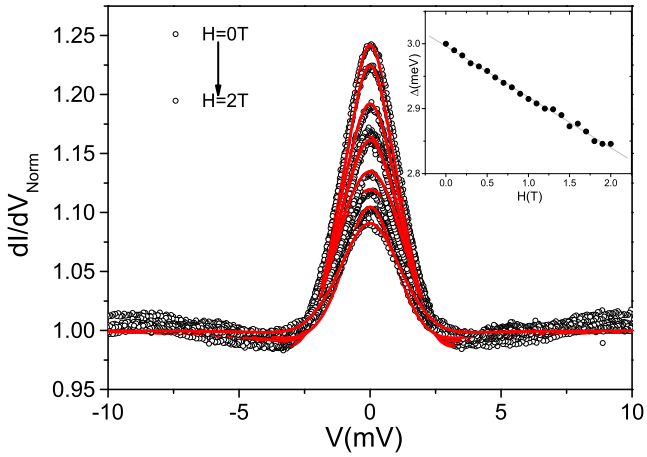

FIGURE 4.11. Magnetic field dependence of the normalized dI/dV vs V characteristics at T=4.2K from 0 T to 2 T (dots) for the spectra of Fig. 4.7b. The full lines are the theoretical fittings obtained as discuss in the text. In the inset the magnetic field dependence of the energy gap is reported.

the interplay between superconductivity and magnetism, to the best of our knowledge no spectroscopic studies in magnetic field of the superconducting order parameter in Ru-1212 have been reported in literature so far.

In Fig. 4.11 we show the PCAR spectra measured by applying an external magnetic field, parallel to the tip, with intensity H varying from 0T to 2T. The dI/dV vs V curves refer to the contact reported in Fig. 4.7b. A reduction of the ZBCP for increasing magnetic fields is observed, that in first approximation can be reproduced by a phenomenological approach. Indeed, addressing the problem of the magnetic field dependence of the conductance characteristics is non conventional superconductors, is a quite difficult task and a complete treatment of PCAR spectroscopy in magnetic field would require the use of an appropriate density of states in calculating the BTK expression for the reflection and transmission coefficients at the N/S interface. Due to the lack of an analytical model, Miyoshi et al. [117] presented a two fluid model to reproduce the effect of normal vortex cores in PCAR junctions in conventional superconductors, assuming that the contact area contains multiple randomly distributed individual junctions (non-Sharvin regime [153]). These authors propose a simplified expression for the conductance, written as a sum of normal and superconducting channels:

$$G_{NS_{tot}}(V) = (1-h)G_{NN} + hG_{NS}(V)$$

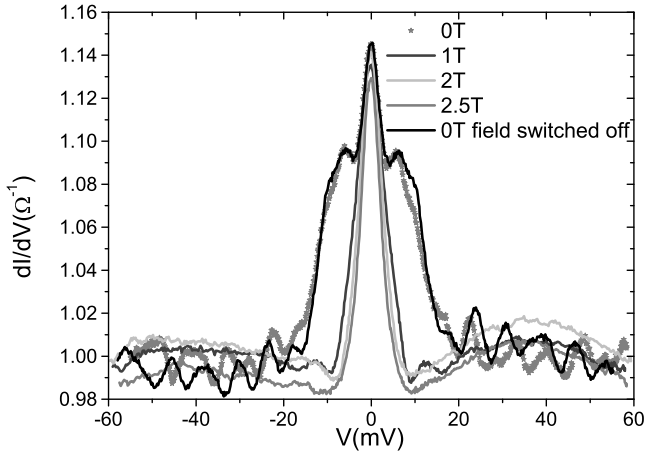

FIGURE 4.12. Normalized conductance curves for the contact of Fig. 4.7e measured at T=4.2K in magnetic field up to 2.5T. When the field is switched off, the original spectra are recovered.

where h=H/H_{C_2} and H_{C_2} is the critical field. This approach, however, cannot be applied to our experiments since we deal with polycrystalline, unconventional superconductor, exhibiting internal magnetic ordering. In this case, the magnetic induction B is not simply proportional to the external magnetic field H and as a consequence the density of vortices is not linearly related to H.

An alternative way to perform a theoretical fitting is obtained by using an additional pair breaking parameter to simulate the effect due to the magnetic field [121, 72]. In this case, the total broadening effect Γ is considered as the sum of two terms: $\Gamma = \Gamma^{Dynes} + \Gamma^{ext}$ where Γ^{Dynes} is the intrinsic broadening due to the quasiparticle lifetime, as used in the previous fittings, while Γ^{ext} mimics the pair breaking effect due to the external applied magnetic field. The curve at H=0T (see Fig. 4.7b) has been fitted by using the *d-wave* modified BTK model with $\Delta = 3.0$meV. For increasing magnetic fields we keep constant, in the numerical computation, the strength of the barrier Z=0.9, the orientation angle $\alpha = 0.51$ and the intrinsic $\Gamma^{\mathrm{Dynes}} = 0.7$meV, while varying only two parameters: the energy gap Δ and the magnetic field effect Γ^{ext}. We observe that the best theoretical fittings (solid lines in Fig. 4.11) satisfactorily reproduce for any field both the height and the amplitude of the measured spectra. In the inset, we report the magnetic field dependence of the superconducting energy gap (dots) as extracted from the theoretical fittings. The amplitude of the energy gap reduces linearly for H up to 2T and by a linear extrapolation of the data, we find that the energy gap disappears at about $H^{\mathrm{ext}} \simeq 30$ T, consistently with the estimated critical field reported in Ref.[8].

We have also studied the effect of the magnetic field on the conductance characteristics of the junctions showing wider ZBCP, that are formed by two junctions in series. In Fig. 4.12 we report the dI/dV vs V curves measured up to 2.5 T for the contacts of Fig. 4.7e. In this case, we observe that the conductance curves dramatically change with the application of the magnetic field. As discussed in the previous section, the Josephson current due to the intergrain coupling is immediately suppressed by the magnetic field, modifying the spectra towards the narrower, non-structured, triangular shape of the ZBCP. In addition to this, the oscillatory behavior of the background, due to the intergrain coupling disappears in magnetic field. Remarkably, for the junctions of both Figs. 4.11, 4.12 the peculiar features of the spectra together with the normal junction resistance, are recovered when the magnetic field is switched off, and no hysteresis is found for increasing/decreasing fields.

4.2.5. Conclusions

In this section we have explained the main results of the PCAR conductance spectra obtained in superconducting $RuSr_2GdCu_2O_8$ (Ru-1212) polycrystalline pellets. All the conductance curves at low temperatures show a Zero Bias Conductance Peak that decreases for increasing temperatures and disappears at the local critical temperature $T_C^l \simeq 30$K of the superconducting grain in contact with the Pt-Ir tip. The triangular shape of all the measured spectra has been modeled by using a modified BTK model for a *d-wave* symmetry of the superconducting order parameter. This finding suggests a closer similarity of the Ru-1212 system to the high-T_C cuprate superconductors rather than to the magnetic ruthenate Sr_2RuO_4 compound. However, the remarkably low values of the energy gap $\Delta = (2.8 \pm 0.2)$meV and of the ratio $2\Delta/K_BT_C \simeq 2$ indicate major differences between the Ru-1212 and the high-T_C cuprates. We speculate that the presence of ferromagnetic order within the superconducting phase results in an effective reduction of the energy gap. We have also demonstrated that, when dealing with granular samples, intergrain coupling effects can play a predominant role. In some cases, an intergrain Josephson junction in series with the point contact junction is formed. Taking into account this feature as well, all conductance spectra have been properly modeled by considering a *d-wave* symmetry of the order parameter, with consistent values of the amplitude of the energy gap.

By fixing all the fitting parameters to their values at the lowest measured temperature, and by varying Δ, the temperature dependence of the energy gap has been extracted from the conductance characteristics of a very stable junction. We have found that the energy gap exhibits a sub-linear dependence in temperature. The magnetic field behavior of the spectra has been also studied, showing a linear reduction of the energy gap for fields up to 2 T, from which a critical field $H_{C_2} \sim 30$ T is inferred. We have found that both

the superconducting features and the normal background in the conductance spectra do not show any hysteresis in magnetic field. These observations seem to suggest a weak coupling between the superconducting and magnetic order parameter.

Our analysis may be helpful for a deeper understanding of the mechanisms enabling high temperature superconductivity, and its interplay with magnetic order in unconventional superconductors like rutheno-cuprates.

4.3. Study of the Andreev reflections at the interface between ferromagnetic and superconducting oxides

In this section we analyze the effect of spin-polarized electrons on the tunneling current in a heterostructure constituted by a high-TC superconductor, $YBa_2Cu_3O_{7-x}$ (YBCO), and a Colossal magneto-resistance ferromagnetic oxide $La_{0.7}Ca_{0.3}MnO_3$ (LCMO), as reported in Refs. [S5,S7]. We observe the presence of both Andreev bound states in the YBCO layer, and spin polarization in the LCMO layer. The zero bias conductance peak, appearing in the conductance spectra due to Andreev bound states at the Fermi level of the superconductor, results to be depressed by a proximity effect induced by the magnetic layer. Our results are well interpreted in the framework of the spin-polarized transport theory.

4.3.1. A rapid overview to YBCO and LCMO

In this subsection we explain the main properties of YBCO and LCMO.

4.3.1.1. YBCO. — A schematic structure of YBCO is presented in Fig. 4.13: the unit cell is developed from that of a tetragonal perovskite tripled along the c-axis and it consists of a sequence of copper-oxygen layers. The dimensions of the unit cell are approximately 1.2 nm and 0.4 nm in the c and in a or b-axis directions respectively. The compound $YBa_2Cu_3O_6$ is an insulator, so it has to be doped to gradually become a hole-doped metallic conductor and a superconductor below some critical temperature. The doping is achieved by adding additional oxygen which forms CuO chains. These oxygen ions attract electrons from the CuO_2-planes which therefore become metallic. Note, that the correct formula for YBCO material is $YBa_2Cu_3O_{7-x}$, where x corresponds to partial oxygen content. Measurements of resistance vs temperature on YBCO films show a $T_C \simeq 91$K [52].

4.3.1.2. LCMO. — The ideal structure of the LCMO oxide is a cubic perovskite. The large sized La trivalent ions and Ca divalent ions occupy the center of the cube with 12-fold oxygen coordination. The smaller Mn ions in the mixed-valence state Mn^{3+}–Mn^{4+} are located at the vertices of the cube and are coordinated 6-fold with the oxygen ions to form octahedrons MnO_6. In

Fig. 4.14 (a) a schematic view of the cubic perovskite structure is shown. Usually, the crystalline lattice will be distorted by the Jahn-Teller effect (see Fig. 4.14 (b)). The phase diagram of LCMO was measured by Cheong and Hwang [170], and is given in Fig. 4.14 (c). The undoped parent compound $LaMnO_3$ has an antiferromagnetic insulating ground state. $LaMnO_3$ and $CaMnO_3$ are both antiferromagnetic insulators. At first sight a mixture of $LaMnO_3$ and $CaMnO_3$ is expected to show no spectacular effect. But, in their phase diagram a ferromagnetism is found, metallicity and several regions with spin and charge orderings. An important aspect in the unexpected rich phase diagram is the small but relevant distinction in crystal structure, although both compounds are perovskites. $LaMnO_3$ consists of deformed MnO_6 octahedra, whereas the octahedra are perfect in $CaMnO_3$. The origin of the deformation is the crystal field splitting of the 3d orbitals. Above 10% Ca doping the ferromagnetic interactions suppress the antiferromagnetic coupling and a ferromagnetic ground state is obtained. In the region of 20% to 50% Ca substitution the ground state is a ferromagnetic metal, dominated by double exchange. According to Cheong's phase diagram, Fig. 4.14 (c), the ferromagnetic metallic phase emerges instantly above a critical concentration, at all

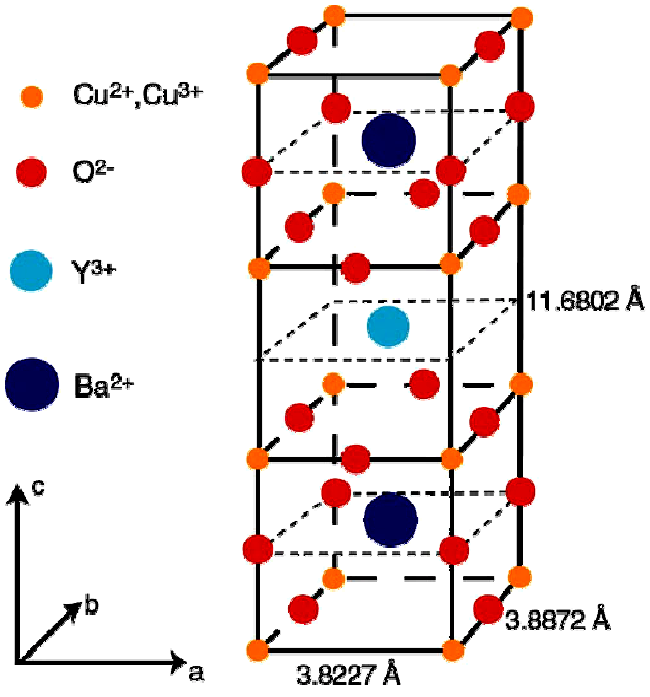

FIGURE 4.13. Schematic representation of the YBCO.

temperatures below T_{Curie}. Resistance *vs* temperature measurements without applied magnetic field showed that the metalinsulator transition temperature is in the range of 220-260K [53].

4.3.2. Sample preparation and experimental setup

Highly epitaxial, *c*-axis oriented (YBCO/LCMO) heterostructures were grown in a pure oxygen atmosphere (p=3.0 mBar) on $SrTiO_3$ (0 0 1) substrates (STO) by DC sputtering technique at T=900C (for further details see Refs. [52, 51]). A YBCO film of 500Å was first deposited; then, by defining the geometry through a shadow mask, we sequentially realized a YBCO/LCMO

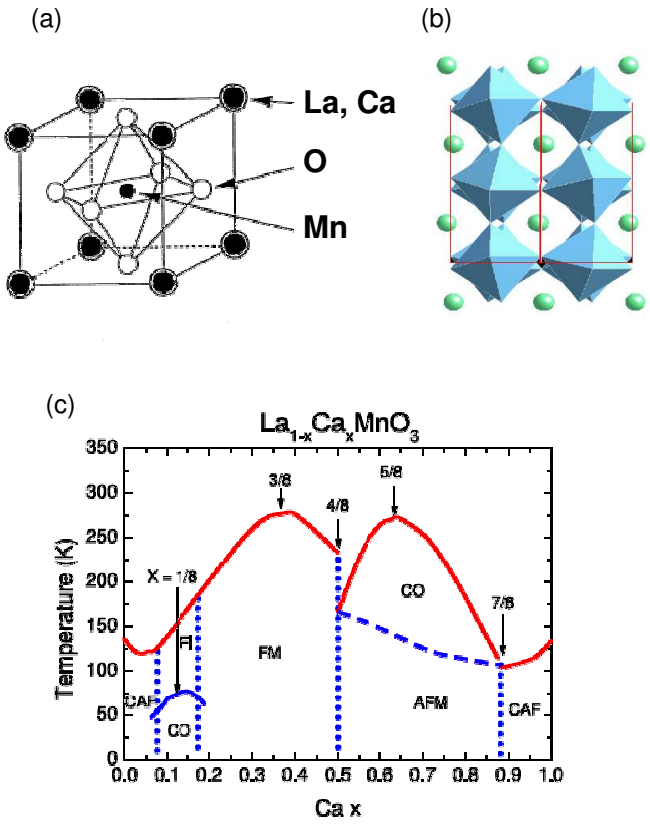

FIGURE 4.14. (a) Schematic view of the cubic cell of the LCMO. (b) Distortion of the structure due to the Jahn-Teller effect. (c) Phase diagram showing the different phases of LCMO as a function of Ca concentration. FM : Ferromagnetic Metal, FI: Ferromagnetic Insulator, AF: Antiferromagnetism, CAF: Canted Ferromagnetism, and CO: Charge/orbital Ordering

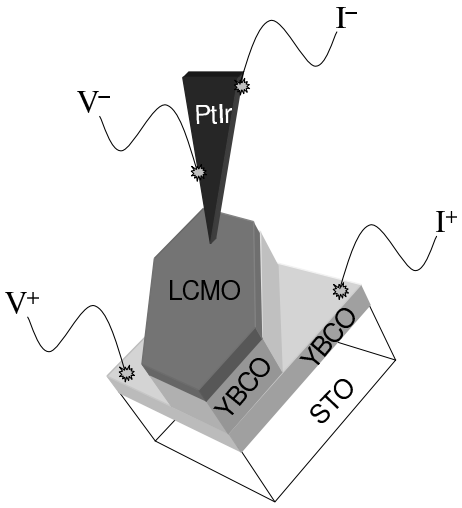

FIGURE 4.15. Scheme of our point contact junction realized between a Pt-Ir tip and a YBCO/LCMO bilayer.

bilayer with thicknesses $d_{\mathrm{YBCO}} = 1000$Å and $d_{\mathrm{LCMO}} = 75$Å, respectively. The conductance spectra were measured in the PCAR setup from liquid-helium temperature to room temperature. To realize the point contact experiments, we used mechanically cut fine tips of Pt-Ir, chemically etched in a 40% solution of HCl in an ultrasound bath. Samples and tips were placed in the PCAR probe and the electrical contacts (two on the tip, and two on the first YBCO basis) were realized by indium drops. In Fig. 4.15 we show the geometry of the junction and the voltage-current terminals.

4.3.3. Results and discussion

We present now the conductance spectra obtained between a YBCO/LCMO bilayer and a Pt-Ir tip. We remark that our transport measurements include two different interfaces, YBCO/LCMO and LCMO/Pt-Ir, both responsible for the profile of the conductance curves. The different contributions can be evidenced for instance in the lowest-temperature spectrum (see the inset of Fig. 4.16), characterized by an asymmetric, "V"-shaped background, with the presence of a Zero Bias Conductance Peak (ZBCP). The "V"-shaped background, similar to that reported for other metallic oxide junctions [141, 41], is a signature of the LCMO/Pt-Ir junction, while the YBCO layer is responsible for the asymmetry [55]. On the other hand, the ZBCP is a consequence of the *d-wave* symmetry of the superconducting order parameter of YBCO, indicating the formation of the Andreev bound states at the YBCO Fermi level [55, 50, 175, 91]. Moreover, the presence of a ZBCP suggests that our tunnel

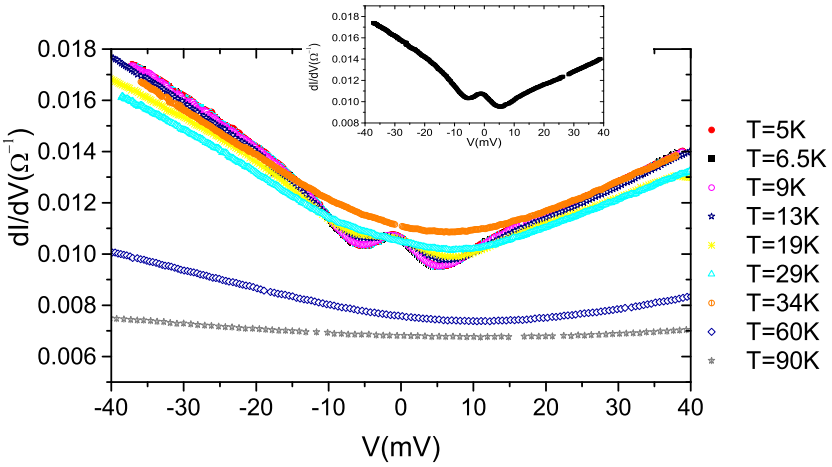

FIGURE 4.16. Temperature dependence of a highly stable junction between the YBCO/LCMO bilayer and the Pt-Ir tip. We notice that a ZBCP appears at low temperatures and disappears at about 30K. The lowest-temperature spectrum is detailed in the inset.

junction is not completely c-axis oriented, but a component in the a-b plane is present as well.

The nature of the ZBCP can be experimentally investigated by following the temperature evolution of the conductance spectra. In the case of PCAR on pure YBCO, the literature reports a ZBCP decreasing with increasing temperature, and vanishing at the critical temperature of YBCO (~ 90 K) [55]. In our YBCO/LCMO junction (see Fig. 4.16), we observe instead a depressed ZBCP. According to the theory of spin transport between a ferromagnetic material and a d-wave superconductor, the depression of the ZBCP follows from the suppression of Andreev reflections at the interface, due to the spin polarization of the ferromagnetic layer [183, 92]. In the measured conductance spectra, the ZBCP disappears at a temperature of about $T_c \sim 30$ K, which is in agreement with the resistivity measurements on YBCO/LCMO bilayers [51]. This fact provides further evidence that the ZBCP is a consequence of the superconducting nature of YBCO and is not due to spurious effects like inelastic tunneling via localized magnetic moments in the barrier region [49].

From our conductance spectra, the amplitude of the superconducting order parameter of YBCO can be inferred as well. Namely, we can fit the background according to the model [4, 111]:

$$G(V) = \frac{dI}{dV} \propto \frac{d}{dV} \int N_{FM}(E) N_{SC}(E + eV)[f(E) - f(E + eV)]dE, \tag{4.6}$$

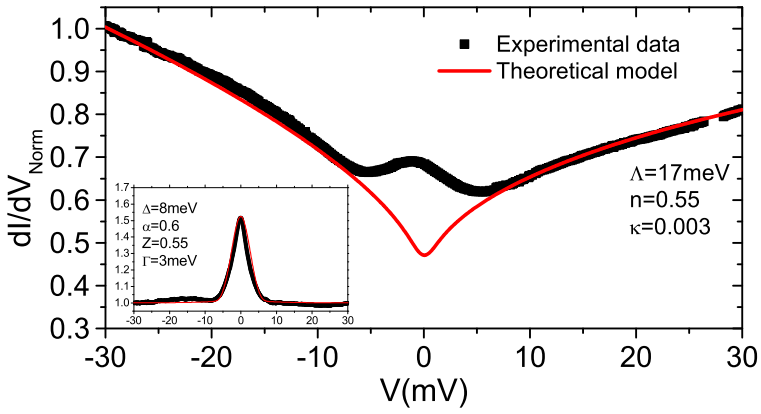

FIGURE 4.17. The conductance spectrum with the fitted background. In the inset the YBCO conductance curve is shown with the best fit with *d-wave* symmetry of the order parameter.

where N_{SC} is the density of states of the YBCO layer, and N_{FM} is the density of states of the LCMO layer. The latter can be expressed as $N_{FM}(E) = N_{FM}(0)[1 + (|E|/\Lambda)^n]$, where Λ is a constant associated with the electron correlated energy of LCMO at the interface and the exponent $0.5 < n < 1$ reflects the degree of disorder in LCMO near the YBCO/LCMO interface. Concerning the YBCO, we can assume that, for bias voltages larger than the superconducting energy gap, N_{SC} is approximately constant, except for a linear correction taking into account for the asymmetry of the normal state of YBCO. In a window of bias voltages $V \in [-\bar{V},\ \bar{V}]$, the density of states of YBCO can thus be written as $N_{SC} = 1 - \kappa(V + \bar{V})$, where κ is the asymmetry factor and the total conductance is normalized such that $G(-\bar{V}) = 1$.

In Fig. 4.17, we show the lowest-temperature conductance spectrum, together with the best fitting curve for the background, following Eq. 4.6. The superconducting energy gap of YBCO corresponds to the bias voltage at which the theoretical curve for the background deviates from the experimental conductance spectrum. From Fig. 4.17, we can estimate an energy gap $\Delta \sim 8$ meV. The contribution of the YBCO layer to the conductance characteristic can then be obtained dividing the measured differential conductance (at the lowest temperature) by the modeled background curve: $G_{\mathrm{YBCO}}(V) = G(V)_{exp}/G(V)_{back}$. We can satisfactorily fit the spectrum $G_{\mathrm{YBCO}}(V)$ with a d-wave BTK model, Eqs. 2.17–2.21 (for details see Sec. 2.2), regarding as fitting parameters the superconducting gap Δ, the barrier strength Z, the angle α of the order parameter and the smearing factor Γ. Remarkably (see the inset of Fig. 4.17), the fitting provides a gap $\Delta = 8$ meV, consistent with our previous findings. This value, smaller than the reported

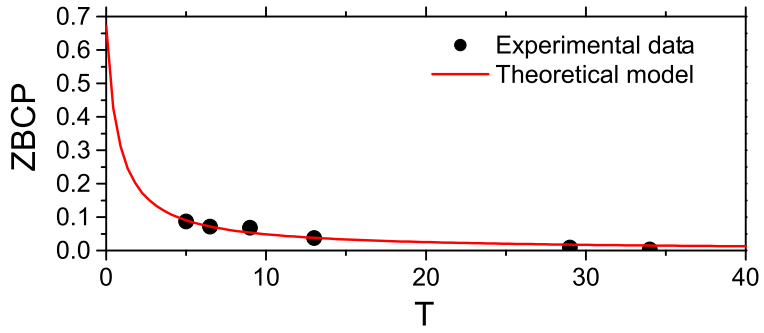

FIGURE 4.18. Temperature dependence of ZBCP (dots) with the best theoretical fit (solid line).

gap value of 20meV for YBCO [55], can be explained by the proximity effect of the Cooper pairs from YBCO to LCMO, or by the injection of spin-polarized electrons from LCMO to YBCO [111].

It has been theoretically predicted that, in a F/S interface, the amplitude of the spin polarization of the ferromagnetic layer can be estimated from the temperature dependence of the ZBCP. The latter is expected to be proportional to the inverse of the temperature for intermediate temperatures [83]. In Fig. 4.18 we show the temperature dependence of the ZBCP as obtained by the experimental conductance spectra of Fig. 4.16, together with the best fitting curve. With an extrapolation of the best fitting curve at low temperatures ($T \to 0$), we can directly compare our ZBCP evolution to the theoretical model of Ref. [83]. This allows us to estimate a spin polarization of the LCMO layer of about 67%, meaning that the electron spins are not fully polarized. This is consistent with the observation of a (depressed) ZBCP: in fact, it would have been completely suppressed if the LCMO polarization had approached unity.

In the context of the fundamental interest on the interplay between superconductivity and ferromagnetism, we compare in Fig. 4.19 the behavior of the ZBCP extrapolated from the temperature dependence of conductance spectra in the Ru-1212 (Fig. 4.10) and YBCO/LCMO (Fig. 4.18) tunneling junctions. We notice a similar, sublinear temperature dependence which is found to be strikingly different from the behavior of standard BCS superconductors. So the depressed ZBCP (both in height and in the temperature evolution) together with a reduced superconducting gap, as observed in both intrinsic (Ru-1212) and artificial (YBCO/LCMO) hybrid structures, are signatures of an injection of spin polarized electrons from the ferromagnetic layer, inducing peculiar modifications to the density of states of the superconducting layer.

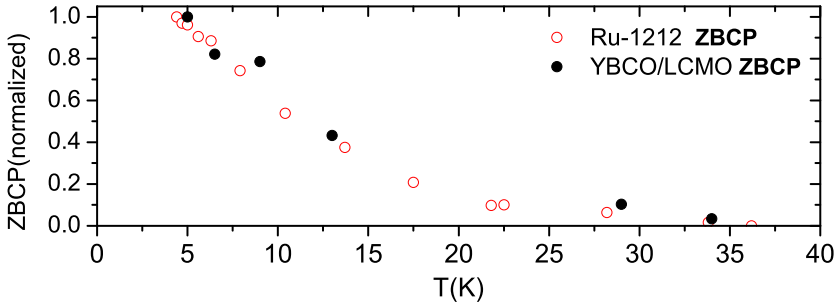

FIGURE 4.19. Temperature evolution of the ZBCP for Ru-1212 and YBCO/LCMO conductance spectra.

To summarize the results of this section, PCAR measurements on the heterostructure constituted by a YBCO/LCMO bilayer and a Pt-Ir tip have resulted in conductance spectra with a triangular ZBCP, signature of the d-wave symmetry of the order parameter of YBCO. A reduced height of the ZBCP, as compared to the case of N/S junctions, has been observed. We have shown that this effect is due to a partial polarization of the LCMO layer. A deeper analysis of the effects of one or more magnetic layers on the superconducting properties of high-T_C compounds awaits further investigation.

CHAPTER 5

REALIZATION AND CHARACTERIZATION OF HIGH PERFORMANCE π-JUNCTIONS WITH STRONG FERROMAGNETS

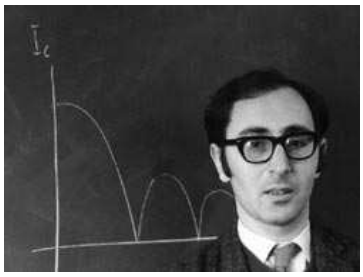

Brian Josephson (1962)
...tunneling supercurrents originally emerged out of complicated calculation of tunneling currents as terms which did not go to zero when the voltage across the barrier was put equal to zero...

In recent years a great interest has grown in the implementation of quantum computing [123], where the information is stored in two-level quantum systems (qubits). Many theoretical and experimental advances have been achieved towards the physical realization of qubits and, in this respect, solid-state implementations appear as good candidates, thanks to their potential scalability which is partly enabled by the development of nano-scale technology [57]. In particular, ferromagnetic π-junctions have been proposed as coherent two-state quantum systems [181]. In fact, as a consequence of exchange splitting of the spin-up and spin-down electrons in the ferromagnetic sub-bands, the superconducting order parameter oscillates as a function of penetration depth which causes its sign to change periodically [35, 97], as we have described in detail in Sec. 2.3. A positive order parameter corresponds to a "0"-state, while a negative order parameter to a "π"-state. To realize a practical quantum device it is necessary to control these two states with the fabrication of adapted

structures; because this is easily achieved in S/F/S systems with weak [98] and strong [26, 18, 130] ferromagnetic barriers, they have been introduced as suitable superconducting quantum-electronic devices based on π-shift technology [180]. These systems exhibit indeed oscillations of the critical current with the thickness of the F layer, equivalent to a change of the Josephson relative phase from 0 to π. The principle goal in this research field is to understand the physics of superconductor based quantum technology and, equally, to evaluate potential material systems for their development, while aiming at reducing the size of the employed heterostructures towards and below nano-scale.

In this Chapter we explain the details of the realization of S/F/S Josephson junctions with strong ferromagnets, and the experimental magnetic and electrical-transport data with their interpretation in agreement with the theoretical models, following the results described in Refs. [S6,S9,S10].

5.1. Nb/Ferromagnet/Nb Josephson junction fabrication

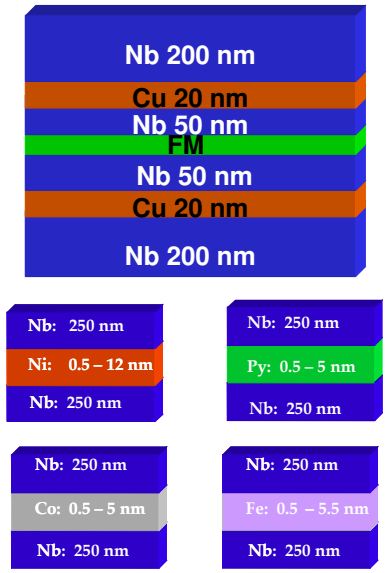

FIGURE 5.1. A schematic picture of the S/F/S heterostructure used in this work.

Our heterostructure consists of Nb (250 nm) / Ferromagnetic layer / Nb (250 nm). As ferromagnetic layer we have used: Ni, $Ni_{80}Fe_{20}$ (Py), Co and Fe. In the case of Co, Fe and Py their respective thicknesses t_F were varied from $\simeq$ 0.5-5.5 nm while, in the case of Ni, t_{Ni} was varied from $\simeq$ 1.0-10 nm. To assist processing in a focused ion beam (FIB) microscope, a 20 nm normal

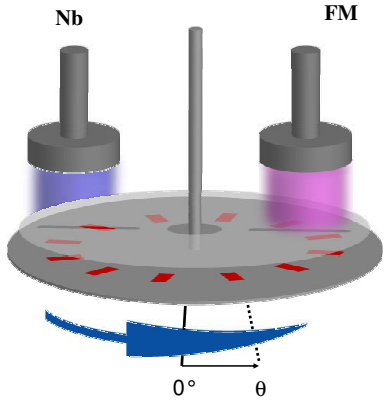

FIGURE 5.2. An illustration of the sputtering process: the ferromagnetic interlayer thickness is varied as a function of the angle θ from the pre-sputter position.

metal interlayer of Cu was deposited inside the outer Nb electrodes, but 50 nm away from the Fe barrier. We remark that the 20 nm of Cu is a thickness smaller than its coherence length, so it is completely proximitized into the Nb, and it does not affect the transport properties of the Josephson junction. Refer to Fig. 5.1 for an illustration of the our heterostructures.

The heterostructures employed in this work, have been deposited by d.c. magnetron sputtering (the details of the sputtering system are presented in Sec. 3.1.2). In a single deposition run, multiple silicon substrates were placed on a rotating holder which passed in turn under three magnetrons: Nb, Cu and the ferromagnetic layer (Fe, Co, Py or Ni). The speed of rotation was controlled by a computer operated stepper motor with a precision angle of better than 3.6° and each sample was separated by an angle of at least 10°. Prior to the deposition each target material was calibrated and the deposition rates were estimated with an Atomic Force Microscopy (see table 5.1 for a summary of the deposition parameters for all target materials presented in this work). In the case of the ferromagnetic materials (Co, Py, Fe and Ni) the rates of deposition, and hence t_F, were obtained by varying the speed of each single chip which moves under the ferromagnetic target while maintaining constant power to the magnetron targets and Ar pressure. This was achieved by knowing the chip position relative to the target material (θ) and by programming the rotating flange such that a linear variation of ferromagnetic thickness with θ, $d(t_F)/d\theta$, was achieved. t_F is inversely proportional to the speed of deposition, $t_F \propto 1/V_t$, and hence it can be shown that in order to achieve a linear variation of $t_F(\theta)$ one programmes the instantaneous speed, at position θ and

Target material	Rate (nm/W at 1 rpm)	Power (W)	Speed range (rpm)	d_F ($\pm$0.2 nm)
Nb	6.89	90	.028	250
Cu	4.39	30	0.22	20
Ni	2.12	40	0.20-4.2	0.5 - 10.5
Co	1.8	40	0.36-3.6	0.5 - 5.0
Py	1.64	40	0.33-3.3	0.5 - 5.0
Fe	2.0	40	0.22-2.2	0.5 -5.0

TABLE 5.1. A summary of the deposition parameters for all materials sputtered. t_F refers to the expected film thickness.

time t seconds (i.e. $V(\theta)_t$), of deposition according to

$$V(\theta)_t = \frac{V_i V_f}{V_f - V_i}\left(\frac{V_i V_f}{V_f - V_i} - \frac{\theta}{2\pi}\right)^{-1}, \tag{5.1}$$

where V_i is the initial speed and V_f is the final speed in units of rpm. This method of varying t_F guaranteed, in all cases, that the interfaces between each layer were prepared under the same conditions while providing precise control of the F layers. Fig. 5.2 shows an illustration of the sputtering process. For each run, simultaneously, our heterostructures have been deposited on 5×5 mm^2 and 5×10 mm^2 SiO_2 substrates. The first ones have been used for the magnetic measurements, the second ones for the realization of Josephson junctions.

5.1.1. X-ray measurements

To confirm our precise control over the ferromagnetic thickness variation we performed low angle X-ray reflectivity of a set of calibration Nb/Co/Nb thin films where the Nb layers had a thickness of 5 nm and the Co barrier thickness was varied from 0.5 nm to 5.0 nm. A series of low angle X-ray scans were made and the thickness of the Co layer ($t_{Co(observed)}$) was extracted by fitting the period of the Kiessig fringes using a simulation package. It was found that our expected Co barrier thicknesses, $t_{Co(expected)}$, was well correlated with $t_{Co(observed)}$ with a mean deviation of $\pm$0.2 nm. Fig. 5.3 (a) shows a comparison of $t_{Co(observed)}$ with $t_{Co(expected)}$ and an example of the low angle x-ray data plotted with the equivalent simulation data where $t_{Co(observed)}$ was extracted.

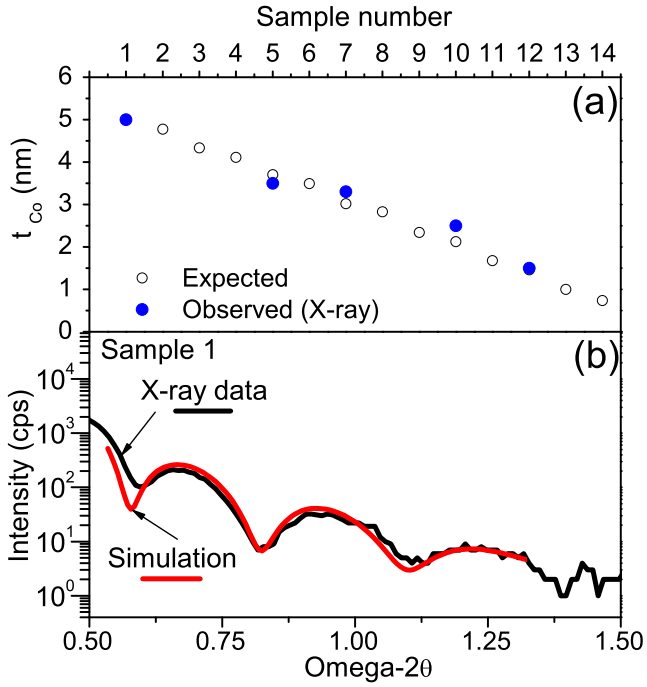

FIGURE 5.3. (a) $t_{Co(observed)}$ plotted with $t_{Co(expected)}$ extracted from simulation data, and (b)low angle x-ray data plotted with the equivalent simulation for sample 1 where $t_{Co(expected)}$ =5 nm and $t_{Co(observed)}$ =5±0.2 nm . The mean deviation is estimated to be ±0.2 nm.

5.2. Nanoscale device process

We can summarize the realization of the Josephson junctions in three different steps (for details on these processes see Sec. 3.1): (i) patterning the films using optical lithography to define the micron scale tracks and the contact pads. Our mask permits etching of at least 14 devices, which allows us to measure numerous devices and to derive good estimates of important parameters, like, for example, characteristic voltage (see Fig. 5.4 to see an illustration of the mask); (ii) broad beam Ar ion milling (3 mAcm^{-2}, 500 V beam) to remove unwanted material from around the mask pattern, thus leaving 4μm tracks for subsequent FIB work; (iii) FIB etching of micron scale tracts to achieve vertical transport. In particular to realize our devices we have used a three-dimensional technique [94]. The wedge holder used in this work was designed by D.-J. Kang and it is schematically shown in Fig. 5.5; it is constituted by three sample lodgings, one in horizontal and two at 45°. Once loaded the sample on the 45° lodging, we can rotate the stage of the FIB

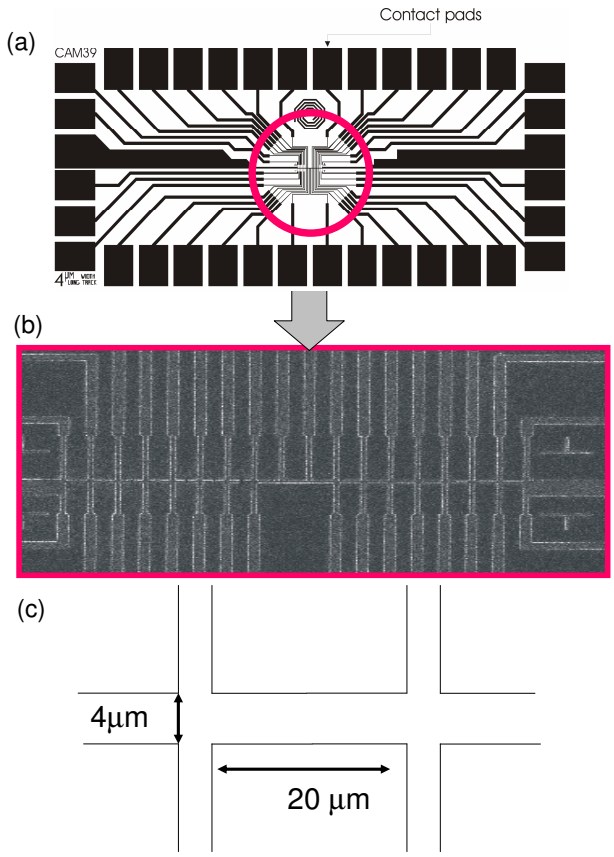

FIGURE 5.4. (a)"Cam 39" mask design for a $10 \times 5mm^2$ chip used in this work, showing contact pads for wirebonding. (b) Central detail: on each chip we realize 14 possible junctions with thinnest track widths of $4\mu m$ (c).

at 45°, in this way the beam is perpendicular to the surface of the sample, and the first cut is done; then the sample holder is rotated of 180° around an axis normal to the sample stage, to permit the vertical cut to be done (see Fig. 5.5). This setup allows to load two samples for each run.

The fabrication procedure is shown in Fig. 5.7 [19]. A first box with area $4 \times 2\mu m^2$ is milled with 150 pA to realize tracks of about 700 nm (b). The time of milling is about $1-3$ minutes, and this milling can be calibrated using the stage-current/end-point detection measurement. Fig. 5.6 shows how the milling of different layers can be distinguished, the first peak corresponds to the Nb, the two small peaks correspond to the two Cu layers, and finally the intensity decreases approaching to the SiO_2 substrate. The sidewalls of the

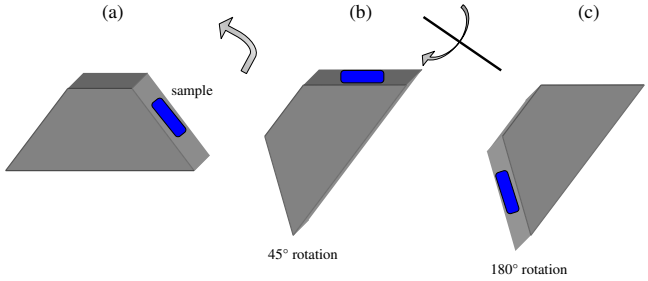

FIGURE 5.5. Schematic of the sample holder used in FIB (a) showing two axes of rotation, 45°, to horizontal milling (b) and 180° to vertical milling.

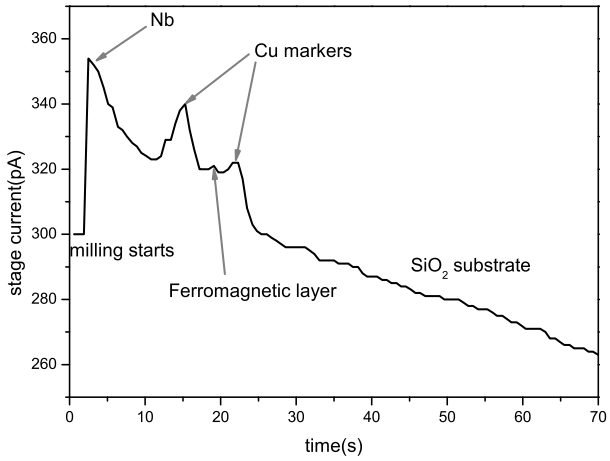

FIGURE 5.6. End Point Detector. The graph shows the stage current as a function of the milling time, we can distingue the Nb layer, the two Cu layers, the Ferromagnetic barrier and when the current decreases we have reached the substrate.

narrowed track are then cleaned with a beam current of 11 pA. This removes excessive gallium implantation from the larger beam size of the higher beam currents. The cleaning takes $\sim$ 25-30 seconds per device. The track width is then $\leq$ 500 nm. The sample is then tilted to $\theta = 90°$, and the two cuts are made with a beam current of 11 pA to give the final device (Fig. 5.7 (d)) with a device area in the range of $0.2 - 1\ \mu\text{m}^2$. This technique permits to achieve vertical transport of the current: in Fig. 5.7 (e) we show a schematic picture of the current path. In Fig. 5.8 the final FIB image of a Nb/Cu/Co/Cu/Nb device is presented.

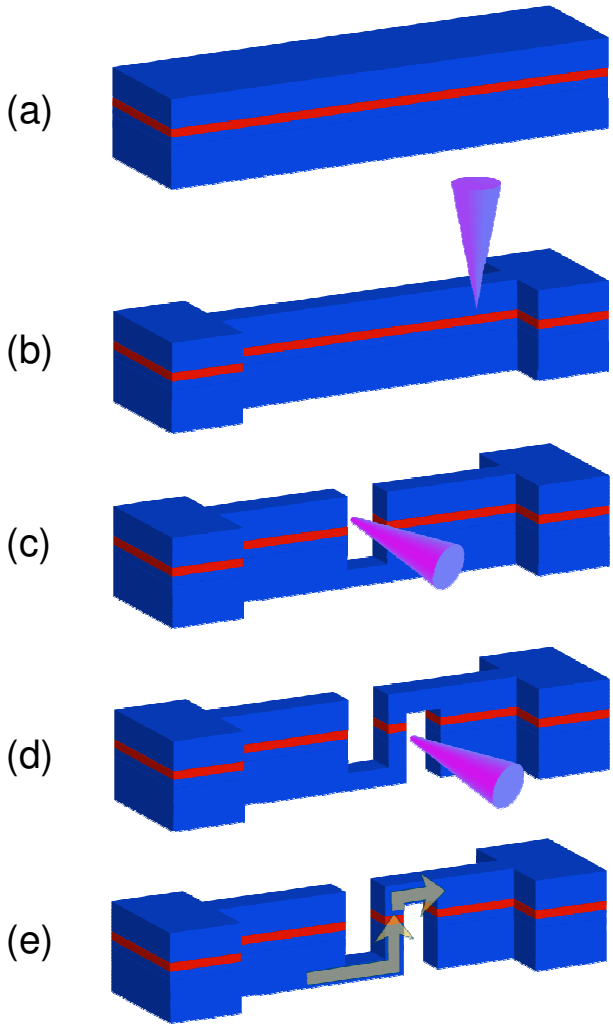

FIGURE 5.7. FIB procedure for device fabrication: the initial trilayer after the photolithography and ion-milling (a) is cut with 150 pA beam (b) and then with 11 pA beam (c-d). (e) At the end two side cuts are realized to create the final device structure with a device area in the range of $0.2 - 1$ μm^2 achieving vertical transport of the current

5.3. Magnetic measurements

In this section we report magnetic measurements of Nb Josephson junctions with strongly ferromagnetic barriers: Ni, $Ni_{80}Fe_{20}$ (Py), Co and Fe. From measurements of the magnetization saturation as a function of the Fe thickness,

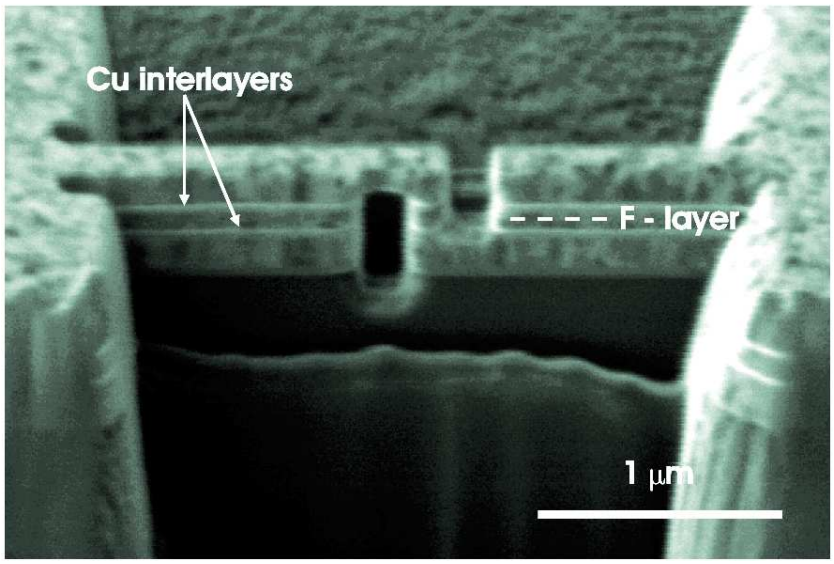

FIGURE 5.8. FIB image of a Nb/Cu/Co/Cu/Nb device, the two light gray lines are the Cu markers.

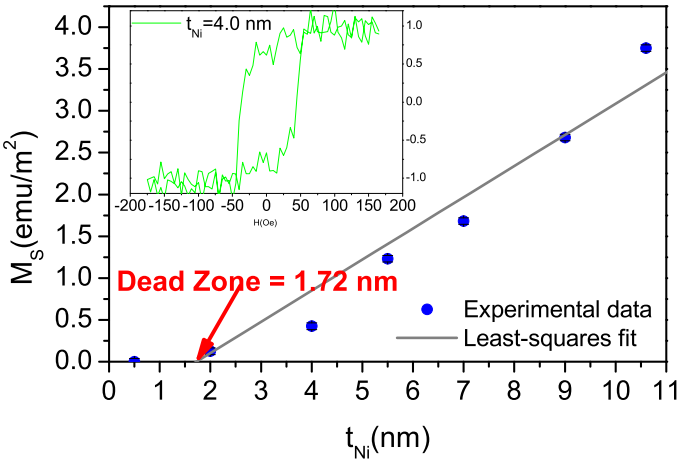

FIGURE 5.9. Saturation magnetization versus thickness of the Ni barrier, inset: hysteresis loop for $t_{Ni} = 4nm$.

our heterostructures have shown a magnetic dead layer ranging between 0.5 nm and 1.7 nm. In the case of Ni barrier we estimate its Curie temperature.

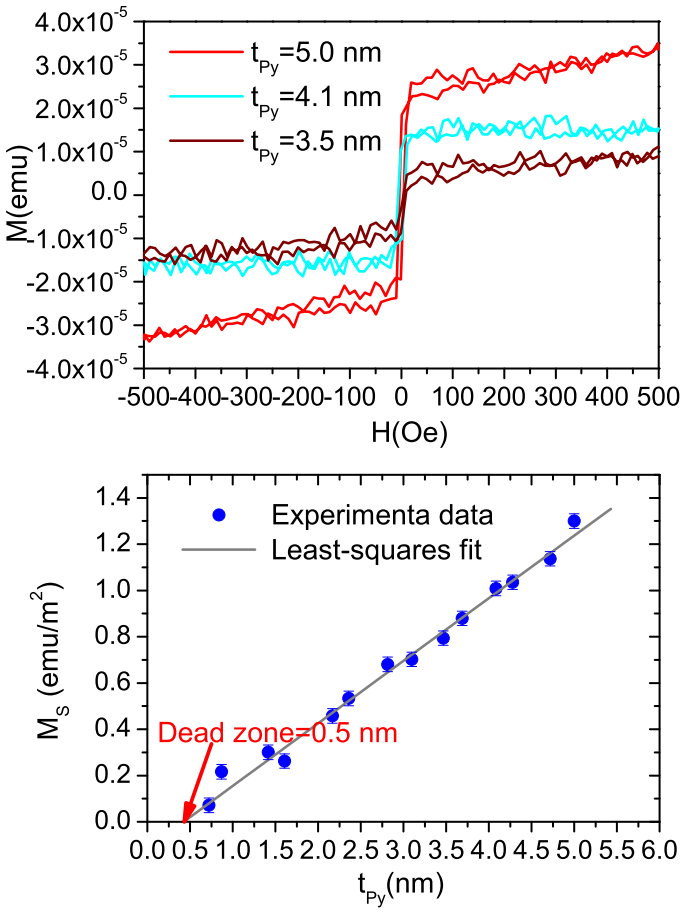

FIGURE 5.10. (a) hysteresis loops for different Co thicknesses. (b) Saturation magnetization versus thickness of the Co barrier. From

5.3.1. Measurement of the magnetic dead layer

In this section we explain the magnetic properties of Nb-Ni-Nb, Nb-Py-Nb, Nb-Co-Nb and Nb-Fe-Nb heterostructures as a function of F thickness.

To this aim we have studied, using a VSM at room temperature (for details see Sec. 3.5), the hysteresis loop of our heterostructures in order to follow the evolution of the magnetization as a function of the applied magnetic field. In Fig. 5.9 (inset), Fig. 5.10 (a), 5.11 (a) and 5.12 (a), we show a collection of hysteresis loops for different thicknesses of the F barrier. We notice that both the saturation magnetization and the width of the hysteresis loop, as expected, decrease with decreasing F layer thickness, and the ferromagnetic order disappears when the F barrier goes to zero. Furthermore from the

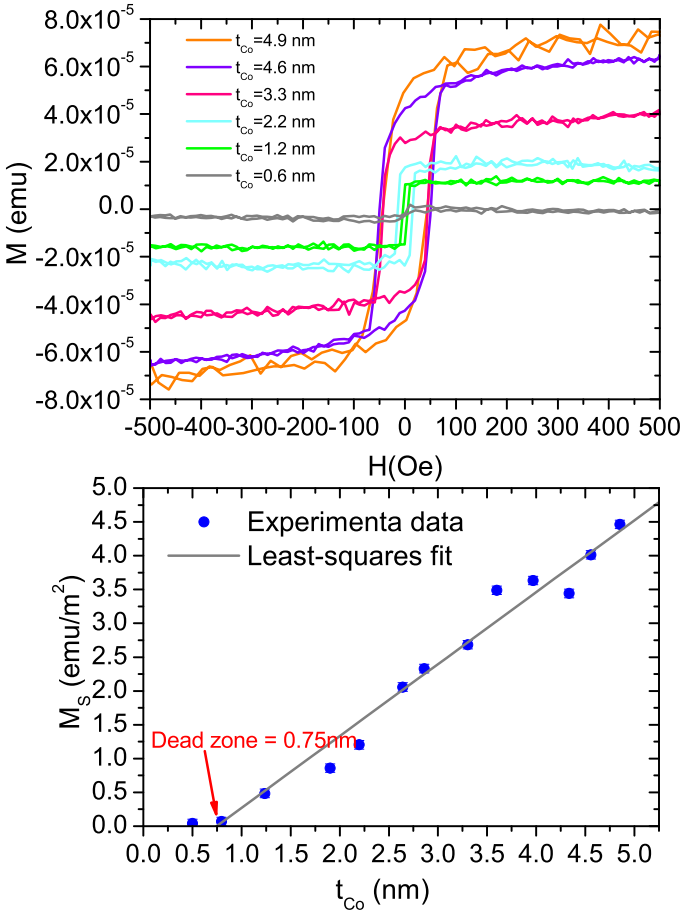

FIGURE 5.11. (a) hysteresis loops for different Co thicknesses. (b) Saturation magnetization versus thickness of the Co barrier. From the linear fit (gray line) the magnetic dead layer is extrapolated.

hysteresis loops we have measured the saturation magnetization as a function of the F barrier to extrapolate the magnetic dead layer.

The presence of a magnetic dead layer has been reported in other studies of S/F/S heterostructures [21, 28] and it can be explained as a loss of magnetic moment of the heterostructures. The magnetic dead layer can be due to numerous factors, as, for example, lattice mis-match at the Nb-F interface resulting in a reduction in the ferromagnetic atomic volume [95] and crystal structure which leads to a reduction in the exchange interaction between neighboring atoms. This loss in exchange interaction manifests itself as a loss in magnetic moment due to a collapse in the regular arrangement of electron

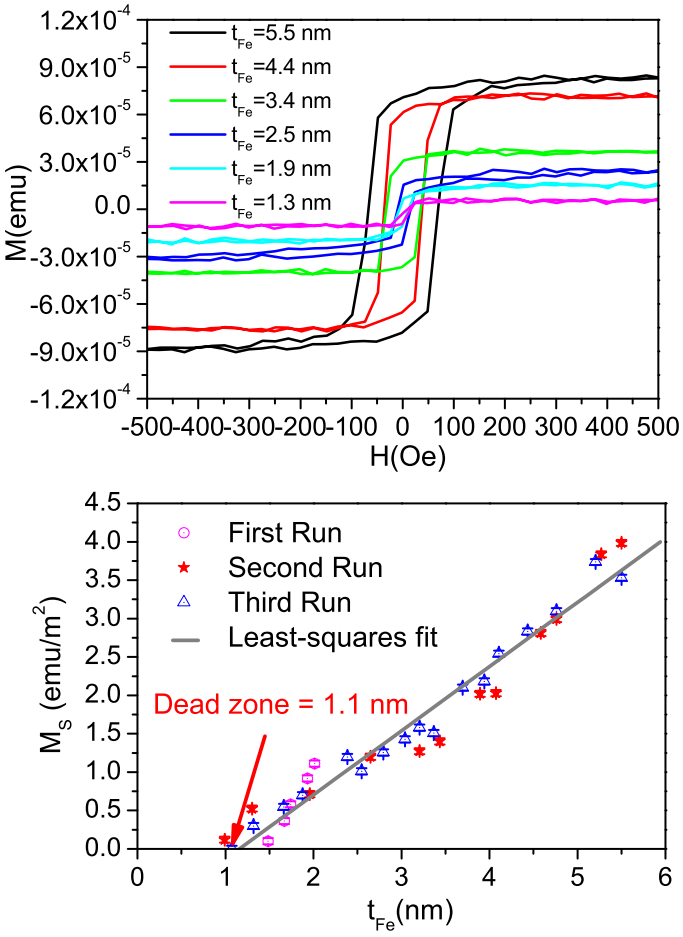

FIGURE 5.12. (a) hysteresis loops for different Fe thicknesses. (b) Saturation magnetization versus thickness of the Iron barrier for three different deposition runs. From the linear fit (gray line) the magnetic dead layer is extrapolated.

spin and magnetic moment and can lead to the suppression in T_{Curie} and E_{ex} [1, 182, 106, 133]. Another factor can be the inter-diffusion of the ferromagnetic atoms into the Nb. Like in the case of lattice mis-match this would result in a breakdown of the crystal structure at the interface leading to a reduction in the exchange interaction. The knowledge of the magnetic dead layer is a crucial point within the implementation of π-technology, to guarantee the reproducibility and the control of the devices.

Extrapolating with a linear fit the saturation magnetization as a function of F thickness, we have obtained the estimation of the magnetic dead layer:

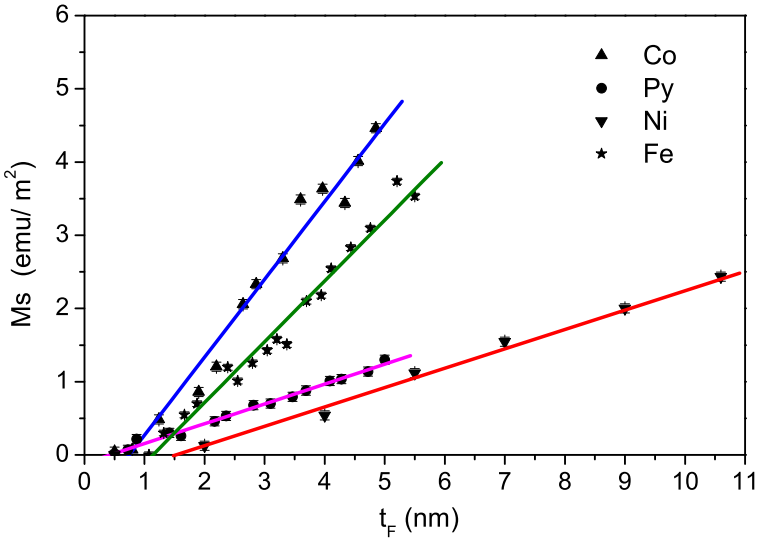

FIGURE 5.13. Saturation magnetization *vs* Ni, Py, Co and Fe thickness at T= 300K.

∼1.7 nm for Ni (see Fig. 5.9), ∼ 0.5 nm for Py (see Fig. 5.10 (b)) and ∼ 0.75 nm for Co (see Fig. 5.11 (b)).

In the case of Fe the saturation magnetization was measured for three different deposition runs (see Fig. 5.12). For each deposition we have obtained similar saturation magnetization and by extrapolating the least-squares fit of these data we have estimated a Fe magnetic dead layer of ∼ 1.1 nm.

In Fig. 5.13 we summarize the magnetic moment *vs* thickness for Ni, Py, Co and Fe. From these data we can extrapolate the slope of M_S *vs* t_F.

From the theoretical model [157, 129] the predicted slopes are: $\simeq$ 0.60 emu/cm^3 for Ni, $\simeq$ 0.52 emu/cm^3 for Py, $\simeq$ 1.42 emu/cm^3 for Co and $\simeq$ 2.6 emu/cm^3, for Fe. On the other hand from our experimental data the slopes of M_S *vs* t_F for these ferromagnetic materials are suppressed from these expected bulk values: 0.27 emu/cm^3 for Ni, 0.27 emu/cm^3 for Py, 1.0 emu/cm^3 for Co and 0.83 emu/cm^3 for Fe. We can argue that, in our case, we are not considering bulk materials, as reported from Slater and Pauling, instead our systems are constituted by F/S sandwiches, so the presence of a superconducting layer, Nb, can induce a weakening of the ferromagnetic properties of the F layer and a possible diffusion of the Nb into the F barrier.

5.3.2. Calculation of the Curie temperature

In the case of Ni we have followed the temperature dependence of the magnetization for two different thicknesses of Ni barrier so that an estimation of

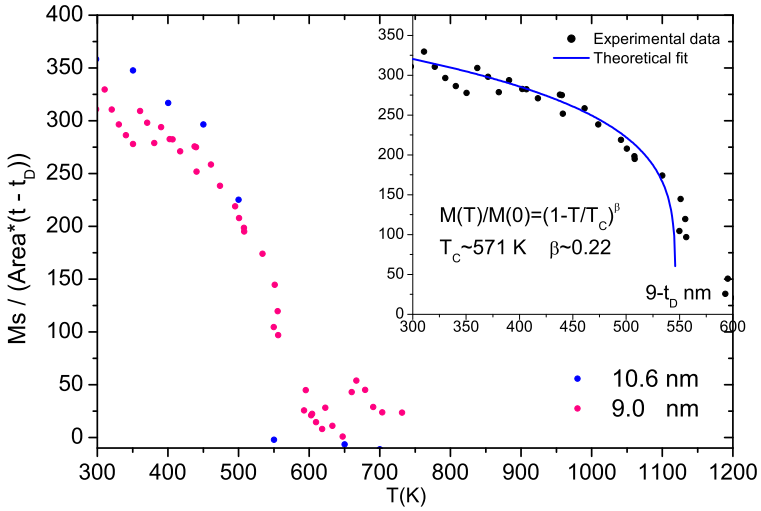

FIGURE 5.14. Magnetization as a function of temperature for a Nb/Ni/Nb trilayer, inset: experimental data with the best fitting curve to extrapolate the Curie temperature of Ni. t_D is the magnetic dead layer.

T_{Curie} could be made (see Fig. 5.14). The experimental data are modeled by the following formula:

$$M(T)/M(0) = (1 - T/T_{Curie})^{\beta}$$

where M(0) is the magnetization at absolute 0 K, T is the measuring temperature, and β and T_{Curie} are fitting parameters. We have estimated $T_{Curie} \sim 571$ K, which is in agreement with $T_{Curie} = 620$ K measurements of Ni in F/S bilayers [24]. This provides evidence that our Ni is consistent and not grossly degraded. In addition the warming and cooling data follow each other implying that no interdiffusion has influenced the M(T) curves.

5.4. Transport measurements

In this section we present the $I(V)$ *vs* V curves for the Nb/F/Nb Josephson junctions varying the thickness of the F barrier. All these materials show multiple oscillations of critical current with barrier thickness implying repeated 0-π phase-transitions in the superconducting order parameter. The critical current oscillations have been modeled with the clean and dirty limit theoretical models, from this analysis we have extrapolated the exchange energy and the Fermi velocity of the ferromagnetic barrier.

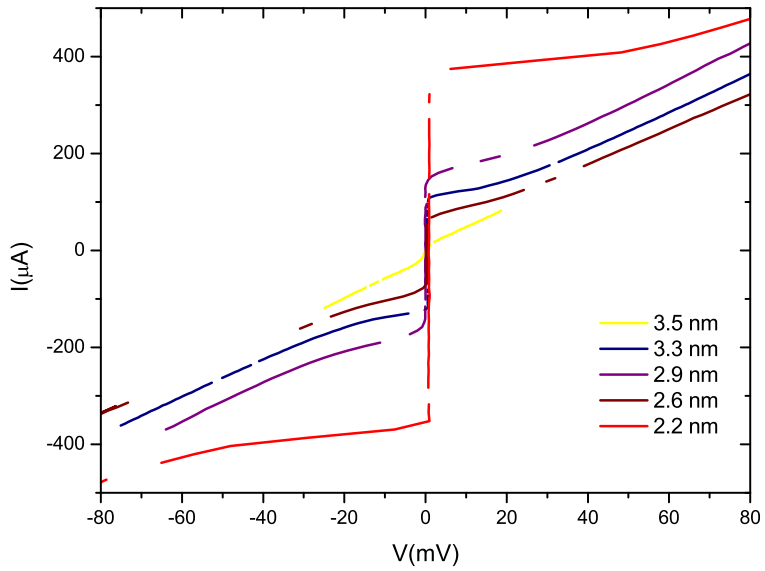

FIGURE 5.15. $I-V$ characteristics for Nb/Co/Nb Josephson junctions with different Co thickness.

5.4.1. Critical current oscillations

For several junctions on each chip we have measured the current versus voltage from which the critical current (I_C) and the normal resistance (R_N) of the Josephson junction have been extrapolated. In Fig. 5.15 we show an example of I *vs* V curves for different Co thicknesses, we notice that for each curve we have roughly the same resistance, that means the same area of the Josephson junctions. This is an indication of the good control on the fabrication of the devices with the FIB.

The I_CR_N products, as a function of F barrier thickness, exhibit a decaying, oscillatory behavior, in agreement with the theoretical predictions (see Sec. 2.3).

The oscillations of I_CR_N as a function of Ni, Py, Co and Fe thicknesses at 4.2 K are shown in Figs. 5.16 (a)-(b) and Figs. 5.17 (a)-(b).

In the case of Py, the clean limit model, Eq. 2.27, closely matches the experimental data up to a thickness of $\simeq$ 2 nm, while in the case of Ni the oscillations are explained by the clean limit theory up to $\simeq$ 7 nm. Above these values a better fit is obtained using a formula for a diffusive and high E_{ex} ferromagnet, Eq. 2.28. For Eq. 2.27 the fitting parameters are the E_{ex} and the Fermi velocity v_F. In the case of Eq. 2.28 the fitting parameters are: v_F, the mean free path L, the superconducting energy gap Δ and E_{ex}. But L and Δ are not free parameters, because they are fixed by the theoretical predictions.

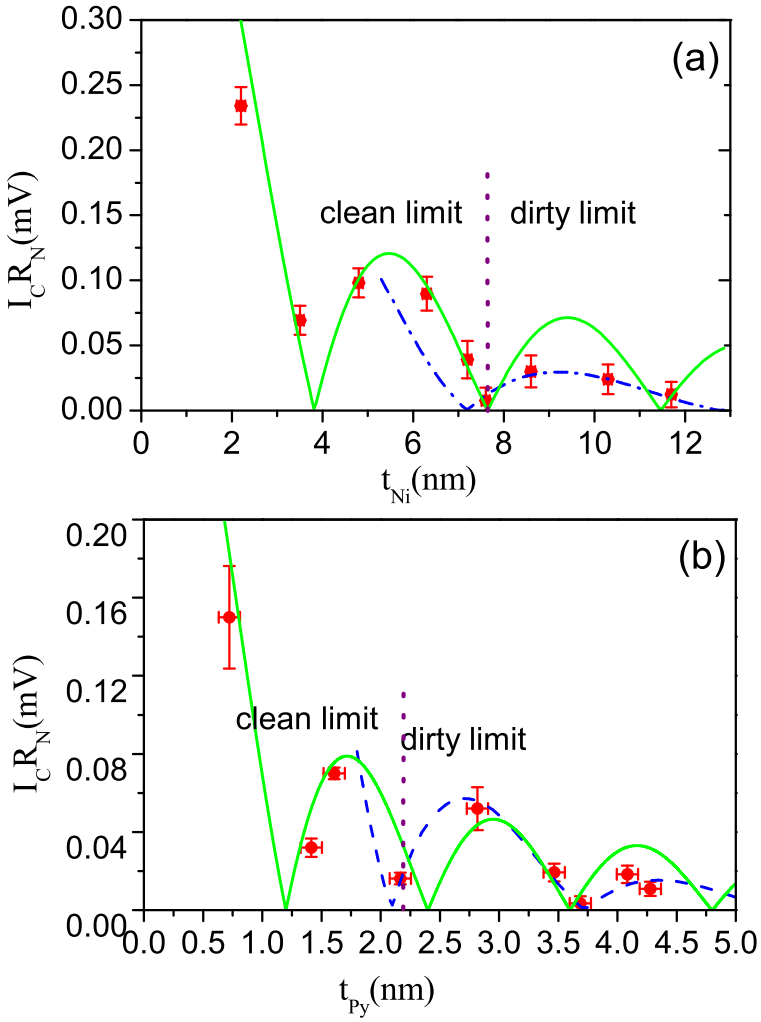

FIGURE 5.16. Oscillations of the $I_C R_N$ product as a function of the thickness of the Ni (a) and Py (b) barrier. The solid green line is the theoretical fit in agreement with Eq. 2.27, dash-dot blue line is referred to Eq. 2.28.

In this way the only free parameters are, as for the clean limit equation, the Fermi velocity and the exchange energy. Using Eq. 2.28 we obtain the best fitting values for Ni: $v_F(Ni) = 2.8 \times 10^5$ m/s and $L_{Ni} \simeq 7$ nm; while for Py $v_F(Py) = 2.2 \times 10^5$ m/s and $L_{Py} \simeq 2.3$ nm and $\Delta = 1.3$ meV. These values are consistent with the ones used in Eq. 2.27 and elsewhere [26, 21]; while for the exchange energy we estimate $E_{ex}(Ni) \simeq 80$ and $E_{ex}(Py) \simeq 201$

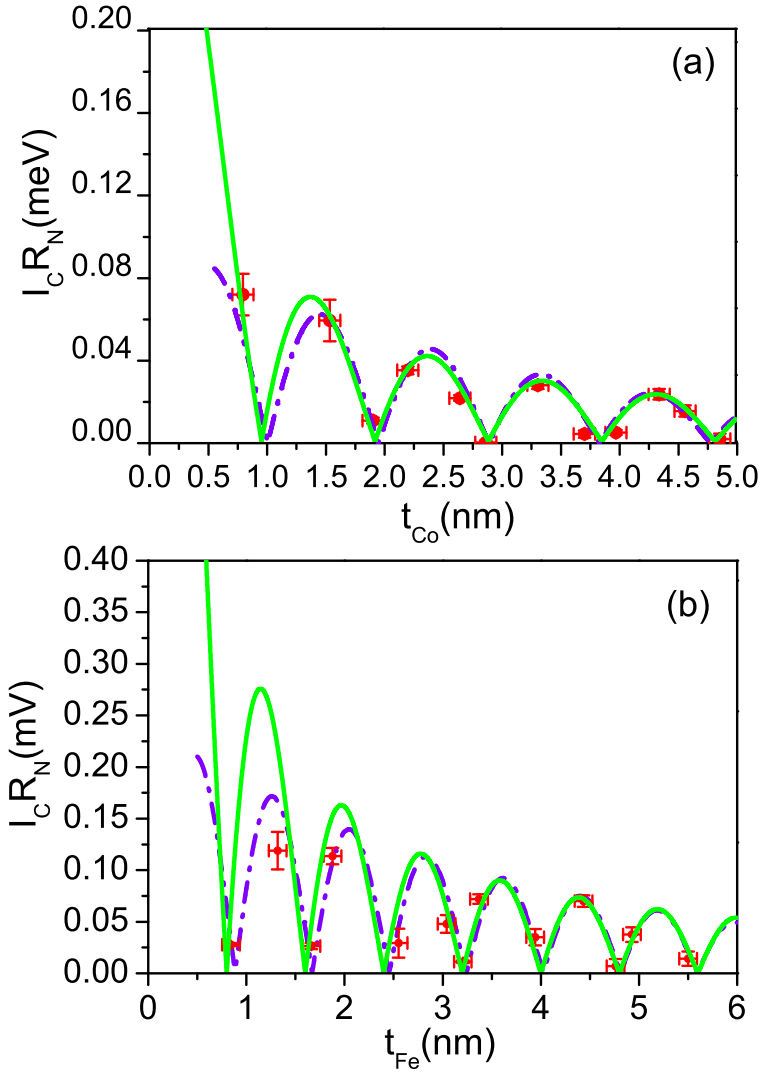

FIGURE 5.17. $I_C R_N$ *vs* t_{Co} (a) and t_{Fe} (b) with the best fitting theoretical model in agreement with Eq. 2.26, dash-dot violet line, and Eq. 2.27 solid green line.

meV. $E_{ex}(Ni)$ is close to other reported values by photoemission experiments [81], but smaller than that reported by other authors [26]. The smaller than expected $E_{ex}(Ni)$ is a consequence of impurities and possibly interdiffusion of Ni into Nb. Anyway, from the magnetic measurements the extrapolated value of the T_{Curie} provides evidence that our Ni is of acceptable quality. The $E_{ex}(Py)$ is consistent with the expected value and is approximately twice

that measured in Nb/Py/Nb junctions deposited with epitaxial barriers where $E_{ex} \simeq 95$ meV [21].

On the other hand for Co and Fe the thicknesses range all in the clean limit, so the experimental data have been modeled with the general formula, Eq. 2.26, and ξ_1 and ξ_2 are the two fitting parameters. We can see that the experimental data are in good agreement with the theoretical model.

In particular for the Co data, from the theoretical fit shown in Fig. 5.17(a) we find that the period of oscillations is $T = 1.91$ nm, hence $\xi_2 \sim 0.30$ nm and $\xi_1 \sim 3.0$ nm. In the clean limit, $\xi_2 = v_F\hbar/2E_{ex}$. In this way, known ξ_2 and estimating the Fermi velocity of being $v_F = 2.8 \times 10^5$ m/s, as reported in literature, we can calculate the exchange energy of the Co: $E_{ex} = \hbar v_F/2T \approx$ 309 meV.

For Fe, from the theoretical fit we obtain $\xi_1 = 3.8$ nm and $\xi_2 = 0.25$ nm. So the period of the oscillations is $T = 1.6$ nm. Known ξ_2 and $v_F = 1.98 \times 10^5$ m/s [48], we can calculate the exchange energy of the Iron: $E_{ex} = \hbar v_F/2T \approx$ 256 meV.

To confirm that our oscillations are all in the clean limit (meaning that the considered Co and Fe thickness are always smaller than the Co and Fe mean free path), we have modeled our data with the simplified formula which holds only in this limit, Eq. 2.27, where in this case E_{ex} and v_F are the two fitting parameters. From the theoretical fit we obtain $E_{ex}(Co) = 309$ meV, $v_F(Co) = 2.8 \times 10^5$ m/s and $E_{ex}(Fe) = 256$ meV, $v_F(Fe) = 1.98 \times 10^5$ m/s. We remark that the best fits are obtained with exactly the same values as previously reported from Eq. 2.26. Both models provide excellent fits to our experimental data showing multiple oscillations of the critical current in a tiny (nano-scale) range of thicknesses of the Co and Fe barrier.

5.4.2. Estimation of the mean free path

With a simplified model that is obtained solving the linear Eilenberger equations [76] we can estimate the mean free path for Co and Fe. The general formula is:

$$\tanh \frac{L}{\xi_{eff}} = \frac{\xi_{eff}^{-1}}{\xi_0^{-1} + L^{-1} + i\xi_H^{-1}} \tag{5.2}$$

where ξ_{eff} is the effective decay length given by $\xi_{eff}^{-1} = \xi_1^{-1} + i\xi_2^{-1}$, ξ_o is the Ginzburg-Landau coherence length and ξ_H is a complex coherence length. In the clean limit $1 + L\xi_0^{-1} >> \frac{1}{2}\max\{\ln(1 + L\xi_0^{-1}), \ln(L\xi_H^{-1})\}$. The solution of Eq. 5.2 gives

$$\xi_1^{-1} = \xi_0^{-1} + L^{-1}, \xi_0 = \frac{v_F\hbar}{2\pi T_c k_B}, \xi_2 = \xi_H = \frac{v_F\hbar}{2E_{ex}}, \tag{5.3}$$

and the numerical solution is shown in Fig. 5.18.

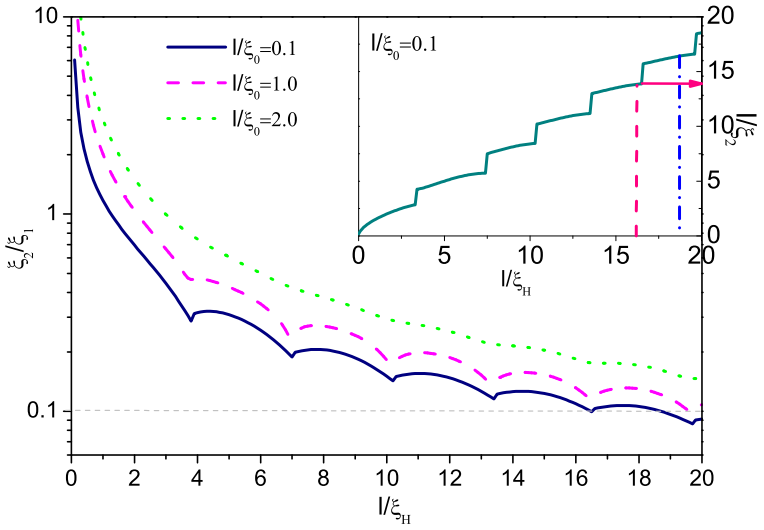

FIGURE 5.18. Estimation of Co mean free path. The dependence of ξ_2/ξ_1 with inverse magnetic length, L/ξ_H, calculated for different ratios of L/ξ_0. Inset: inverse decay length, $L/\xi_2 = f(L/\xi_0)$ for when $L/\xi_H \simeq 0.1$

In the case of Co, following this method we find from Fig. 5.18 that the experimental ratio $\xi_2/\xi_1 \simeq 0.1$ corresponds to two inverse magnetic lengths of $L/\xi_H \simeq 16.5$ and $L/\xi_H \simeq 18.7$. By assuming $L/\xi_0 \simeq 0.1$ and for the estimated parameters $\xi_1 \simeq 3$ nm and $\xi_2 \simeq 0.3$ nm we obtained, from the inset in Fig. 5.18 that for $L/\xi_H \simeq 16.5$ and $L/\xi_H \simeq 18.7$ the mean free path $L \simeq 5$ nm. Furthermore to validate the determined mean free path of our Co thin film we have estimated $L(Co)$ in a 50 nm thick Co film by measuring its resistivity as a function of temperature using the Van der Pauw technique. The transport in Co thin films is dominated by free-electron-like behavior [75] and hence the maximum mean free path is estimated from $L = \hbar k_F/n_e e^2 \rho_b$, where n_e is the electron density for Co and is estimated from the ordinary Hall effect to be 5.8×10^{28} cm^{-3} [100] and ρ_b is the residual resistivity. The residual resistance ratio $((\rho_T + \rho_b)/\rho_b)$ was measured to be $\simeq 1.41$ and hence we calculate L_{Co} at 4.2 K to be 10 nm. This verifies that our assumption that for Co the oscillations are all in the clean limit is well justified.

The same method can be done to estimate the mean free path for Fe. In this case the ratio $\xi_2/\xi_1 \simeq 0.06$, so supposing L/ξ_0=0.2, we can extrapolate from the graphical solution (Fig. 5.19) a value of $L/\xi_H \simeq 29$. Considering the curve L/ξ_2 *vs* L/ξ_H (see inset in Fig. 5.19) we obtain a value L/ξ_2 of about 25 and we estimate the value of the mean free path of about 6nm. With this analysis

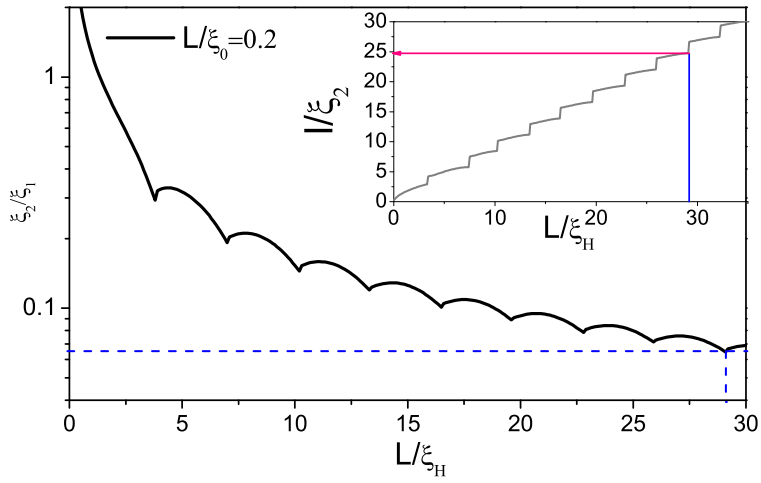

FIGURE 5.19. Estimation of Fe mean free path. ξ_2/ξ_1 *vs* L/ξ_H, calculated for different ratios of $L/\xi_0 = 0.2$.Inset: L/ξ_H *vs* L/ξ_H to estimate the mean free path, L.

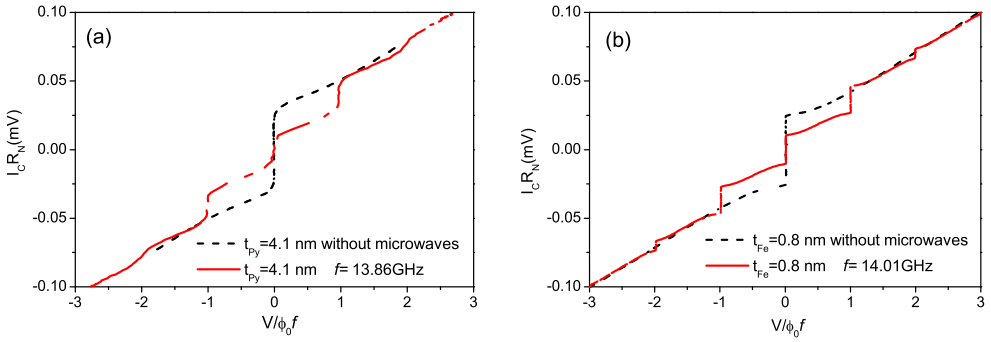

FIGURE 5.20. A typical I *vs* V curve of a Josephson junction with 4.1 nm of Py (a) and 0.8 nm of Fe (b) (black dash line) and the integer Shapiro steps in the voltage-current curve with an excitation at 13.86 GHz (a) and 14.01 GHz (red line). $\phi_0 = h/2e$

we can remark that for Co and Fe the condition that all the thicknesses are in the clean limit is unambiguously fulfilled.

5.4.3. Shapiro steps and Fraunhofer pattern

In Fig. 5.20 we show an example of typical I *vs* V characteristics for a sample with a barrier of 4.1 nm of Py (a) and 0.8 nm of Fe (b). For these $I(V)$ curves we also show the effect of an applied microwave field with an excitation at $f = 13.86$ GHz and $f = 14.01$ GHz, respectively. Constant voltage Shapiro

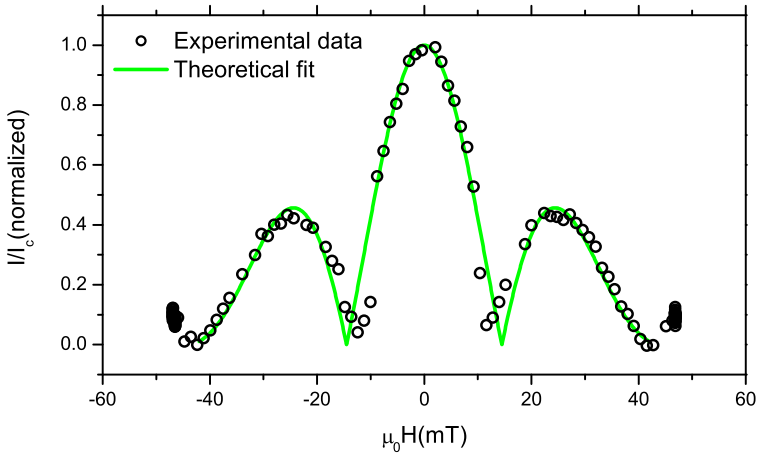

FIGURE 5.21. Magnetic field dependence of the critical current of a Nb/Fe/Nb Josephson junction with 2.5 nm of Fe with the best theoretical fit in agreement with Eq. 2.15.

steps appear due to the synchronization of the Josephson oscillations on the applied excitation [15]. As expected the steps manifest at voltages equal to integer multiples of $hf/2e$.

A uniform magnetic field ranging between -60 mT and 60 mT has been applied through the junction barrier from a solenoid coil. Measurements of the critical current I_C as a function of the applied magnetic flux, $\mu_0 H$, reveal a Fraunhofer-like shape. In Fig. 5.21 the $I_C(H)/I_C(H=0)$ *vs* μ_0 H is shown for the Nb/Fe/Nb Josephson junction with 2.5 nm of Fe. The best theoretical fitting is obtained considering Eq. 2.15.

5.4.4. Temperature dependence of the $I_C R_N$ product

In Fig. 5.22 (b) we show the temperature dependence of the product $I_C R_N$ for different Co thicknesses. We notice that, for each Co thickness, the Josephson junction resistance remains approximately constant, slightly increasing when approaching the critical temperature of Nb ($T_C = 9.2$K), as expected. On the other hand, the critical current, and hence the product $I_C R_N$, quickly decreases with increasing T and goes to zero at the critical temperature of the Nb. This is shown explicitly, in Fig. 5.22 (b) $I(V)$ *vs* V curves for 2.2 nm of Co are presented for different temperatures.

As for the Fe data, n Fig. 5.23 we show the temperature dependence of the $I_C R_N$ product for different thicknesses of the Fe barrier. We remark that also in this case the $I_C R_N$ product, quickly decreases with increasing the temperature.

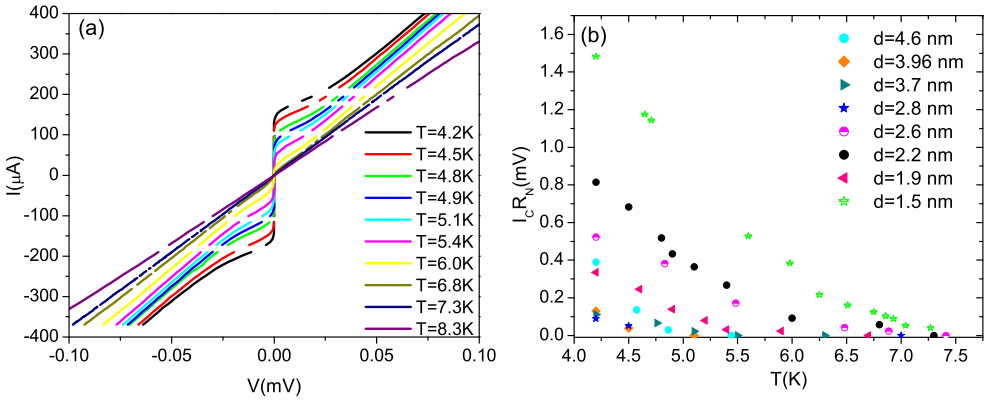

FIGURE 5.22. *I vs V* for different Co thicknesses (a); temperature dependence of the Nb/Co/Nb Josephson junction with 2.2 nm of Co(b); I_CR_N *vs* T for different t_{Co}.

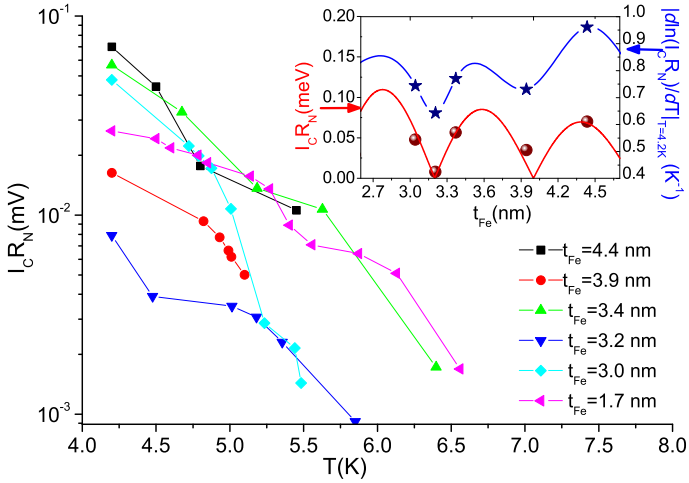

FIGURE 5.23. Temperature dependence of the I_CR_N for different thicknesses of the Fe layer (logarithmic scale). Inset: oscillations of the decay rate $\alpha_T(T_0 = 4.2\text{K})$ of I_CR_N, Eq. 5.4, with the temperature [stars; the blue line is a guide to the eye], as compared with the oscillations of the I_CR_N product itself [spheres; the red line is the fit given by Eq. 2.26] in a window of Fe thicknesses.

It is interesting to notice how the rate at which the critical current drops to zero, exhibits a non-monotonic dependence on the Fe and Co layer thickness. We can define the relative decay rate α_T of the I_CR_N product with the

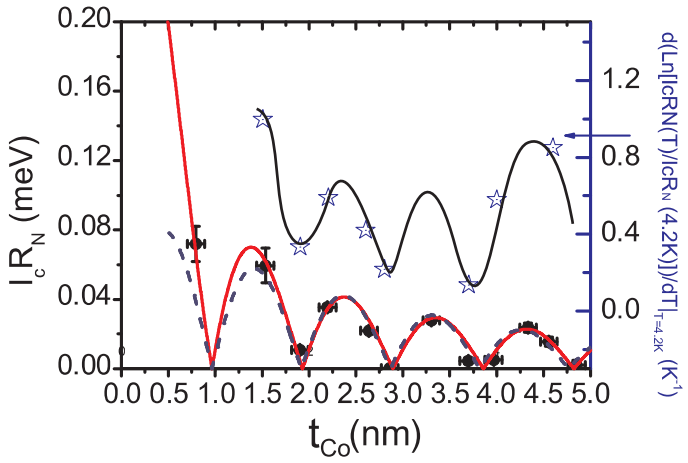

FIGURE 5.24. Oscillations of the decay rate $\alpha_T(T_0 = 4.2\text{K})$ of $I_C R_N$, Eq. 5.4, with the temperature [stars; the blue line is a guide to the eye], as compared with the oscillations of the $I_C R_N$ product itself in Nb/Co/Nb π junctions.

temperature as in Ref. [26], namely

$$\alpha_T(T_0) = \left|\frac{\mathrm{d}\ln[I_C R_N(T)]}{\mathrm{d}T}\right|_{T=T_0} = \left|\frac{\mathrm{d}I_C R_N(T)}{\mathrm{d}T}\right|_{T=T_0} \frac{1}{I_C R_N(T_0)}, \tag{5.4}$$

calculated at $T_0 = 4.2$ K. In the inset of Fig. 5.23 and in Fig. 5.24 we plot α_T as a function of t_{Fe} and t_{Co}, respectively, for consecutive thicknesses; we observe oscillations of α_T in phase with the oscillations of the $I_C R_N$, in other words the smaller $I_C R_N$ decays to zero with increasing T more slowly than the greater $I_C R_N$. A satisfactory explanation for this intriguing phenomenon awaits further investigation.

5.4.5. Summary

In summary, we have fabricated and investigated Nb/F/Nb Josephson junctions varying the Ni, Py, Co or Fe barrier thickness. A magnetic dead layer lower than 1.7 nm is extrapolated by a linear regression of the thickness dependence of the saturation magnetization. From the $I(V)$ *vs* V curves we have measured the Josephson critical current I_C and the normal resistance R_N in order to follow the oscillations of the $I_C R_N$ as a function of the F thickness. In agreement with the theoretical models for the clean and dirty limit, we have fitted the experimental data estimating the exchange energy and the Fermi

Barrier	$E_{ex}(meV)$	$v_F(\times 10^5$ m/s)	t_D(nm)
Ni	80	2.8	1.7
Py	201	2.8	0.5
Co	309	2.8	0.7
Fe	256	1.98	1.1

TABLE 5.2. Summary of the exchange energy E_{ex} and the Fermi velocity v_F extrapolated from theoretical fits of the critical current oscillations and the magnetic dead layer t_D.

velocity of the F barrier (see table 5.2 for a summary of the E_{ex} and v_F). Shapiro steps appear at integer multiples of the applied voltage. Then, for different thickness of the Co and Fe barrier, we have shown that the $I_C R_N$ product decreases with increasing temperature, and in particular the decay rate presents the same oscillatory behavior as the critical current.

With the results of this Chapter, we have shown that we are able to produce nano-structured Nb/F/Nb π-junctions with a high control of the F thickness (within an accuracy of 0.2 nm). The low magnetic dead layer gives us the possibility to reproduce the transport properties in our heterostructures with a small thickness deviation. The estimated E_{ex} is close to that of the bulk F, which implies that our films are deposited cleanly with only a small reduction in exchange energy. Interfacial roughness and possibly interdiffusion of F into Nb is assumed to account for the slightly smaller exchange energy. Moreover, in particular for Co and Fe, which exhibit oscillations all in the clean limit, the high exchange energy means small period of $I_C R_N$ oscillations, enabling us to obtain the switch from 0 to π state in a very small range of thicknesses ($\lesssim 3$ nm). We can therefore conclude that Co and Fe barrier based Josephson junctions are viable structures to the development of superconductor-based quantum electronic devices. The electrical and magnetic properties of Co and Fe are well understood and are routinely used in the magnetics industry: we have demonstrated that Nb/Co/Nb and Nb/Fe/Nb hybrids can readily be used in controllable two-level quantum information systems.

CHAPTER 6

CONCLUSIONS AND OUTLOOK

Friedrich Wilhelm Nietzsche (1844-1900)
Since I grew tired of the chase and search, I learned to find;
and since the wind blows in my face, I sail with every wind.

In this dissertation we have summarized the main results obtained during the three years of my PhD. There are two main reading keys underlying the entirety of our analysis, and acting as its common denominator. From a

motivational point of view, the main scope of our research has been to understand the physics of conventional and unconventional superconductors with the modification of their properties in presence of a ferromagnetic order. On a more technical ground, our employed tool of investigation has been, with its manifold manifestations, the Andreev reflection.

Specifically, our analysis took off in Chapter 4 from the study of a novel *s-wave* superconductor, MgB_2 (see Sec. 4.1). The superconducting microconstrictions realized between MgB_2 pellets and Nb tips have shown the Josephson current and Subharmonic Gap Structures, indicating the coupling of the Nb energy gap with the MgB_2 3D band. The subgap resonances have been explained in terms of Multiple Andreev Reflections and from this analysis we have extracted the correct temperature dependence of the Nb energy gap and the value $\Delta = 2.4$ meV for the 3D energy gap at the MgB_2 Fermi surface [S2,S8].

We have then turned our attention towards a high-T_C cuprate superconductor, $RuSr_2GdCu_2O_8$ (see Sec. 4.2), which exhibits an intrinsic coexistence with a magnetic order, qualifying itself as an atomic-size S/F heterostructure. The conductance spectra obtained on this compound have shown a triangular Zero Bias Conductance Peak, feature of the formation of Andreev bound states at the superconductor Fermi level. We have properly interpreted our experimental data by assuming a *d-wave* symmetry of the superconducting order parameter, thus estimating a value of the energy gap $\Delta = 2.8$ meV, smaller than that observed in others (non-magnetic) cuprate high-T_C superconductors. We interpreted the effective reduction of the energy gap as a consequence of the presence of ferromagnetic order within the superconducting phase [S1,S3,S4].

The reduction of the superconducting energy gap and a sublinear temperature dependence of the zero bias peak have been evidenced also in the conductance spectra obtained on $YBa_2Cu_3O_7/La_{0.7}Ca_{0.3}MnO_3$ bilayers (see Sec. 4.3). These artificial S/F heterostructures have served as an interesting testground for the investigation and interpretation of the interplay between ferromagnetism and superconductivity. In this context, we have shown that the partial suppression of the superconducting properties of $YBa_2Cu_3O_7$ (reduction of both critical temperature and gap amplitude) is due to a partial polarization of the $La_{0.7}Ca_{0.3}MnO_3$ layer [S5,S7].

Motivated by intellectual curiosity and by the sake of achieving a more fundamental understanding of the effects of the competing superconducting and magnetic orders, our interest has thereupon turned towards the analysis of conventional superconductors at the interface with more traditional ferromagnetic materials.

In Chapter 5 we have presented the details of the fabrication and investigation of Nb/F/Nb Josephson junctions, with different ferromagnetic barriers, Ni, $Ni_{80}Fe_{20}$ (Py), Co and Fe. In these systems, the suppression of the Andreev reflection due to the ferromagnetic layer, results in an exponentially decaying and oscillatory behavior of the superconducting order parameter as a function of the penetration length. Dealing with Josephson junctions, such phenomenon manifests as oscillations of the Josephson critical current, corresponding to multiple 0 to π switchings of the Josephson relative phase. The S/F/S heterostructures have been deposited in situ by dc magnetron sputtering varying only the thickness of the ferromagnetic layer in the range between 0.5 and 12 nm. From the magnetic measurements we have extrapolated a magnetic dead layer lower than 1.7 nm, which ensures the quality and reproducibility of our devices. The nanoscale junctions have been realized with optical photolithography, broad ion milling and focused ion beam. From the electrical measurements we have measured the Josephson critical current (I_C) and the normal resistance R_N in order to follow the oscillations of I_CR_N as a function of the ferromagnetic thickness. The oscillations of the critical current have been interpreted with the theoretical models to extrapolate the exchange energy and the Fermi velocity of the ferromagnetic barrier. This research has also enabled us to evaluate potential material systems (in our case, Co and Fe) for the realization of superconductor-based quantum electronic devices at the nanoscale [S6,S9,S10].

The research of new materials which stand out for their superconducting and/or magnetic properties is always open, so the necessity to study the symmetry of the superconducting order parameter and its modification due to a magnetic interface remains always a lively and exciting field. The electron-doped materials and single-crystal specimens of new members of the ruthenocuprate material family are only some examples.

On the other hand the study and the investigation of atomic-size and artificial superconducting/ferromagnetic heterostructures has given the input for new and interesting research towards the realization of high performance devices based on the interplay between these two opposite orders.

In this context, a viable future development will be to realize pseudo spin valve (PSV) devices using two F layers made of different ferromagnetic materials with the different coercitive fields separated by a superconducting layer [20]. In this case the spacer layer is relatively thick, and is used to decouple the ferromagnetic layers to prevent them from switching at the same field. In such an instance the fundamental physics will play with the interlink between these two competing orders, and on the practical point of view it could be the starting brick for suitable devices. In this way the magnetization orientation of the F/S/F structure can be controlled by a weak magnetic field which by

itself is insufficient to destroy superconductivity, but the small magnetic field enables the softer F layer to be aligned with it, while the harder material will not switch. This artificial structure allows active control of the magnetic state of the barrier. The magnetoresistance of the PSV gives direct access to the information about relative orientation of the ferromagnetic layers, and the magnetic state of the barrier.

The novelty, and strength of such devices, lies in the fact that these heterostructures can be realized either with classical ferromagnetic materials and low-T_C superconductors, or with colossal magneto-resistance materials and high-T_C cuprates. So what will be the most promising future technology??? Will it rely on liquid helium, or nitrogen???? We hope to contribute towards providing a proper answer to such dilemmas. On a far-reaching scope, the route to room-temperature applications would constitute a more formidable challenge for our research.

LIST OF PUBLICATIONS

[S1] S. Piano, F. Bobba, F. Giubileo, A. Vecchione, A. M. Cucolo, *Point Contact Study Of The Superconducting Order Parameter In* $RuSr_2GdCu_2O_8$, Int. J. Mod. Phys. B **19**, 323 (2005).

[S2] F. Giubileo, F. Bobba, M. Aprili, S. Piano, A. Scarfato and A. M. Cucolo, *Subharmonic gap structures and Josephson effect in MgB2/Nb microconstrictions*, Phys. Rev. B **72**, 174518 (2005).

[S3] S. Piano, F. Bobba, F. Giubileo, M. Gombos, A. Vecchione and A. M. Cucolo, *Pairing state in the rutheno-cuprate superconductor* $RuSr_2GdCu_2O_8$*: A Point Contact Andreev Reflection Spectroscopy study*, Phys. Rev. B **73**, 064514 (2006).

[S4] S. Piano, F. Bobba, F. Giubileo, A. Vecchione, A. M. Cucolo, *Point-Contact Spectroscopy on* $RuSr_2GdCu_2O_8$, J. of Phys. and Chem. of Solids **67**, 384 (2006).

[S5] S. Piano, F. Bobba, A. De Santis, F. Giubileo, A. Scarfato and A. M. Cucolo, *Point Contact Spectra on* $YBa_2Cu_3O_{7-x}/La_{0.7}Ca_{0.3}MnO_3$ *bilayers*, Journal of Physics: Conference Series **43**, 1123 (2006).

[S6] J. W. A. Robinson, S. Piano, G. Burnell, C. Bell, and M. G. Blamire, *Critical current oscillations in strong ferromagnetic* π*-junctions*, Phys. Rev. Lett. **97**, 177003 (2006).

[S7] S. Piano, F. Bobba, A. De Santis, F. Giubileo, and A. M. Cucolo, *Point Contact Spectroscopy on ferromagnetic/superconducting heterostructures*, in press on Physica C (2006).

[S8] F. Giubileo, F. Bobba, M. Aprili, S. Piano, A. Scarfato, and A. M. Cucolo, *Temperature Evolution of Subharmonic Gap Structures in MgB_2/Nb Point-Contacts*, in press on Physica C (2006).

[S9] J. W. A. Robinson, S. Piano, G. Burnell, C. Bell, and M. G. Blamire, *Transport and Magnetic Properties of Strong Ferromagnetic Pi-Junctions*, submitted to IEEE Trans. Appal. Supercon. (2006).

[S10] S. Piano, J. W. A. Robinson, G. Burnell, and M. G. Blamire, *0-π oscillations in nanostructured Nb/Fe/Nb Josephson junctions*, cond-mat 0612235 (2006).

BIBLIOGRAPHY

[1] J. Aarts, J. M. E. Geers, E. Brck, A. A. Golubov, and R. Coehoorn, Phys. Rev. B **56**, 2779 (1997).

[2] A. A. Abrikosov, *Fundamental of the Theory of Metals* (North Holland, New York, 1988).

[3] A. A. Abrikosov, J. Phys. Cond. Matt. **13**, L943 (2001).

[4] B. Altshuler and A. Aronov, in *Electron-Electron Interactions in Disordered Systems* (A. L. Efros and M. Pollak, eds.), North-Holland, Amsterdam (1985).

[5] A. F. Andreev, Zh. Eksp. Teor. Fiz. **46**, 1128 (1964).

[6] D. Aoki, A. Huxley, E. Ressouche, D. Braithwaite, J. Flou-quet, J.-P. Brison, E. Lhotel, and C. Paulsen, Nature **413**, 613 (2001).

[7] G.B. Arnold, J. Low Temp. Phys. **68**, 1 (1987).

[8] C. Attanasio, M. Salvato, R. Ciancio, M. Gombos, S. Pace, S. Uthayakumar, and A. Vecchione, Physica C **411**, 126 (2004).

[9] M. H. Badr, M. Freamat, Y. Sushko, and K.-W. Ng, Phys. Rev. B **65**, 184516 (2002).

[10] J. Bardeen, L. N. Cooper, and J. R. Schrieffer, Phys. Rev. **79**, 845 (1950).

[11] J. Bardeen, L. N. Cooper, and J. R. Schrieffer, Phys. Rev. **104**, 1189 (1956).

[12] J. Bardeen, L. N. Cooper, and J. R. Schrieffer, Phys. Rev. **108**, 1175 (1957).

[13] J. Bardeen, L. N. Cooper, and J. R. Schrieffer, Phys. Today **25**, 73 (1972).

[14] L. J. Barnes, Phys. Rev. **184**, 434 (1969).

[15] A. Barone and G. Paternò, *Physics and Applications of the Josephson effect* (John Wiley & Sons, 1982).

[16] L. Bauernfeind, W. Widder, and H. F. Braun, Physica C **254**, 151 (1995).

[17] J. G. Bednorz and K. A. Muller, Z. Phys. B **64**, 189 (1986).

[18] C. Bell, Ph.D. thesis (University of Cambridge, 2003).

[19] C. Bell, G. Burnell, D.-J. Kang, R. H. Hadfield, M. J. Kappers, and M. G. Blamire, Nanotechnology **14**, 630 (2003).

[20] C. Bell, G. Burnell, C. W. Leung, E. J. Tarte, D.-J. Kang, and M. G. Blamire, Appl. Phys. Lett. **84**, 1153 (2003).

[21] C. Bell, R. Loloee, G. Burnell, and M. G. Blamire, Phys. Rev. B **71**, 180501 (R) (2005).

[22] F. S. Bergeret, A. F. Volkov, and K. B. Efetov1, Phys. Rev. B **64**, 134506 (2001).

[23] C. Bernhard, J. L. Tallon, E. Brücher, and R. K. Kremer, Phys. Rev. B **61**, R14 960 (2000).

[24] C. Bernhard, J. L. Tallon, Ch. Niedermayer, Th. Blasius, A. Golnik, E. Brücher, R. K. Kremer, D. R. Noakes, C. E. Stronach, and E. J. Ansaldo, Phys. Rev. B **59**, 14099 (1999).

[25] G. E. Blonder, M. Tinkham, and T. M. Klapwijk, Phys. Rev. B **25**, 4515 (1982).

[26] Y. Blum, A. Tsukernik, M. Karpovski, and A. Palevski1, Phys. Rev. Lett. **89**, 187004 (2002).

[27] F. Bobba, D. Roditchev, R. Lamy, E-M Choi, H-J Kim, W. N. Kang, V. Ferrando, C. Ferdeghini, F. Giubileo, W. Sacks, S-I Lee, J. Klein, and A. M. Cucolo, Supercond. Sci. Technol. **16**, 167 (2003).

[28] F. Born, M. Siegel, E. K. Hollmann, H. Braak, A. A. Golubov, D. Yu. Gusakova, and M. Yu. Kupriyanov, Phys. Rev. B **74**, 140501 (R) (2006).

[29] F. Bouquet, R.A. Fisher, N.E. Phillips, D.G. Hinks, and J.D. Jorgensen, Phys. Rev. Lett. **87**, 047001 (2001).

[30] E. N. Bratus, V. S. Shumeiko, and G. Wendin, Phys. Rev. Lett. **74**, 2110 (1995).

[31] A. Brinkman, A. A. Golubov, H. Rogalla, O. V. Dolgov, J. Kortus, Y. Kong, O. Jepsen, and O. K. Andersen, Phys. Rev. B **65**, 180517(R) (2002).

[32] Y. Bugoslavsky, Y. Miyoshi, G. K. Perkins, A. V. Berenov, Z. Lockman, J. L. MacManus-Driscoll, L. F. Cohen, A. D. Caplin, H. Y. Zhai, M. P. Paranthaman, H. M. Christen, and M. Blamire, Supercond. Sci. Technol. **15**, 526 (2002).

[33] K. H. J. Buschow and F. R. de Boer, *Physics of Magnetism and Magnetic Materials* (Kluwer Academic/Plenum Publishers, New York, 2003).

[34] A. Butera, A. Fainstein, E. Winkler, and J. Tallon, Phys. Rev. B **63**, 054442 (2001).

[35] A. I. Buzdin, Rev. Mod. Phys. **77**, 935 (2005).

[36] A. I. Buzdin, L.N. Bulaevskii, and S.V. Panyukov, JETP Lett. **35**, 179 (1982).

[37] A. I. Buzdin and M. V. Kuprianov, JETP Lett. **52**, 488 (1990).

[38] A. I. Buzdin and M. V. Kuprianov, JEPT Lett. **52**, 487 (1990).

[39] A. I. Buzdin and M. V. Kuprianov, JETP Lett. **53**, 321 (1991).

[40] P. C. Canfield, P. L. Gammel, and D. J. Bishop, Phys. Today **51**, 40 (1998).

[41] D. Cao, F. Bridges, D. C. Worledge, C. H. Booth, and T. Geballe, Phys. Rev. B **61**, 11373 (2000).

[42] G. Carapella, N. Martucciello, G. Costabile, C. Ferdeghini, V. Ferrando, and G. Grassano, Appl. Phys. Lett. **80**, 2949 (2002).

[43] K. Chahara, T. Ohno, M. Kasai, and Y. Kozono, Appl. Phys. Lett. **63**, 1990 (1993).

[44] P. Chaudhari and S-Y Lin, Phys. Rev. Lett. **72**, 1084 (1994).

[45] X.K. Chen, M.J. Konstantinovic, J.C. Irwin, D.D. Lawrie, and J.P. Franck, Phys. Rev. Lett. **87**, 157002 (2001).

[46] M. R. Cimberle, M. Tropeano, A. Martinelli M. Feretti, C. Artini, and G. A. Costa, Supercond. Sci. Technol. **18**, 454 (2005).

[47] P. Coleman, Nature **406**, 580 (2000).

[48] M. K. Covo, A. W. Molvik, A. Friedman, G. Westenskow, J. J. Barnard, R. Cohen, P. A. Seidl, J. W. Kwan, G. Logan, D. Baca, F. Bieniosek, C. M. Celata, J.-L. Vay, and J. L. Vujic, Phys. Rev. ST AB **9**, 063201 (2006).

[49] A. M. Cucolo, Physica C **305**, 85 (1998).

[50] Y. Dagan, R. Krupke, and G. Deutscher, Phys. Rev. B **62**, 146 (2000).

[51] A. De Santis, Ph.D. thesis (University of Salerno, 2003).

[52] A. De Santis, F. Bobba, M. A. Boffa, R. Caciuffo, P. Mengucci, M. Salvato, A. Vecchione, and A. M. Cucolo, Physica C **408**, 48 (2004).

[53] A. De Santis, F. Bobba, G.Cristiani, A. M. Cucolo, K.Frohlich, H.-U. Habermeierb, M.Salvato, and A. Vecchione, J. Magn. Magn. Mater. **262**, 150 (2003).

[54] E. A. Demler and M. R. Beasley G. B. Arnold, Phys. Rev. B **55**, 15 174 (1997).

[55] G. Deutscher, Rev. Mod. Phys. **77**, 109 (2005).

[56] G. Deutscher and P. G. De Gennes, in *Superconductivity*, Ed. R. D. Parks (Marcel Dekker, INC.,New York, 1969).

[57] M. H. Doveret, A. Wallraff, and J. M. Martinis, cond-mat/0411174 (2004).

[58] A. M. Duif, A. G. M. Jansen, and P. Wyder, J. Phys.: Condens. Matter **1**, 3157 (1989).

[59] R. C. Dynes, V. Narayanamurti, and J. P. Garno, Phys. Rev. Lett. **41**, 1509 (1978).

[60] D. Fay and J. Appel, Phys. Rev. B **22**, 3173 (1980).

[61] Focused Ion Beam Workstation Reference Guide, FEI Company (1996).

[62] S. Foner, Rev. of Sci. Inst. **30**, 548 (1959).

[63] M. Forgelstrom, D. Rainer, and J. A. Sauls, Phys. Rev. Lett. **79**, 281 (1997).

[64] P. Fulde and R. A. Ferrell, Phys. Rev. **135**, A550 (1964).

[65] H. E. Hoenig G. Binnig, A. Baratoff and J. G. Bednorz, Phys. Rev. Lett. **45**, 1352 (1980).

[66] I. Giaever, Phys. Rev. Lett. **5**, 147 (1960).

[67] I. Giaever and K. Megerle, Phys. Rev. **122**, 251 (1961).

[68] V. L. Ginzburg, Sov. Phys. JETP **4**, 153 (1957).

[69] F. Giubileo, D. Roditchev, W. Sacks, R. Lamy, D. X. Thanh, J. Klein, S. Miraglia, D. Fruchart, J. Marcus, and P. Monod, Phys. Rev. Lett. **87**, 177008 (2001).

[70] K. Gloos, Phys. Rev. Lett. **85**, 5257 (2000).

[71] R. S. Gonnelli, A. Calzolari, D. Daghero, G. A. Ummarino, V. A. Stepanov, G. Giunchi, S. Ceresara, and G. Ripamonti, Phys. Rev. Lett. **87**, 097001 (2001).

[72] R. S. Gonnelli, D. Daghero, A. Calzolari, G. A. Ummarino, V. Dellarocca, V. A. Stepanov, J. Jun, S. M. Kazakov, and J. Karpinski, Phys. Rev. B **69**, 100504 (R) (2004).

[73] M. Grajcar, A. Plecenik, P. Seidel, and A. Pfuch, Phys. Rev. B **51**, 16185 (1995).

[74] W. Guichard, M. Aprili, O. Bourgeois, T. Kontos, J. Lesueur, and P. Gandit, Phys. Rev. Lett. **90**, 167001 (2003).

[75] B. A. Gurney, V. S. Speriosu, J. P. Nozieres, H. Lefakis, D. R. Wilhoit, and O. U. Need, Phys. Rev. Lett. **71**, 4023 (1993).

[76] D. Yu. Gusakova, M. Yu. Kupriyanov, and A. A. Golubov, JETP Lett. **83**, 487 (2006).

[77] H.A.Jahn and E. Teller, Proc. R. Soc. London A **161**, 220 (1937).

[78] J. W. Halley ed., *Theory of High-Temperature Superconductivity* (Addison-Wesley, Redwood City, CA, 1988).

[79] W. N. Hardy, D. A. Bonn, D. C. Morgan, R. Liang, and K. Zhang, Phys. Rev. Lett. **70**, 3999 (1990).

[80] D. J. Van Harlingen, Rev. Mod. Phys. **67**, 515 (1995).

[81] P. Heinmann, F.J. Himpsel, and D.E. Eastman, Solid State Comm. **39**, 219 (1981).

[82] R. Von Helmolt, J.Wecker, B. Holzapfel, L. Schultz, and K. Samwer, Phys. Rev. Lett. **71**, 2331 (1993).

[83] T. Hirai, Y. Tanaka, N. Yoshida, Y. Asano, J. Inoue, and S. Kashiwaya, Phys. Rev. B **67**, 174501 (2003).

[84] M. Hurd, S. Datta, and P. F. Bagwell, Phys. Rev. B **54**, 6557 (1996).

[85] M. Iavarone, G. Karapetrov, A. E. Koshelev, W. K. Kwok, G. W. Crabtree, D. G. Hinks, W. N. Kang, E.-M. Choi, H. J. Kim, H.-J. Kim, and S. I. Lee, Phys. Rev. Lett. **89**, 187002 (2002).

[86] J. S. Jiang, D. Davidovic, D. H. Reich, and C.L. Chien, Phys. Rev. Lett. **74**, 314 (1995).

[87] S. Jin, T.H. Tiefel, M. M.Cormack, R.A. Fastnacht, R. Ramesh, and L.H. Chen, Science **264**, 413 (1994).

[88] Z. Jirák, S. Vratislav, and J. Zajícek, Phys. Stat. Sol. **52**, K 39 (1979).

[89] G.H. Jonker and J.H. Van Santen, Physica **16**, 337 (1950).

[90] B. D. Josephson, Phys. Lett. **1**, 1101 (1962).

[91] S. Kashiwaya and Y. Tanaka, Rep. Prog. Phys. **63**, 1641 (2000).

[92] S. Kashiwaya, Y. Tanaka, N. Yoshida, and M. R. Beasley, Phys. Rev. B **60**, 3572 (1999).

[93] R. J. Kelley, C. Quitmann, M. Onellion, H. Berger, P. Almeras, and G. Margaritondo, Science **271**, 1255 (1996).

[94] S.-J. Kim, Yu I. Latyshev, and T. Yamashita, Appl. Phys. Lett. **74**, 1156 (1999).

[95] M. Kitada and N. Shimizu, J. Mat. Sci. Lett. **10**, 437 (1991).

[96] R. Kleiner, A. S. Katz, A. G. Sun, R. Summer, D. A. Gajewski, S. H. Han, S. I. Woods, E. Dantsker, B. Chen, K. Char, M. B. Maple, R. C. Dynes, and J. Clarke, Phys. Rev. Lett. **76**, 2161 (1996).

[97] T. Kontos, M. Aprili, J. Lesueur, F. Genêt, B. Stephanidis, and R. Boursier, Phys. Rev. Lett. **86**, 304 (2001).

[98] T. Kontos, M. Aprili, J. Lesueur, F. Genêt, B. Stephanidis, and R. Boursier, Phys. Rev. Lett. **89**, 137007 (2002).

[99] J. Kortus, I. I. Mazin, K. D. Belashchenko, V. P. Antropov, and L. L. Boyer, Phys. Rev. Lett. **86**, 4656 (2001).

[100] J. Kötzler and W. Gil, Phys. Rev. B **72**, 060412(R) (2005).

[101] K. Krishna, N. P. Ong, Q. Li, G. D. Gu, and N. Koshizuka, Science **277**, 83 (1997).

[102] J. Kübler ed., *Theory of Itinerant Electron Magnetism* (Oxford University Press, 2000).

[103] K. I. Kumagai, S. Takada, and Y. Furukawa, Phys. Rev. B **63**, 180509 (R) (2001).

[104] P. A. Lee, J. Appl. Phys. **42**, 325 (1971).

[105] S. Y. Lee, J. H. Lee, J. S. Ryu, J. Lim, H. N. Lee S. H. Moon, H. G. Kim, and B. Oh, Appl. Phys. Lett. **79**, 3299 (2001).

[106] Qu. Leng, H. Han, and C. Hiner, J. Appl. Phys. **87**, 6621 (2000).

[107] A.Y. Liu, I. I. Mazin, and J. Kortus, Phys. Rev. Lett. **87**, 4087005 (2001).

[108] F. London, *Superfluids* (John Wiley & Sons, Inc., New York, 1950).

[109] S. Lundquist and *et al.* eds., *Towards the Theoretical Understanding of High-Tc Superconductivity* (World Scientific, Singapore, 1989).

[110] P. S. Luo, H. Wu, F. C. Zhang, C. Cai, X. Y. Qi, X. L. Dong, W. Liu, X. F. Duan, B. Xu, L. X. Cao, X. G. Qiu, and B. R. Zhao, Phys. Rev. B **71**, 094502 (2005).

[111] P. S. Luo, H. Wu, F. C. Zhang, C. Cai, X. Y. Qi, X. L. Dong, W. Liu, X. F. Duan, B. Xu, L. X. Cao, X. G. Qiu, and B. R. Zhao1, Phys. Rev. B **71**, 094502 (2005).

[112] J. W. Lynn, B. Keimer, C. Ulrich, C. Bernhard, and J. L. Tallon, Phys. Rev. B **61**, 14964 (R) (2000).

[113] D.H. Martin, *Magnetism in Solids* (MIT Press, 1967).

[114] P. Martinez-Samper, J. G. Rodrigo, G. Rubio-Bollinger, H. Suderow, S. Vieira, S. Lee, and S. Tajima, Physica C **385**, 233 (2002).

[115] W. Meissner and R. Ochesenfeld, Naturwiss. **21**, 787 (1933).

[116] N. Miyakawa, P. Guptasarma, J. F. Zasadzinski, D. G. Hinks, and K. E. Gray, Phys. Rev. Lett. **80**, 157 (1998).

[117] Y. Miyoshi, Y. Bugoslavsky, and L. F. Cohen, Phys. Rev. B **72**, 012502 (2005).

[118] T. Nachtrab, C. Bernhard, C. T. Lin, D. Koelle, and R. Kleiner, cond-mat/0508044 (2005), Special Issue on "Magnetism and Superconductivity Coexistence".

[119] T. Nachtrab, D. Koelle, R. Kleiner, C. Bernhard, and C. T. Lin, Phys. Rev. Lett. **92**, 117001 (2004).

[120] J. Nagamatsu, N. Nakagawa, T. Muranaka, Y. Zenitani, and J. Akimitsu, Nature **410**, 63 (2001).

[121] Yu. G. Naidyuk, R. Häusslera, and H. v. Löhneysenet, Physica B **218**, 122 (1996).

[122] Yu. G. Naidyuk and I. K. Yanson, J. Phys. : Condens. Matter **10**, 8905 (1998).

[123] M. A. Nielsen and I. L. Chuang, *Quantum computation and quantum information*.

[124] M. Octavio, M. Tinkham, G. E. Blonder, and T. M. Klapwijk, Phys. Rev. B **27**, 6739 (1983).

[125] H. K. Onnes, Leiden Comm. **1206**, 1226 (1911).

[126] J. Orloff, Rev. Sci. Instrum. **64**, 1105 (1993).

[127] G. Ortiz, M. Harris, and P. Ballone, Phys. Rev. Lett. **82**, 5317 (1999).

[128] R. D. Parks ed., *Superconductivity* (Marcel Dekker, Inc., New York, 1969).

[129] L. Pauling, J. Appl. Phys. **8**, 385 (1937).

[130] V. Peña, Z. Sefrioui, D. Arias, C. Leon, J. Santamaria, J. L. Martinez, S. G. E. te Velthuis, and A. Hoffmann, Phys. Rev. Lett. **94**, 057002 (2005).

[131] M. A. Peshkin and R. A. Buhrman, Phys. Rev. B **28**, 161 (1983).

[132] C. Pfleiderer, M. Uhlarz, S. M. Hayden, R. Vollmer, H. Lohneysen, N. Bernhoeft, and G. Lonzarich, Nature **412**, 58 (2001).

[133] S. Pick, I. Turek, and H. Dreyssé, Solid State Commun. **124**, 21 (2002).

[134] Ya. G. Ponomarev, S. A. Kuzmichev, M. G. Mikheev, M. V. Sudakova, S. N. Tchesnokov, N. Z. Timergaleev, A. V. Yarigin, E. G. Maksimov, S. I. Krasnosvobodtsev, A. V. Varlashkin, M. A-Hein, H. Piel G. Müller, L. G. Sevastyanova, O. V. Kravchenko, K. P. Burdina, and B. M. Bulychev, Solid State Communications **129**, 85 (2004).

[135] M. Požek, A. Dulčić, D. Paar, A. Hamzić, M. Basletić, G. V. M. Williams E. Tafra, and S. Krämer, Phys. Rev. B **65**, 174514 (2002).

[136] M. Prester, M.Stubičar E. Babić, and P. Nozar, Phys. Rev. B **49**, 6967 (1994).

[137] J.W. Quilty, S. Lee, A. Yamamoto, and S. Tajima, Phys. Rev. Lett. **88**, 087001 (2002).

[138] G.T. Rado and H. Suhl eds., *Magnetism* (Academic Press, 1966).

[139] Z. Radovic, L. Dobrosavljević-Grujić, A. I. Buzdin, and John R. Clem, Phys. Rev. B **38**, 2388 (1988).

[140] Z. Radovic, M. Ledvij, L. Dobrosavljević-Grujić, A. I. Buzdin, and John R. Clem, Phys. Rev. B **44**, 759 (1991).

[141] A. K. Raychaudhuri, K. P. Rajeev, H. Srikanth, and N. Gayathri, Phys. Rev. B **51**, 7421 (1995).

[142] S. Reyntjens and R. Puers, J. Micromech. Microeng. **11**, 287 (2001).

[143] J.M. Rowell and W.L. Feldman, Phys. Rev. **172**, 393 (1968).

[144] A. Saito, A. Kawakami, H. Shimakage, H. Terai, and Z. Wang, J. Appl. Phys. **92**, 7369 (2002).

[145] S. S. Saxena, P. Agarwal, K. Ahilan, F. M. Grosche, R. K. W. Haselwimmer, M. J. Steiner, E. Pugh, I. R. Walker, S. R. Julian, P. Monthoux, and *et al.*, Nature **406**, 587 (2000).

[146] E. Scheer, P. Joyez, D. Esteve, C. Urbina, and M. H. Devoret, Phys. Rev. Lett. **78**, 3535 (1997).

[147] A. Schilling, M. Cantoni, J. D. Guo, and H. R. Ott, Nature **58**, 908 (1993).

[148] H. Schmidt, J. F. Zasadzinski, K. E. Gray, and D. G. Hinks, Phys. Rev. Lett. **88**, 127002 (2002).

[149] J. R. Schrieffer and J. W. Wilkins, Phys. Rev. Lett. **10**, 17 (1963).

[150] Z. Sefrioui, D. Arias, V. Peña, J. E. Villegas, M. Varela, P. Prieto, C. León, J. L. Martinez, and J. Santamaria, Phys. Rev. B **67**, 214511 (2003).

[151] L. Shan, H. J. Tao, H. Gao, Z. Z. Li, Z. A. Ren, G. C. Che, and H. H. Wen, Phys. Rev. B **68**, 144510 (2003).

[152] S. Shapiro, Phys. Rev. Lett. **11**, 80 (1963).

[153] Y. Sharvin, Zh. Ekperim. i. Teor. Fiz. **48**, 984 (1965), (Soviet Physics JETP, **21**, 655).

[154] Z. Z. Sheng and A. M. Hermann, Nature **332**, 55 (1989).

[155] H. Shimakage, K. Tsujimoto, Z. Wang, and M. Tonouchi, Appl. Phys. Lett. **86**, 072512 (2005).

[156] S. V. Shulga, S.-L. Drechsler, H. Eshrig, H. Rosner, and W. E. Pickett, e–print cond-mat/0103154 (2001).

[157] J. C. Slater, Phys. Rev. **49**, 537 (1936).

[158] R.J. Soulen, J.M. Byers, M.S. Osofsky, B. Nadgorny, S.F. Cheng T. Ambrose, P.R. Broussard, C.T. Tanaka, J. Nowak, J.S. Moodera, A. Barry, and J.M.D. Coey, Science **282**, 85 (1998).

[159] B. C. Stoner, Proc. Roy. Soc. **165**, 372 (1938).

[160] G. J. Strijkers, Y. Ji, F. Y. Yang, C. L. Chien, and J. M. Byers, Phys. Rev. B **63**, 104510 (2001).

[161] H. Suhl, Phys. Rev. Lett. **87**, 167007 (2001).

[162] H. Suhl, B. T. Matthias, and L. R. Walker, Phys. Rev. Lett. **3**, 552 (1959).

[163] I. W. Sumarlin, S. Skanthakumar, J. W. Lynn, J. L. Peng, Z. Y. Li, W. Jiang, and R. L. Greene, Phys. Rev. Lett. **68**, 2228 (1992).

[164] A. G. Sun, D. A. Gajewski, M. B. Maple, and R.C. Dynes, Phys. Rev. Lett. **72**, 2267 (1994).

[165] P. Szabó, P. Samuely, J. Kacmarcík, T. Klein, J. Marcus, D. Fruchart, S. Miraglia, C. Marcenat, and A. G. M. Jansen, Phys. Rev. Lett. **87**, 137005 (2001).

[166] T. Takahashi, T. Sato, S. Souma, T. Muranaka, and J. Akimitsu, Phys. Rev. Lett. **86**, 4915 (2001).

[167] H. J. Tao, Z. Z. Li, Y. Xuan, Z. A. Ren, G. C. Che, B. R. Zhao, and Z. X. Zhao, Physica C **386**, 569 (2003).

[168] M. Tinkham, *Introduction to superconductivity* (McGraw-Hill, Inc., USA, 1976).

[169] Y. Tokunaga, H. Kotegawa, K. Ishida, Y. Kitaoka, H. Takagiwa, and J. Akimitsu, Phys. Rev. Lett. **86**, 5767 (2001).

[170] Y. Tokura ed., *Colossal Magnetoresistance Oxides* (Gordon and Breach, Monographs in Condensed Matter Science, London, 2000).

[171] C. C. Tsuei, J. R. Kirtley, C. C. Chi, L. S. Yu-Jahnes, A. Gupta, T. Shaw, J. Z. Sun, and M. B. Ketchen, Phys. Rev. Lett. **73**, 593 (1994).

[172] K. Ueda, S. Saito, K. Semba, T. Makimoto, and M. Naito, Appl. Phys. Lett. **86**, 172502 (2005).

[173] T. Van Duzer and C. W. Turner, *Principles of Superconductive Devices and Circuits* (Edward Arnold, London, 1981).

[174] Y. Wang, T. Plackowski, and A. Junod, Physica C **355**, 179 (2001).

[175] J. Y. T. Wei, N.-C. Yeh, D. F. Garrigus, and M. Strasik, Phys. Rev. Lett. **81**, 2542 (1998).

[176] E.O. Wollen and W.C. Koehler, Phys. Rev **100**, 545 (1955).

[177] D. A. Wollman, D. J. Van Harlingen, W. C. Lee, D. M. Ginsberg, and A. Leggett, Phys. Rev. Lett. **71**, 2134 (1993).

[178] M. K. Wu, J. R. Ashburn, C. J. Torng, P. H. Hor, R. L. Meng, L. Gao, Z. J. Huang, Y. Q. Wang, and C. W. Chu, Phys. Rev. Lett. **363**, 56 (1987).

[179] M. Xu, H. Kitazawa, Y. Takano, J. Ye, k. Nishida, H. Abe, A. Matsushita, N. Tsujii, and G. Kido, Appl. Phys. Lett. **79**, 2779 (2001).

[180] T. Yamashita, K. Tanikawa, and S. Maekawa, Phys. Rev. B **73**, 144517 (2006).

[181] T. Yamashita, K. Tanikawa, S. Takahashi, and S. Maekawa, Phys. Rev. Lett. **95**, 097001 (2005).

[182] R. Zhang and R. F. Willis, Phys. Rev. Lett. **86**, 2665 (2001).

[183] J-X Zhu, B. Friedman, and C. S. Ting, Phys. Rev. B **59**, 9558 (1999).

[184] U. Zimmermann, S. Abens, D. Dikin, K. Keck, and V. M. Dmitriev, Z. Phys. Cond. Mat. **97**, 59 (1995).